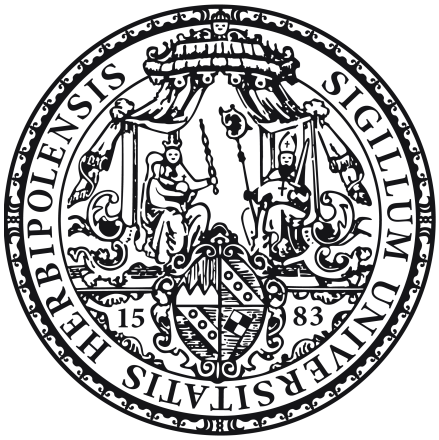

Engineering approaches in biofabrication of vascularized structures

Ingenieurtechnische Ansätze in der Biofabrikation vaskularisierter Strukturen

Doctoral thesis

for a doctoral degree at the Graduate School of Life Sciences,
Julius-Maximilians-Universität Würzburg,

Section Biomedicine

submitted by

Ali Nadernezhad

from

Tehran, Iran

Würzburg 2022

Submitted on: ……

Office stamp

Members of the *Thesis Committee*:

Chairperson: Prof. Dr. Jürgen Seibel

Primary Supervisor: Prof. Dr. Jürgen Groll

Supervisor (Second): Prof. Dr. Iwona Cicha

Supervisor (Third): Prof. Dr. Süleyman Ergün

Supervisor (Forth): Prof. Dr.-Ing. habil. Aldo R. Boccaccini

Date of Public Defense: ……

Date of Receipt of Certificates: ……

بساز رود که در نشیب دره سر به سنگ می‌زند

رونده باش

امید هیچ معجزی ز مرده نیست

زنده باش

ه. الف سایه

LIST OF PUBLICATIONS

As the first author:

1) **Nadernezhad, A.**, Forster, L., Netti, F., Adler-Abramovich, L., Teßmar, J. and Groll, J.. Rheological analysis of the interplay between the molecular weight and concentration of hyaluronic acid in formulations of supramolecular HA/FmocFF hybrid hydrogels. *Polymer Journal*, **2020**, 52(8), pp.1007-1012.

2) **Nadernezhad, A.**, Ryma, M., Genç, H., Cicha, I., Jüngst, T. and Groll, J.. Melt electrowriting of isomalt for high-resolution templating of embedded microchannels. *Advanced Materials Technologies*, **2021**, 6(8), p.2100221.

3) Ryma, M.*, Genç, H.*, **Nadernezhad, A.***, Paulus, I., Schneidereit, D., Friedrich, O., Andelovic, K., Lyer, S., Alexiou, C., Cicha, I. and Groll, J.. A print-and-fuse Strategy for Sacrificial Filaments Enables Biomimetically Structured Perfusable Microvascular Networks with Functional Endothelium Inside 3D Hydrogels. *Advanced Materials*, **2022**, p.2200653.

4) **Nadernezhad, A.**, Groll, J.. Machine learning reveals a general understanding of printability in formulations based on rheology additives. *Advanced Science*, **2022**, p. 2202638.

* Equally shared author contributions

As the co-author:

1) Lorson, T., Ruopp, M., **Nadernezhad, A.**, Eiber, J., Vogel, U., Jungst, T. and Lühmann, T.. Sterilization methods and their influence on physicochemical properties and bioprinting of alginate as a bioink component. *ACS omega*, **2020**, 5(12), pp.6481-6486.
2) Hauptstein, J., Böck, T., Bartolf-Kopp, M., Forster, L., Stahlhut, P., **Nadernezhad, A.**, Blahetek, G., Zernecke-Madsen, A., Detsch, R., Jüngst, T. and Groll, J.. Hyaluronic Acid-Based Bioink Composition Enabling 3D Bioprinting and Improving Quality of Deposited Cartilaginous Extracellular Matrix. *Advanced Healthcare Materials*, **2020**, 9(15), p.2000737.
3) Horder, H., Guaza Lasheras, M., Grummel, N., **Nadernezhad, A.**, Herbig, J., Ergün, S., Teßmar, J., Groll, J., Fabry, B., Bauer-Kreisel, P. and Blunk, T.. Bioprinting and differentiation of adipose-derived stromal cell spheroids for a 3D breast cancer-adipose tissue model. *Cells*, **2021**, 10(4), p.803.
4) Hauptstein, J., Forster, L., **Nadernezhad, A.**, Groll, J., Teßmar, J. and Blunk, T.. Tethered TGF-β1 in a Hyaluronic Acid-Based Bioink for Bioprinting Cartilaginous Tissues. *International journal of molecular sciences*, **2022**, 23(2), p.924.

5) Hauptstein, J., Forster, L., **Nadernezhad, A.**, Horder, H., Stahlhut, P., Groll, J., Blunk, T. and Teßmar, J.. Bioink Platform Utilizing Dual-Stage Crosslinking of Hyaluronic Acid Tailored for Chondrogenic Differentiation of Mesenchymal Stromal Cells. *Macromolecular Bioscience*, **2022**, 22(2), p.2100331.

Statement of individual author contributions and of legal second publication rights to manuscripts included in the dissertation

Manuscript 1 (complete reference): Nadernezhad, A., Ryma, M., Genç, H., Cicha, I., Jüngst, T. and Groll, J., 2021. Melt electrowriting of isomalt for high-resolution templating of embedded microchannels. Advanced Materials Technologies, 6(8), p.2100221

Participated in	**Author Initials,** Responsibility decreasing from left to right				
Study Design Methods Development	AN AN	JG			
Data Collection	AN				
Data Analysis and Interpretation	AN				
Manuscript Writing Writing of Introduction Writing of Materials & Methods Writing of Discussion Writing of First Draft	 AN AN AN AN	 JG JG	 TJ	 MR	 IC

Explanations (if applicable):

Manuscript 2 (complete reference): Ryma, M.*, Genç, H.*, Nadernezhad, A.*, Paulus, I., Schneidereit, D., Friedrich, O., Andelovic, K., Lyer, S., Alexiou, C., Cicha, I. and Groll, J., 2022. A print-and-fuse Strategy for Sacrificial Filaments Enables Biomimetically Structured Perfusable Microvascular Networks with Functional Endothelium Inside 3D Hydrogels. Advanced Materials, p.2200653.

Participated in	**Author Initials,** Responsibility decreasing from left to right				
Study Design Methods Development	MR MR	AN AN	JG JG	IC IC	HG HG
Data Collection	AN	MR	HG	IP	DS
Data Analysis and Interpretation	AN	HG	IC	MR	JG
Manuscript Writing Writing of Introduction Writing of Materials & Methods Writing of Discussion Writing of First Draft	 MR AN AN MR	 AN MR IC AN	 JG HG MR HG	 IC JG	 HG

Explanations: * equally shared author contributions

Manuscript 3 (complete reference): Nadernezhad, A., Forster, L., Netti, F., Adler-Abramovich, L., Teßmar, J. and Groll, J., 2020. Rheological analysis of the interplay between the molecular weight and concentration of hyaluronic acid in formulations of supramolecular HA/FmocFF hybrid hydrogels. Polymer Journal, 52(8), pp.1007-1012.					
Participated in	**Author Initials,** Responsibility decreasing from left to right				
Study Design Methods Development	AN	JG	JT		
Data Collection	AN				
Data Analysis and Interpretation	AN	JG	JT		
Manuscript Writing Writing of Introduction Writing of Materials & Methods Writing of Discussion Writing of First Draft	 AN AN AN AN	 JG			

Manuscript 4 (complete reference): Nadernezhad, and Groll, J., 2022. Machine learning reveals a general understanding of printability in formulations based on rheology additives. Advanced Science, p.2202638.					
Participated in	**Author Initials,** Responsibility decreasing from left to right				
Study Design Methods Development	AN				
Data Collection	AN				
Data Analysis and Interpretation	AN				
Manuscript Writing Writing of Introduction Writing of Materials & Methods Writing of Discussion Writing of First Draft	 AN AN AN AN	 JG JG			

If applicable, the doctoral researcher confirms that he has obtained permission from both the publishers (copyright) and the co-authors for legal second publication.

The doctoral researcher and the primary supervisor confirm the correctness of the above-mentioned assessment.

Ali Nadernezhad	23.10.2022	Dresden	
Doctoral Researcher's Name	Date	Place	Signature
Jürgen Groll			
Primary Supervisor's Name	Date	Place	Signature

Statement of individual author contributions to figures/tables of manuscripts included in the dissertation

Manuscript 1 (complete reference): Nadernezhad, A., Ryma, M., Genç, H., Cicha, I., Jüngst, T. and Groll, J., 2021. Melt electrowriting of isomalt for high-resolution templating of embedded microchannels. Advanced Materials Technologies, 6(8), p.2100221					
Figure	**Author Initials,** Responsibility decreasing from left to right				
Scheme 1	AN				
1	AN				
2	AN				
3	AN				
Supporting Figure 1	AN				
Supporting Figure 2	AN				
Supporting Figure 3	AN				
Table	**Author Initials,** Responsibility decreasing from left to right				
1	AN				

Manuscript 2 (complete reference): Ryma, M.*, Genç, H.*, Nadernezhad, A.*, Paulus, I., Schneidereit, D., Friedrich, O., Andelovic, K., Lyer, S., Alexiou, C., Cicha, I. and Groll, J., 2022. A print-and-fuse Strategy for Sacrificial Filaments Enables Biomimetically Structured Perfusable Microvascular Networks with Functional Endothelium Inside 3D Hydrogels. Advanced Materials, p.2200653.					
Figure	**Author Initials,** Responsibility decreasing from left to right				
1	AN	MR			
3	AN	HG			
Supporting Figure 8	AN				
Supporting Figure 9	AN				
Table	**Author Initials,** Responsibility decreasing from left to right				
1	MR	AN			
2	AN				
Supporting Table 2	AN				
Supporting Table 3	AN				
Supporting Table 4	AN				
Supporting Table 5	AN				
Supporting Table 6	AN				

Explanations: * equally shared author contributions

Manuscript 3 (complete reference): Nadernezhad, A., Forster, L., Netti, F., Adler-Abramovich, L., Teßmar, J. and Groll, J., 2020. Rheological analysis of the interplay between the molecular weight and concentration of hyaluronic acid in formulations of supramolecular HA/FmocFF hybrid hydrogels. Polymer Journal, 52(8), pp.1007-1012.					
Figure	**Author Initials,** Responsibility decreasing from left to right				
1	AN				
2	AN				
Table	**Author Initials,** Responsibility decreasing from left to right				
1	AN	LF			
2	AN				

Manuscript 4 (complete reference): Nadernezhad, and Groll, J., 2022. Machine learning reveals a general understanding of printability in formulations based on rheology additives. Advanced Science, p.2202638.					
Figure	**Author Initials,** Responsibility decreasing from left to right				
Scheme 1	AN				
1	AN				
2	AN				
3	AN				
4	AN				
5	AN				
6	AN				
Supporting Figure 1	AN				
Supporting Figure 2	AN				
Supporting Figure 3	AN				
Supporting Figure 4	AN				
Table	**Author Initials,** Responsibility decreasing from left to right				
1	AN				
2	AN				
Supporting Table 1	AN				
Supporting Table 2	AN				

I also confirm my primary supervisor's acceptance.

Ali Nadernezhad 23.10.2022 Dresden

_____

Doctoral Researcher's Name Date Place Signature

Table of Contents

Abbreviation and Symbol Index

Abbreviation	Meaning	Annex
3IOT	3-Interval Oscillatory Test	
3ITT	3-Interval Thixotropy Test	
AM	additive manufacturing	
ANOVA	analysis of variance	
AI	artificial intelligence	
bFGF	basic fibroblast growth factor	
R^2	coefficient of determination	
CAD	computer-aided design	
CTS	critical translation speed	
DF	damping factor	
DSC	differential scanning calorimetry	
DMSO	dimethylsulfoxide	
EHD	electrohydrodynamic	
EC	endothelial cell	
et al.	et alii	and others
ECM	extracellular matrix	
GelMA	gelatin-methacryloyl	
GAGs	glycosaminoglycans	
HAC	HA-Carbopol	
HAF	HA-Fmoc-FF	
HAL	HA-Lapointe XLG	
HA	hyaluronic acid	
HIF-1	hypoxia-induced factor-1	
i.e.	id est	which means
LAP	Lithium-phenyl-2,4,6-trimethylbenzoylphosphinat	
LMWG	low molecular weight gelator	
LCST	lower critical solution temperature	
ML	machine Learning	
MMPs	matrix metalloproteinases	
MES	melt electrospinning	
MEW	melt electrowriting	
Fmoc-FF	N-fluorenylmethoxycarbonyl diphenylalanine	
PD	partial dependence	
PDP	partial dependence plot	
PBS	Phosphate-buffered saline	

Abbreviation	Meaning	Annex
PDGF	platelet-derived growth factor	
P*cyclo*PrOx	poly(2-cyclopropyl-2-oxazoline)	
PGA	poly(l-glutamic acid)	
PCL	polycaprolactone	
PDMS	polydimethylsiloxane	
PEG	polyethylene glycol	
PS	polystyrene	
PU	polyurethane	
PI	prediction Interval	
PSPP	processing-structure-properties-performance	
RF	random Forest	
RH	relative humidity	
RSM	response surface methodology	
SWIFT	sacrificial writing into functional tissues	
SHAP	Shapley additive explanations	
SES	solution electrospinning	
G	storage modulus	
TG	thermal gravimetric	
3D	three-dimensional	
TGF-β	transforming growth factor-β	
TNF-α	tumor necrosis factor alpha	
2D	two-dimensional	
VEGF	vascular endothelial growth factor	
versus	vs.	as opposed to
GPM	α-D-glucopyranosyl–1-6-mannitol	
GPS	α-D-glucopyranosyl–1-6-sorbitol	

Symbol	Meaning
°	degree
%	percent
°C	degree Celsius
M_W	Molecular weight
T_g	glass transition temperature
T_M	melting temperature

Acknowledgments

My stay at Würzburg was an adventure with many ups and downs. The gift was having some old friends' support and meeting new people, to whom I shall express my deepest gratitude and sincere regards.

I would like to express my earnest gratitude to Prof. Dr. Jürgen Groll for his trust in me and my capabilities and for giving me the freedom to explore, grow, and become a wiser and better version of myself. I appreciate his support and remain grateful for his patience during challenging times. Many thanks to Prof. Dr. Iwona Cicha, who enriched my experience by being a model of an independent and resilient scientist; she simply never gave up on hope, and I learned from her that there will always be a way.

I am immensely thankful to Dr. Ferdows Afghah, whose support and friendship were always present with no hesitations. She proved to be a great companion at times of happiness and hardship. I will be forever grateful for her kindness.

I would like to thank Dr. Matthias Ryma for his company during the course of my work on the SFB-TRR225/B02 project. We shared many tough and challenging times when we could easily give up, but we kept trying.

I had the opportunity to meet Dr. Mehmet Berat Taskin, Alessandro Cianciossi, Friederike Kaiser, and Dr. Taufiq Ahmad. We spent many hours with each other, shared our stories, tried our best to help each other, and created many good memories. I will remain grateful for their friendship and wish them all the best throughout their lives.

Writing while being full-time employed wasn't easy; I appreciate the support and positive attitude of Verena Kast during the writing of this dissertation.

I am greatly indebted to my family for their support throughout my career, especially my mother, who always believed in me and encouraged me to excel. She was a teacher; she always taught me to be curious about life, and I always tried to be her best student.

Summary / Zusammenfassung

Summary

To successfully mimic the complexities of tissues *in vitro* by using biofabrication technologies, many parameters and conditions should be considered and implemented correctly. Vascularization in biofabrication is the main frontier to face when the size of constructs passes the limits of diffusion *in vivo*, and to ensure the delivery of nutrients and oxygen on a bulk scale, creating a network of artificial vascular structures is necessary. Deploying complex vasculatures often demands a convergence between multiple biofabrication technologies, and current literature is showing an interest in using hybrid platforms and strategies to address this challenge. However, novel approaches should be engineered to enable such possibilities, and a deeper understanding of the existing technologies should be provided to use the current methods at their maximum potential.

The **overall focus of this doctoral thesis** was twofold, to implement engineering methods for optimization and evaluation of major parameters in creating artificial microvascular structures using Melt Electrowriting (MEW)-assisted sacrificial templating; and to further advance the knowledge on the contributing factors that define printability of bioinks formulations using 3D extrusion bioprinting.

In the first part of this thesis, two different sacrificial templating methods by MEW were presented. **Chapter 2** introduced a sacrificial templating method using carbohydrate glass to create geometrically controlled embedded microchannels. The main objective of this study was to push the limits of using carbohydrate glasses as fugitive materials for templating microchannels with sub-100-micron dimensions in a reproducible manner. By using Isomalt as the fugitive material, this study pioneered the processing of sugars with MEW, enabling the fabrication of sacrificial structures with unprecedented resolution. A systematic variation of process parameters showed that complex perfusable microchannel architectures with a controlled diameter could be fabricated in a single design.

Chapter 3 presented the results of a novel method to create perfusable and biomimetically designed microvasculatures within bulk hydrogel bodies. The presented approach, the print-and-fuse strategy, resulted in forming perfusable branching microchannels, which approximate Murray's law in the geometrical ratio between parent and daughter vessels. This methodology benefited from the spontaneous merging and plasticity of sacrificial thermoresponsive poly(2-cyclopropyl-2-oxazoline) structures produced by MEW in aqueous environments above their lower critical solution temperature. Optimized by response surface methodology, it was possible to create

complex branching patterns of fugitive structures in a predictable manner. The interconnected branched microvessels could be further endothelialized, and the flow profiles within the microchannels mimicked the *in vivo* conditions. This novel integrative approach has been proven to be an essential step toward one-step fabricating vascularized *in vitro* platforms with functional endothelium inside bulk hydrogels.

By considering extrusion bioprinting as a complementary approach to MEW in a multi-technology biofabrication, a deeper understanding of the role of bioink physical properties in its success is crucial. With this goal in mind, two studies focused on the role of rheology modifiers in inducing printability and injectibility in bioinks were presented in the second part of this thesis.

In **Chapter 4**, it was shown that changing a few inherent characteristics of a simple two-component formulation could significantly influence the physical properties of the final bioink. It was shown that when using low molecular weight gelator peptides, the complex relationships between molecular weight and concentration of hydrogel component drive the gelation kinetics and the evolution of viscoelasticity in the formulations and their plastic flow.

Taking a step further, it was shown in **Chapter 5** that a generalized understanding of the concept of printability in formulations based on rheology modifiers could be drawn by using sophisticated statistical approaches. Using state-of-the-art descriptive machine learning methodologies, it was possible to shed light on the hidden correlations between major physical characteristics of bioinks, which collaboratively contribute to the transition from a non-printable material to a printable one. This study was the first to address the lack of in-depth knowledge about the printability of hydrogel bioinks used in extrusion-based biofabrication. The results of this study highlighted that 13 critical rheological and physical factors determine the outcome of printability assessments, and by using these findings, new tools for designing and engineering printable materials can be accessible. Moreover, the descriptive nature of the findings of this study could benefit future research toward automated biofabrication technologies.

In conclusion, a deeper insight into some fundamental aspects of two leading biofabrication technologies was derived during this dissertation. The contributing studies can be extended in the future to converged hybrid biofabrication approaches for creating vascularized constructs, where the geometrical precision of MEW fabricated sacrificial templates can be incorporated into an automated extrusion-based bioprinting approach, in which the process parameters could be tuned based on the knowledge of the printability in a given bioink formulation.

Zusammenfassung

Um die Komplexität von Geweben *in vitro* mit Hilfe von Biofabrikationstechnologien erfolgreich nachzubilden, müssen viele Parameter und Bedingungen berücksichtigt und korrekt umgesetzt werden. Die Vaskularisierung in der Biofabrikation ist die wichtigste Herausforderung, wenn die Größe der Konstrukte die Grenzen der Diffusion *in vivo* überschreitet. Um die Versorgung mit Nährstoffen und Sauerstoff in großem Maßstab zu gewährleisten, ist die Schaffung eines Netzwerks künstlicher Gefäßstrukturen erforderlich. Der Aufbau komplexer Gefäßstrukturen erfordert oft eine Konvergenz zwischen verschiedenen Biofabrikationstechnologien. Die aktuelle Literatur zeigt ein Interesse an der Verwendung hybrider Plattformen und Strategien, um diese Herausforderung zu bewältigen. Es sollten jedoch neue Ansätze entwickelt werden, um solche Möglichkeiten zu ermöglichen, und es sollte ein tieferes Verständnis der bestehenden Technologien geschaffen werden, um die derzeitigen Methoden optimal nutzen zu können.

Der **Fokus der Doktorarbeit** lag auf der Implementierung von Methoden zur Optimierung und Bewertung der wichtigsten Parameter bei der Herstellung künstlicher mikrovaskulärer Strukturen durch Melt Electrowriting (MEW)-unterstütztes Opfer-Templating und auf der Erweiterung des Wissens über die Faktoren, die die Druckbarkeit von Biotintenformulierungen durch 3D-Extrusions-Bioprinting bestimmen.

Im ersten Teil dieser Arbeit wurden zwei verschiedene Methoden der Opferschablonierung durch MEW vorgestellt. In **Kapitel 2** wurde eine Opfer-Templating-Methode unter Verwendung von Kohlenhydratglas vorgestellt, um geometrisch kontrollierte eingebettete Mikrokanäle zu erzeugen. Das Hauptziel dieser Studie war es, die Grenzen der Verwendung von Kohlenhydratgläsern als flüchtige Materialien für die reproduzierbare Herstellung von Mikrokanälen mit Abmessungen unter 100 Mikrometern zu erweitern. Durch die Verwendung von Isomalt als flüchtiges Material leistete diese Studie Pionierarbeit bei der Verarbeitung von Zuckern mit MEW und ermöglichte die Herstellung von Opferstrukturen mit noch nie dagewesener Auflösung. Eine systematische Variation der Prozessparameter zeigte, dass komplexe, durchlässige Mikrokanalarchitekturen mit einem kontrollierten Durchmesser in einem einzigen Design hergestellt werden konnten.

In **Kapitel 3** wurden die Ergebnisse einer neuartigen Methode zur Herstellung durchblutbarer und biomimetisch gestalteter Mikrogefäße in Hydrogelkörpern vorgestellt. Der vorgestellte Ansatz, die Print-and-Fuse-Strategie, führte zur Bildung von durchblutbaren, sich verzweigenden Mikrokanälen, die im geometrischen Verhältnis

zwischen Mutter- und Tochtergefäßen dem Murray'schen Gesetz nahe kommen. Diese Methode profitierte von der spontanen Verschmelzung und Plastizität der thermoresponsiven Poly(2-cyclopropyl-2-oxazolin)-Opferstrukturen, die durch MEW in wässriger Umgebung oberhalb ihrer unteren kritischen Lösungstemperatur hergestellt wurden. Durch die Optimierung mit Hilfe der Response-Surface-Methode war es möglich, komplexe Verzweigungsmuster der flüchtigen Strukturen auf vorhersehbare Weise zu erzeugen. Die miteinander verbundenen verzweigten Mikrogefäße konnten weiter endothelialisiert werden, und die Strömungsprofile innerhalb der Mikrokanäle ahmten die Bedingungen *in vivo* nach. Dieser neuartige integrative Ansatz hat sich als wesentlicher Schritt zur schrittweisen Herstellung von vaskularisierten In-vitro-Plattformen mit funktionellem Endothel innerhalb von Hydrogelen erwiesen.

Wenn man das Extrusions-Bioprinting als komplementären Ansatz zur MEW in einer Multitechnologie-Biofabrikationsstrategie betrachtet, ist ein tieferes Verständnis der Rolle der physikalischen Eigenschaften der Biotinte für ihren Erfolg von entscheidender Bedeutung. Mit diesem Ziel vor Augen wurden im zweiten Teil dieser Arbeit zwei Studien vorgestellt, die sich mit der Rolle von Rheologiemodifikatoren für die Druckbarkeit und Injektionsfähigkeit von Biotinten befassten.

In **Kapitel 4** wurde gezeigt, dass die Veränderung einiger inhärenter Eigenschaften einer einfachen Zweikomponentenformulierung die physikalischen Eigenschaften der fertigen Biotinte erheblich beeinflussen kann. Es wurde gezeigt, dass bei der Verwendung von Gelatorpeptiden mit niedrigem Molekulargewicht die komplexen Beziehungen zwischen Molekulargewicht und Konzentration der Hydrogelkomponente die Gelierkinetik und die Entwicklung der Viskoelastizität in den Formulierungen und deren plastisches Fließen bestimmen.

In einem weiteren Schritt wurde in **Kapitel 5** gezeigt, dass ein verallgemeinertes Verständnis des Konzepts der Bedruckbarkeit von Formulierungen, die auf Rheologiemodifikatoren basieren, mit Hilfe ausgefeilter statistischer Ansätze gewonnen werden kann. Mit Hilfe modernster deskriptiver Methoden des maschinellen Lernens war es möglich, die verborgenen Korrelationen zwischen den wichtigsten physikalischen Eigenschaften von Biotinten zu beleuchten, die gemeinsam zum Übergang von einem nicht bedruckbaren Material zu einem bedruckbaren Material beitragen. Diese Studie war die erste, die das fehlende Wissen über die Druckbarkeit von Hydrogel-Biotinten für die extrusionsbasierte Biofabrikation aufdeckte. Die Ergebnisse dieser Studie haben gezeigt, dass 13 kritische rheologische und physikalische Faktoren das Ergebnis der Bewertung der Druckbarkeit bestimmen, und durch die Nutzung dieser Erkenntnisse können neue Werkzeuge für das Design und die Entwicklung druckfähiger Materialien

zugänglich gemacht werden. Darüber hinaus könnte der deskriptive Charakter der Ergebnisse dieser Studie der zukünftigen Forschung im Bereich der automatisierten Biofabrikationstechnologien zugute kommen.

Zusammenfassend lässt sich sagen, dass im Rahmen dieser Dissertation ein tieferer Einblick in einige grundlegende Aspekte zweier führender Biofabrikationstechnologien gewonnen wurde. Die beitragenden Studien können in Zukunft auf konvergierte hybride Biofabrikationsansätze zur Herstellung vaskularisierter Konstrukte ausgeweitet werden, bei denen die geometrische Präzision von MEW-gefertigten Opferschablonen in einen automatisierten extrusionsbasierten Bioprinting-Ansatz integriert werden kann, bei dem die Prozessparameter auf der Grundlage der Kenntnis der Druckbarkeit in einer bestimmten Biotintenformulierung abgestimmt werden können.

Chapter 1

State of knowledge and the aims of this thesis

1.1 Vascularization within the context of tissue engineering

Despite the century-long history of two-dimensional (2D) cell culture methods, the three-dimensional (3D) cell culture techniques show convincing evidence that more advanced readouts with higher mimicry of *in vivo* conditions could be experimentally conceived [1]. Different approaches of scaffold-based and scaffolds-free techniques showed the potential of 3D cell culture methods to study organ-level behavior, promising to fill the gap in the transition from 2D cell culture to animal models [1]. If appropriately designed, 3D culture methods can imitate the biochemical and biomechanical signaling in the extracellular matrix (ECM) and model the tissues' cellular heterogeneity within the temporal and spatial context of ECM. However, rendering such characteristics in 3D demands establishing an optimal and continuous supply of nutrients, oxygen, and signaling factors.

Delivery of nutrients and waste removal is the primary function of the vascular system in living tissues. The hierarchical and dynamically reforming vascular network comprises multi-scale vessels with several orders of magnitudes diameter range designed to deliver oxygen beyond the diffusion limit *in vivo* [2]. Mimicking the intricate and complex architecture of the natural vascular system *in vitro* proved tedious, and as a result, vascularization is considered one of the primary challenges in many regenerative, therapeutic, and diagnostic approaches based on tissue engineering principles.

The formation of vascular structures *in vivo* can occur through angiogenesis and vasculogenesis. The former refers to the formation of new blood vessels from preexisting ones, and the latter describes the generation of new vascularization in the absence of blood vessels which generally includes the formation of new capillaries during embryologic development. *In vitro*, 2D vascularization is usually accomplished by either imposing specific patterns on culture substrates or subjecting cells to angiogenic factors to stimulate neovascularization. However, the technical complexity of this process increases proportionally by moving from 2D to 3D culture systems. The generation of stable microvascular structures in 3D is not only a matter of triggering the rapid proliferation of endothelial cells (ECs), but a mature microvascular structure demands ECs proliferation, interconnected capillary network formation, and recruitment of mural cells [3].

The main approaches for *in vitro* generation of 3D microvascular networks involve self-conducting and self-regulating angiogenesis by supplementing bioactive signaling components in the 3D matrix or using the directed organization by providing solid support guidance or biochemical patterning. The self-conducting angiogenesis involves multiple

stages of vasculogenic assembly, sprouting angiogenesis, and vascular remodeling. Several molecular signaling mechanisms are implicated throughout the early stages of angiogenesis, followed by cell-cell instructive signaling and ECM remodeling during sprouting and the essential biophysical triggering of regulatory signaling in the remodeling phase [4]. In contrast to self-conducting angiogenesis, the directed organization relies on pre-defined microenvironmental cues patterned within the matrix. The migration and invasion of ECs toward the surrounding matrix depend significantly on the cells' adhesion to the ECM and microenvironment sensing. With this in mind, various microenvironmental cues could be engineered to evoke desired EC behavior and vascularization outcome. These cues include bioactive materials, oxygen tension, and biophysical features of the matrix [5].

Directed organization of the microvascular system provides the advantage of controlling the network's extent and form in engineered constructs, regardless of the intended use *in vitro* or *in vivo*. Pro-angiogenic components of natural ECM, such as type I collagen [6, 7] and fibrin [8], play a vital role in engaging and guiding ECs. Extracts of the natural ECM of vascular tissue [9, 10] and the basement membrane [11] showed pro-angiogenic properties, although the complexity in composition might obscure the underlying mechanism and restrict the application. In contrast, modified natural polymers or synthetic biomaterials offer tunability of physicochemical properties and can selectively host natural pro-angiogenic factors [11, 12]. Additionally, exploiting the innate natural angiogenesis mechanisms in response to hypoxia [13] proved valuable in developing vascularization strategies. Delivery of hypoxia-induced factor-1 (HIF-1), as the primary transcriptional mediator expressed by ECs subjected to oxygen stress, exposure to short-term cyclic hypoxia, and hypoxic culture were found to promote neovascularization and differentiation of stem cells into ECs [14-16]. Moreover, the biophysical properties of the microenvironment could significantly alter and control the formation of the microvascular system. Static biophysical properties such as topology of the matrix, stiffness, and internal architecture showed the most significant impact on angiogenesis in a 3D matrix [17-21], and dynamic biophysical cues such as fluid shear stress [22-24] and electrical stimulation [25] are proved to be directly related to the development of the EC monolayer in microvasculatures.

In vivo, biophysical and biochemical cues for vascularization usually coexist and often collaborate. Inspired by this, vascularization strategies to engineer 3D tissue constructs could be based on incorporating multiple stimuli. Among them, approaches based on the simultaneous incorporation of static biophysical cues and bioactive materials are of particular interest, considering the recent technological advances in controlling the

topographic features of the scaffolds and the possibility of tuning the biochemical properties of the matrices.

1.1.1 Bioactive materials to stimulate angiogenesis

Using the knowledge about the vascular niche and its regulatory role in tissue regeneration, engineered biomaterials can promote and guide angiogenesis in regenerative, therapeutic, and diagnostic platforms. Several categories of bioactive and instructive materials for angiogenesis could be formed depending on the presence of bioactive modalities, the inherent bio-functionality of a biomaterial, and its natural or synthetic nature. In the most general form, bioactive materials for guiding angiogenesis are classified based on their natural or synthetic source.

Naturally derived bioactive materials include collagen and its derivatives, fibrin, glycosaminoglycans (GAGs), or complex ECM components such as Matrigel®. Collagen is an abundant component across various tissue microenvironments and supports endothelial network formation [26, 27]. However, the thrombogenic potential, higher risk of immunogenicity, and difficulties in controlling collagen gelation and mechanical properties led to more interest in using its derivative, gelatin. Although gelatin lacks collagen's fibrillar microstructure, it has rich biochemistry that can be modified to tune biochemical and biophysical properties [28-31].

Hydrogels from fibrin can promote angiogenesis and the formation of natural vasculature [32], and it was shown that the dynamics of vascularization in fibrin hydrogels could be controlled by engineering the integrin-binding protein sequences [33]. Matrices derived from GAGs for *in vitro* and *in vivo* vascularization mainly include hyaluronic acid (HA) hydrogels. Although HA does not have any integrin-binding or matrix metalloproteinases (MMPs) sensitive sites, it has great potential for chemical modification and tuning of the biochemical and biomechanical presentation [34] and further incorporation as a matrix to induce targeted angiogenesis [35]. Other polysaccharides such as alginate [36, 37] and dextran [38, 39] have also been used to guide and stimulate angiogenesis *in vitro* and *in vivo*, although they lack the essential cell-interaction motifs and require further modifications depending on the application. The excellent pro-angiogenic property of Matrigel® placed this component as the standard substrate material for EC tube formation assay [40].

Synthetic bioactive materials offer highly tunable chemical and mechanical properties and the capacity to be bundled with natural pro-angiogenic agents. Among them, polyethylene glycol (PEG) [41-44], its blends [45-47] and PEGylated peptides [48-50], polycaprolactone (PCL) [51, 52], poly(l-glutamic acid) (PGA) [53], and elastomeric

polyurethane (PU) [54] showed high angiogenic capacity and supporting multiple cell-types to harness tissue level mimicry of the microenvironment. Despite the usefulness of synthetic bioactive materials for the mechanistic study of angiogenesis and controlling the effect of individual matrix properties, they fall short in stimulating native cell behavior, as usually they can not capture the complexity of ECM to its fullest extent.

The current state of the literature shows that neither natural nor synthetic bioactive materials deliver an optimal angiogenesis performance exclusively, and strategies incorporating combined offerings of two categories could harness the advantages of each category and compensate for some of the limitations [47, 51]. Diversifying the pool to select candidate bioactive materials presents an excellent opportunity to engineer and tune the outcome of vascularization. The hybrid approach for selecting bioactive materials for angiogenesis is discussed in section 1.4.1.

1.1.2 Biophysical cues to guide angiogenesis

Results of several studies showed that biophysical cues could significantly alter and guide the outcome of angiogenesis, even independently from the selection of biomaterials. Among them, surface (micro) topography, porosity, stiffness, and hydrodynamic stress have been studied comprehensively.

It has been demonstrated that surface topography significantly impacts the behavior of different cell types [18, 55]. In addition to various topographies such as pillars, pits, grooves, tubes, fibers, and roughness, features' curvature and direction play an essential role in cellular proliferation and migration [18, 56]. Micro-textured substrates could increase vascular invasion *in vivo* [57], while ECs tend to elongate and migrate in the direction of aligned collagen nanofibrils [19]. Nanofibrillar collagen scaffolds seeded by EC improved blood perfusion and arteriogenesis in a mouse model [20]. While the most impactful surface topographies on vascularization have a scale of below a few microns, the surface curvature with the scales much larger than cells was found to influence the angiogenesis behavior significantly [58].

Structural porosity is an efficient way to control and guide cell infiltration and delivery of oxygen, nutrients, and waste removal. On the microscale, porosity can be created using freeze-drying, particulate templating, and biofabrication methods, which could be applied to hydrogels and polymers. Pore size and architecture could significantly influence cell behavior [58, 59]. *In vitro* studies showed that the cells tend to invade more in areas of large pore size, and *in vivo* results showed that the density of newly formed blood vessels is higher in areas with large pores [60]. Additionally, pore size can modulate angiogenic paracrine activity by influencing cell-cell interactions [61].

The matrix's density and stiffness can influence the vasculature's extent and remodeling capacity. Increased stiffness increases individual EC spreading and the number and length of outgrowths in ECs spheroids [62]. Usually coupled with matrix stiffness, matrix density directly influences vascularization, and increased matrix density reduces capillary formation *in vitro* [63, 64].

Hydrodynamic shear stress is another critical biophysical factor guiding angiogenesis and vascularization. Although mostly related to the post-lumenization of vessels, studies showed that the endothelial barrier integrity and permeability are significantly influenced by the flow-exerted shear stress [65, 66]. Moreover, the applied shear stress could impact the signaling cascades within ECs and their gene expression [65, 67].

1.2 Deployment of guided vascularization in 3D matrices

Fabrication of vascularized 3D matrices is generally divided into two main categories, "bottom-up" and "top-down" strategies (**Figure 1**). The decisive factor in separating fabrication approaches is the involvement of the process of tubulogenesis [68]. The bottom-up approaches are generally based on encapsulating ECs in a 3D matrix, followed by spontaneous and self-regulated microvascular network formation through vasculogenesis and angiogenesis. This process requires tubulogenesis during vasculogenesis and angiogenesis to form the lumens. The bottom-up approaches are usually slow, and the network architecture is usually challenging to control [69]. The bottom-up approaches mainly rely on bioactive materials to guide and direct angiogenesis. However, biophysical factors such as matrix stiffness and fluid flow are critical [70]. Natural components of ECM and synthetic substitutes have been widely used to stimulate and guide angiogenesis [11], and different growth factors and their gradients were employed to promote neovascularization [70]. Among them, vascular endothelial growth factor (VEGF), basic fibroblast growth factor (bFGF), platelet-derived growth factor (PDGF), and transforming growth factor-β (TGF-β) have been extensively explored [36, 71-73]. Growth factors could be physically or chemically immobilized within the matrix, and their spatial and temporal delivery can be tuned to control the process of angiogenesis [74-80].

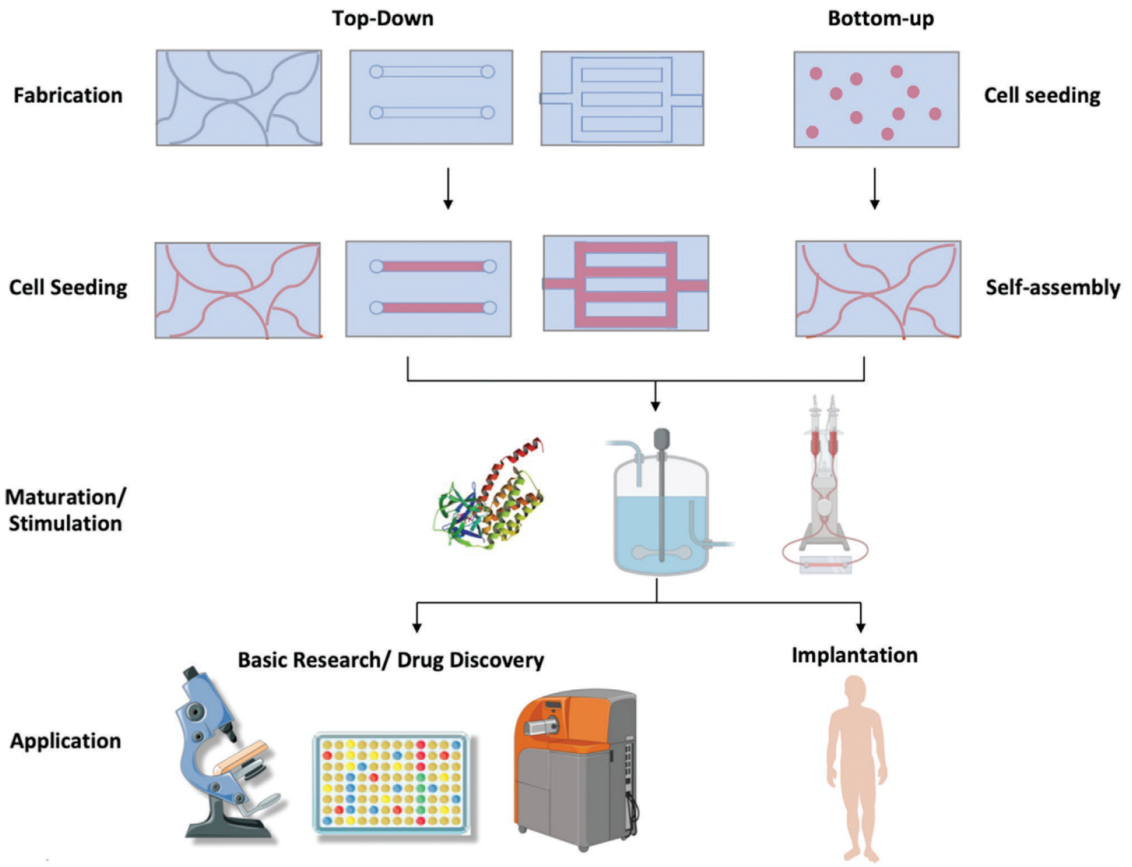

Figure 1. **Engineered meso- and microvasculature.** Approaches to engineering meso- and microvasculature can be divided into top-down and bottom-up approaches. In top-down, the vasculature is predesigned, while bottom-up relies on cellular and extracellular stimuli to promote vessel formation. The vasculature can be further matured or stimulated to induce sprouting to generate a stable and functional vascular network then. Both approaches generate *in vitro* vasculature models for basic research and drug screening applications and/or vascularizing tissues for regenerative medicine applications. Reproduced from reference [70] with permission from Wiley-VCH.

In contrast to bottom-up approaches, the top-down methods mainly rely on patterned microstructures to guide ECs to form microvessels. Traditionally, porous scaffolds were used as the microenvironment to guide vascularization through solid support angiogenesis guidance. The porosity of scaffolds and the geometrical aspects such as pore size, distribution, and morphology can critically influence the outcome of vascularization [81]. However, it became evident that the orientation of pores is the determinant factor for the accurate control over the newly formed vasculature, and the tubular channels were promoting vascularization more efficiently than random pore architectures [82]. Efficient perfusion of liquids through the oriented (micro)channels accelerates the delivery rate of nutrients and waste removal [82]. Moreover, hollow microchannels could act as physical cues and guide tissue ingrowth into the scaffolds [83]. It is also shown that the density of vasculature *in vivo* is higher in scaffolds patterned with microchannels [84].

In order to create oriented pore structures and microchannels, different patterning technologies were used. Among them, microfluidic vascularization and biofabrication-based approaches have been extensively explored. Microfluidic vascularization was mainly developed to address a need for quantitative angiogenesis assays [85]. Moreover, well-controlled microenvironments and *in vivo* relevant dimensions of microchannels made microfluidic-based vascularization models very attractive for researchers [86]. However, microfluidic platforms for studying angiogenesis usually are limited to *in vitro* assays with less control over the architecture of the formed vascular networks.

With the recent progress in biofabrication, various methods based on biofabrication principles are actively utilized to guide angiogenesis for regenerative and diagnostic applications. Biofabrication refers to *"the automated generation of biologically functional products with structural organization from living cells, bioactive molecules, biomaterials, cell aggregates such as macro-tissues, or hybrid cell-material constructs, through bioprinting or bioassembly and subsequent tissue maturation processes"* [87]. Several biofabrication technologies, including laser-based technologies, extrusion-based 3D bioprinting, inkjet printing, and solution or melt electrospinning, could be highlighted for vascularization. More details about these fabrication methodologies are provided in the next section.

1.2.1 Biofabrication as a tool for controlled vascularization

Most biofabrication technologies stem from additive manufacturing (AM) principles. Being faithful to AM principles, the classifications of different biofabrication methods result in six major categories (**Figure 2**). These categories comprise (i) laser-based technologies, (ii) 3D printing, (iii) fused deposition modeling, (iv) inkjet printing, (v) 3D plotting, and (vi) solution or melt electrospinning [88]. In each category, modifications and adaptations of the underlying working principles were made to maximize the compatibility and applicability of the respective methods to meet the desired geometrical, biophysical, and biological needs in the biofabrication strategy.

The details regarding each of these methodologies are out of the scope of this work. However, a number of them showed great potential to be implemented as a part of the strategies for controlled vascularization. With the main objective of creating hollow channels within the bulk of biofabricated constructs, templating methods in the bulk of hydrogels have gained significant attention throughout the past years. Rather than focusing on a particular technology, the choice of strategies to create a microvascular structure is of great importance, as it could determine the needs and the outcome of the

vascular network formation. Focusing on creating hollow channeled patterns, the main biofabrication strategies for vascularization involve sacrificial bioprinting, embedded extrusion bioprinting, hollow fiber bioprinting, and stereolithographic bioprinting [92].

In sacrificial bioprinting, the aim is to create hollow channels by templating a secondary “removable” phase using different biofabrication technologies. After templating, the sacrificial phase will be removed through different mechanisms; the most common ones include temperature-triggered selective dissolution, and extraction by physical force using pulling or mild vacuum [93-97]. The resultant hollow lumens will be further seeded with ECs and perfused.

The embedded extrusion bioprinting methodology is based on the deposition of hydrogels in a medium other than air, which will support the deposited ink through the viscoelasticity of the medium [98-100]. By tuning the physical properties of the supporting medium, channeled structures with a high level of detail could be resolved, and by subsequent removal of the supporting medium, ECs could be seeded in the hollow lumens and perfused. The main advantage of embedded extrusion bioprinting is the possibility of creating naturally branching structures, which proved challenging to realize in methods based on sacrificial bioprinting.

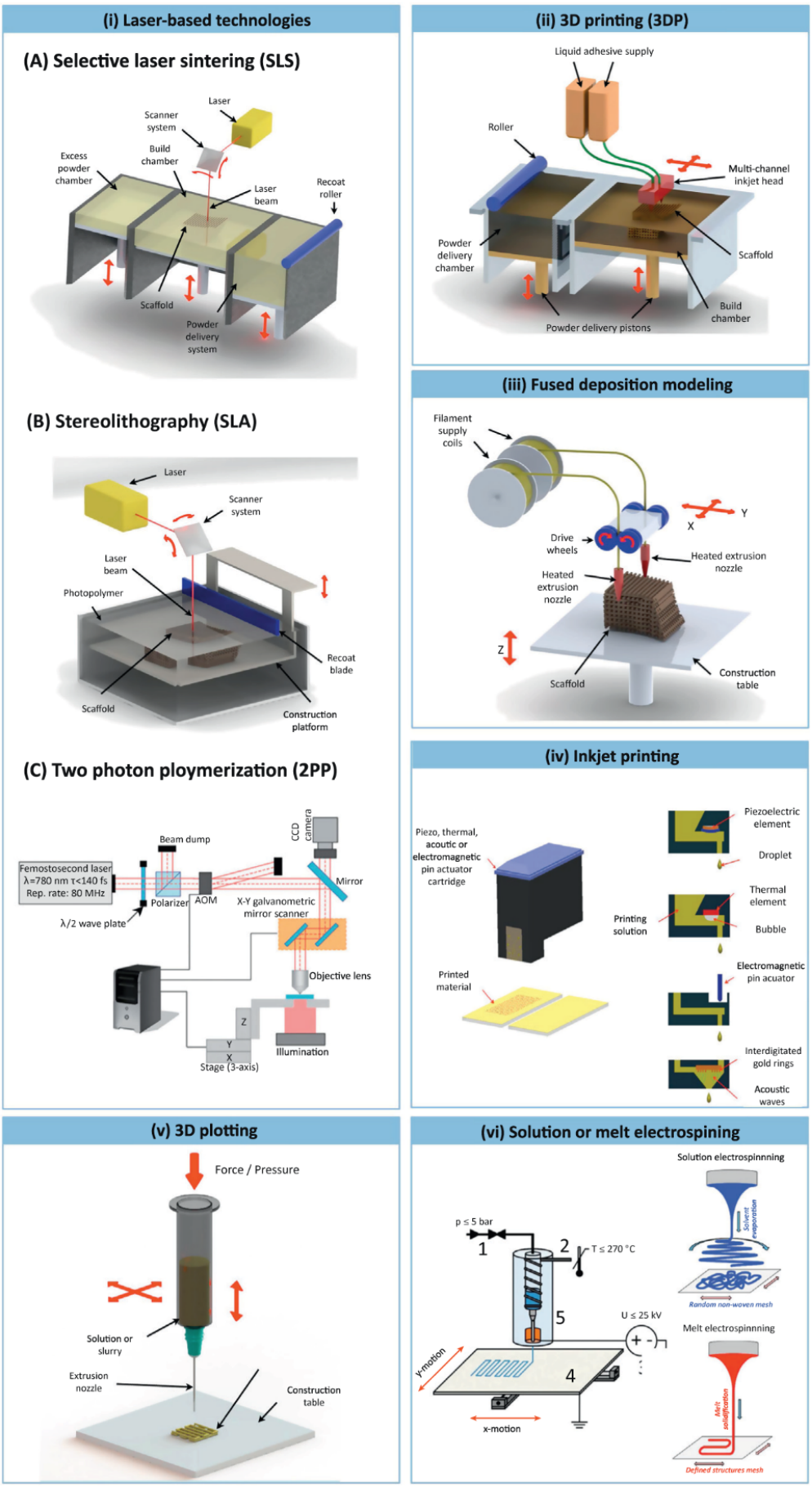

(Description on the next page)

Figure 2. Commonly Used Technologies in Biofabrication with a Major and Active Role of Biomaterials in the Printing Process. i) Light-based technologies (selective laser sintering, stereolithography, two-photon polymerization), **ii**) 3D printing, **iii**) fused deposition modeling, **iv**) ink-jet printing, **v**) 3D plotting, and **vi**) solution and melt electrospinning. [88-91] Reproduced from reference [88] with permission from Elsevier.

In contrast to multi-step processes based on sacrificial bioprinting and embedded extrusion bioprinting, hollow fiber bioprinting offers a facile and stand-alone process to fabricate single hollow channels that either host ECs laded in the wall structure or be seeded with ECs and perfused as vascular grafts [101-103]. Despite the feasibility and accessibility, hollow fiber bioprinting has significant limitations in creating branched and multi-scale vascular networks; hence its application could be limited to fabricating large, monotonously sized vessel structures.

Another approach for guided biofabrication of vascular networks is based on stereolithographic bioprinting methods. Stereolithographic bioprinting approaches allow the fabrication of large-scale vascularized structures with multi-scale hierarchical features. The principles of stereolithographic approaches include either patterned light illumination in a layer-by-layer fashion [104, 105] or, more recently, using a volumetric bioprinting approach [106, 107]. Regardless of the implemented technology, a 3D volume with a vascular network is obtained, and in addition to creating a 3D network, the surrounding matrices could be patterned with single or multiple cell types.

1.2.2 Biofabrication by sacrificial templating for guided vascularization

The spatial resolution of the biofabrication methods critically determines their applicability to be used for creating hollow microchannels. Different biofabrication methods can produce structures within different ranges of dimensional features, with overlaps between the different methods. These ranges include cell-relevant feature size to organ-level dimension, and a few methodologies can produce sub-nanometer scale structures and features (**Figure 3**). However, resolving dimensional features might not necessarily guarantee the intended function [108]. Despite the spatial resolution limitations of each biofabrication technology, compatibility with the maturation of cell-based strategies, and its exclusivity in the choice of processable materials must be considered [88]. In this way, a single biofabrication technology might not meet the requirements and demands of a specific design. Hybridization of manufacturing technologies has been the rational step toward expanding the application frameworks of each particular biofabrication technique [109]. The complexity and inherent hierarchy of natural cellular and tissue environments at different scales resulted in a trend in the literature toward utilizing multi-technology biofabrication approaches [109].

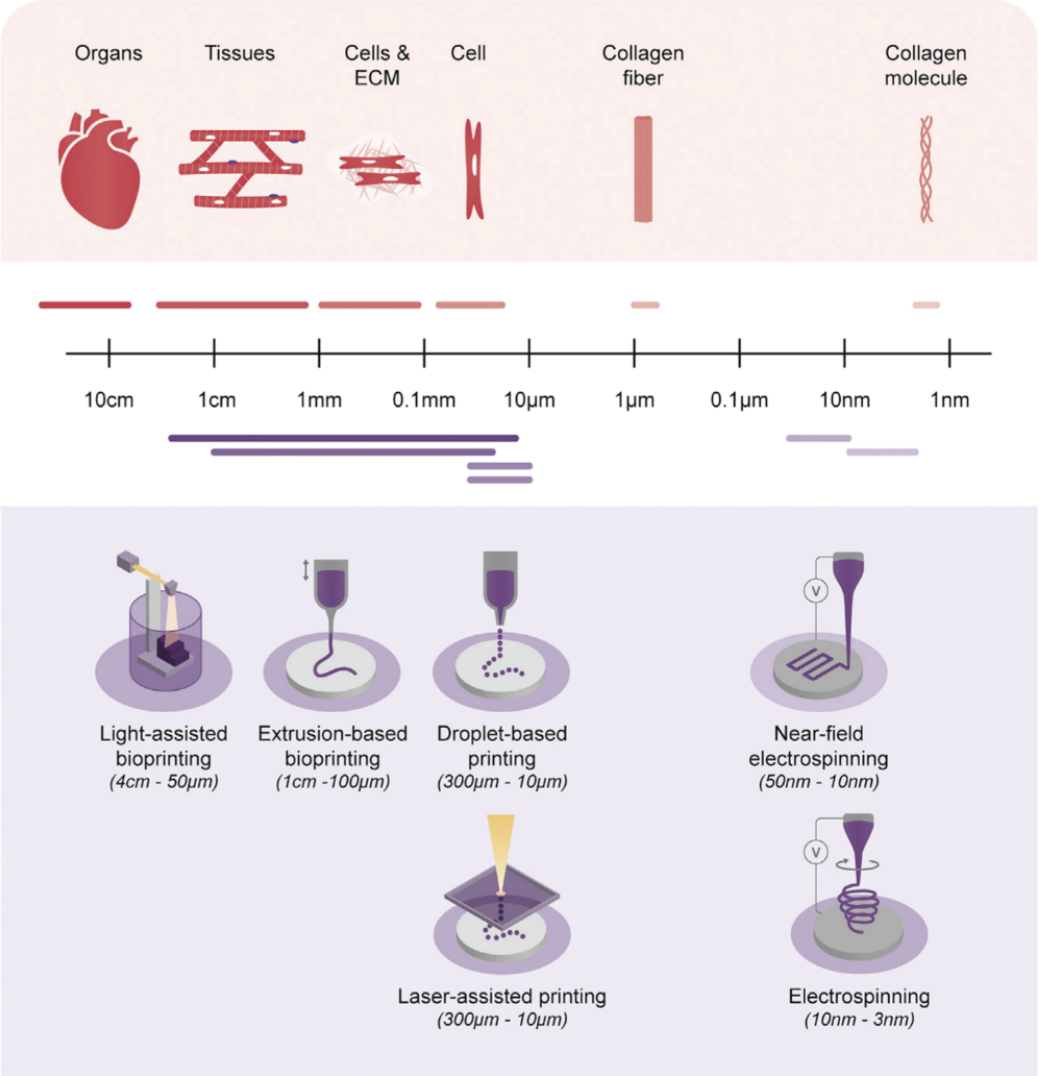

Figure 3. Schematic Illustration of Multi-technology Biofabrication. Comparison of the typical operation length of single deposition biofabrication technologies with the size and hierarchical structure of tissues and organs. Reproduced from reference [108] with permission from Elsevier.

To create hollow microchannels as a physical guide for vascularization, sacrificial templating shows the most potential either as a single or multi-technology approach. This is mainly due to the multi-step and multi-component nature of sacrificial bioprinting, involving the fabrication of the matrix and the templating structures. The early reports on using sacrificial printing to create microvasculature were based on the embedment of a previously fabricated interconnected network within a matrix of choice. The microvascular templating structure was fabricated in a separate step with either direct-write assembly [110, 111] or solution electrospinning [112]. Although the pioneering studies showed the potential of sacrificial templating in the fabrication of microfluidic networks in the bulk material, they were mainly restricted by the use of cytotoxic solvents or processing conditions for template removal or casting step, which restricted their applicability to acellular structures.

Cytocompatible removal of the sacrificial templates is one primary concern in selecting materials and designing the corresponding methodologies. The early works led by Jennifer Lewis's laboratory demonstrated sacrificial templating with the cytocompatible temperature-induced removal of the sacrificial templates [93, 113]. These sacrificial templates were mainly based on gelatin and Pluronic solutions, showing temperature-dependent solubility and gelation behavior. Following the same principles, this approach was further evolved into the direct sacrificial writing into functional tissues (SWIFT), based on the direct writing of sacrificial structures within a highly dense organ-specific cellular aggregate [114].

The SWIFT method, at its core, is a hybrid approach for creating microvascular structures by incorporating the principles of sacrificial bioprinting and embedded extrusion bioprinting. As a consequence of hybridization, the requirements of each fabrication technology might be applied to the hybrid method. A practical example of this process was in the SWIFT method [114], where tuning the rheological requirements of the cellular matrix and the sacrificial ink must be taken into account as a part of the requirements of embedded extrusion bioprinting.

The next breakthrough in biofabrication methods for vascularization involving sacrificial bioprinting was based on the incorporation of rigid water-soluble templating structures, mainly carbohydrate glasses, which could be processed and manufactured in a separate fabrication step. The fabrication methods involved 3D extrusion printing of carbohydrate glasses [115, 116] or selective laser sintering of granular carbohydrates [117]. The main advantage of these methods was the ease of removal of the sacrificial template by spontaneous dissolution in water and the improved handling of the sacrificial templated due to their rigidity. However, the water-solubility of carbohydrate glasses posed another challenge; the need to adapt matrix formation/consolidation with the rate of dissolution of sacrificial templates to preserve geometrical features. Coating methods based on polyesters were used to preserve the structural integrity of templating microstructures [115].

So far, 3D extrusion printing and direct writing are the main methods for fabricating sacrificial structures. In addition to the accessibility of 3D extrusion printing, its compatibility with a wide range of sacrificial materials contributed to its widespread use. However, limitations in reaching below 100-micron size features in extruded constructs pose a challenge in using these methods for templating microvascular structures. Although the technical advances in the field of additive manufacturing have facilitated reaching dimensions below 100-micron in a reproducible and stable manner, however,

to compensate for these limitations, additional costs and process complexities will be imposed.

Alternative methods for the fabrication of sacrificial structures were used to generate micron-scale sacrificial structures. Melt Electrowriting (MEW), one of the emerging biofabrication technologies, showed great potential in generating microchannels at the micron scale [118].

1.3 Melt Electrowriting (MEW) to fabricate sacrificial templates

MEW, at its core, involves the direct deposition of a polymer jet generated by the electrohydrodynamic (EHD) forces applied to a molten polymer reservoir [119, 120]. The structures produced by MEW possess low dimensions and a high surface-to-volume ratio. These structures are particularly interesting within the context of tissue engineering since their internal structure, size, porosity, and shape could be readily controlled to induce anticipated biological responses. Several factors play critical roles in the MEW process's outcome and mechanics, which are discussed in the following sections.

1.3.1 Working principles of MEW

The formation of a polymer jet during MEW results from several acting forces applied to a molten polymer reservoir. **Figure 4** provides a general overview of the acting forces on the deposited fibers and the core elements of a generic MEW platform. The primary phenomenon observed in MEW is similar to solution and melt electrospinning (SES and MES, respectively), formation, and materialization of a jet at the tip of the nozzle due to the EHD phenomenon termed as Taylor cone, named after Sir Geoffrey Taylor [121]. The main difference between MEW, SES, and MES is the stability of the formed jet during the travel distance from the nozzle to the collection surface. In MEW, the balance between the mass flux of the polymer jet and the mass flux of deposited polymer fiber is maintained through several opposing factors, including the surface tension of the polymer, viscosity, electrical field strength, and collector movement speed. By maintaining the balance between these factors, controlled and directed deposition of the polymer fibers could be achieved, mainly referred to as writing. Moreover, the deposited fiber cools down during its travel from the nozzle to the collector surface, resulting in a solid polymer fiber placement. In addition to the formation and guiding of the jet, the EHD phenomenon results in complex convection in the vicinity of the traveling jet, which is reflected as EHD quenching assisted by the transport of charged ions through the travel path [122].

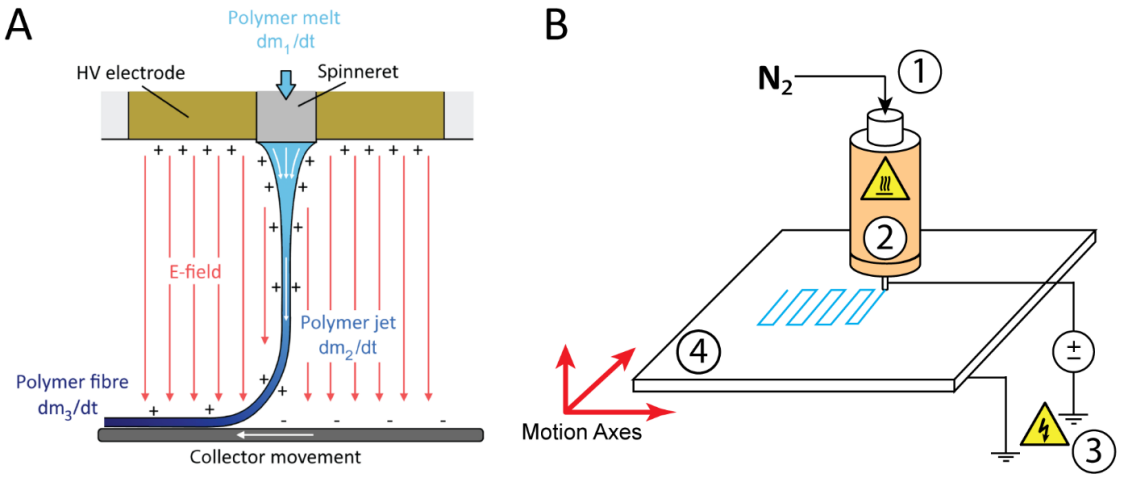

Figure 4. Schematic of MEW process. **A**) The acting forces on molten polymer resulted in the formation of a thin fiber jet that can be deposited on the collector in a controlled manner. The balance between mass flow caused by electrohydrodynamic forces determines the accuracy of the deposition. Reprinted from reference [123] as an open-access article distributed under the terms of the Creative Commons Attribution 3.0 license (CC BY-NC-ND 3.0). **B**) Demonstration of a typical MEW platform to produce micron-sized fibers. Different elements of the platform include 1) a pneumatic source for the continuous supply of molten polymer at the nozzle, 2) a hot reservoir to melt and store the polymer, 3) a high-voltage source to apply the required electrical field between the nozzle and the collector, and 4) a multiple-axis motorized and computer-controlled collector plate. Modified and reprinted from reference [124] as an open-access article distributed under the terms of the Creative Commons Attribution 4.0 license (CC BY-NC 4.0).

The geometrical accuracy and deposition resolution of MEW critically depends on the balance between the mass fluxes of polymer jet and polymer fiber. This balance is mainly controlled by adjusting the collector's movement speed, and in principle, a critical translation speed (CTS) is considered the threshold for the deposition of straight fibers. At traveling speeds below CTS, deposition of straight fibers is impossible since the mass flux of the polymer jet is greater than that of the polymer fiber. By increasing the traveling speed to values greater than CTS, fiber pulling might occur, contributing to stretching the deposited fiber and, subsequently, reducing the fiber diameter [125].

1.3.2 MEW challenges and opportunities

The multi-parameter nature of MEW results in two main features of the process, one is the flexibility and versatility of this technique in creating structures with a considerable level of detail in terms of geometrical features, and the other is the challenges in controlling and optimization of process parameters to achieve stability and reproducibility. A significant source of geometrical errors and artifacts in the MEW process stems from the "pulsing" phenomenon, which is defined as the undesired oscillation of fiber diameter caused by disequilibrium of mass flow between the polymer jet and the polymer fiber [123] (**Figure 5**). Fiber pulsing is especially important when a sudden change in the direction and the velocity of printing is planned, which might result

in the misplacement of fibers and, subsequently, the accumulation of geometrical errors in multi-layer objects [123]. To overcome fiber pulsing, the balance in the mass flow should be preserved by adjusting different process parameters, including the potential difference, collector distance, printing temperature, collector speed, and the inlet pressure (or, in general terms, the nozzle's mass influx). Flow instabilities could generally deteriorate the outcome of MEW by introducing geometrical artifacts, potentially influencing the delicately-structured scaffolds' structural and mechanical properties [123].

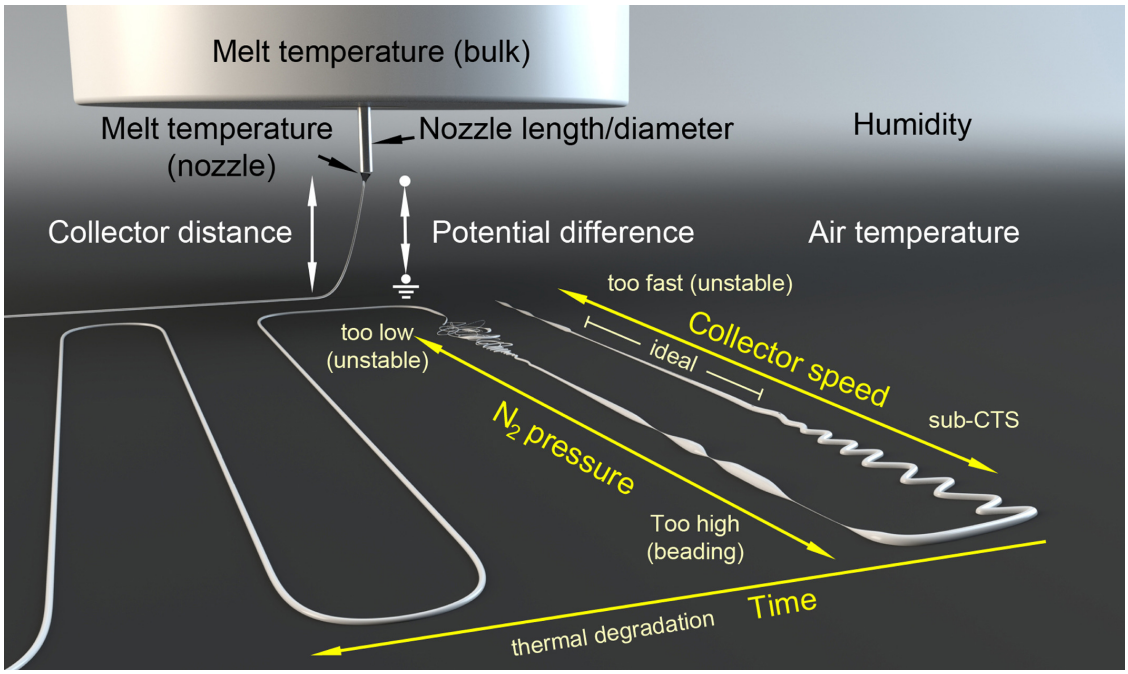

Figure 5. Schematic of the MEW jet and fibers, with some essential parameters affecting fiber diameter/quality-labeled. Reproduced from reference [126] with permission from John Wiley & Sons Ltd.

The same critical process parameters in MEW could potentially expand the reach of this technique by enabling precise control over the geometrical features of the deposited fibers [124, 125, 127, 128]. Changing process parameters during printing alters deposition characteristics, mainly regarding the geometrical pattern [124, 128-130] and the fiber diameter [124, 125]. **Figure 6** shows examples of different scaffold architectures and dimensions produced by variations of several process parameters. In addition to conventional box-structured scaffolds, different laydown patterns, including triangular, dodecagonal, sinusoidal, interpenetrating mesh networks, and tubular structures, can be produced. Moreover, fiber diameters in a wide range, from hundreds of nanometers to tens of micrometers, could be realized [127].

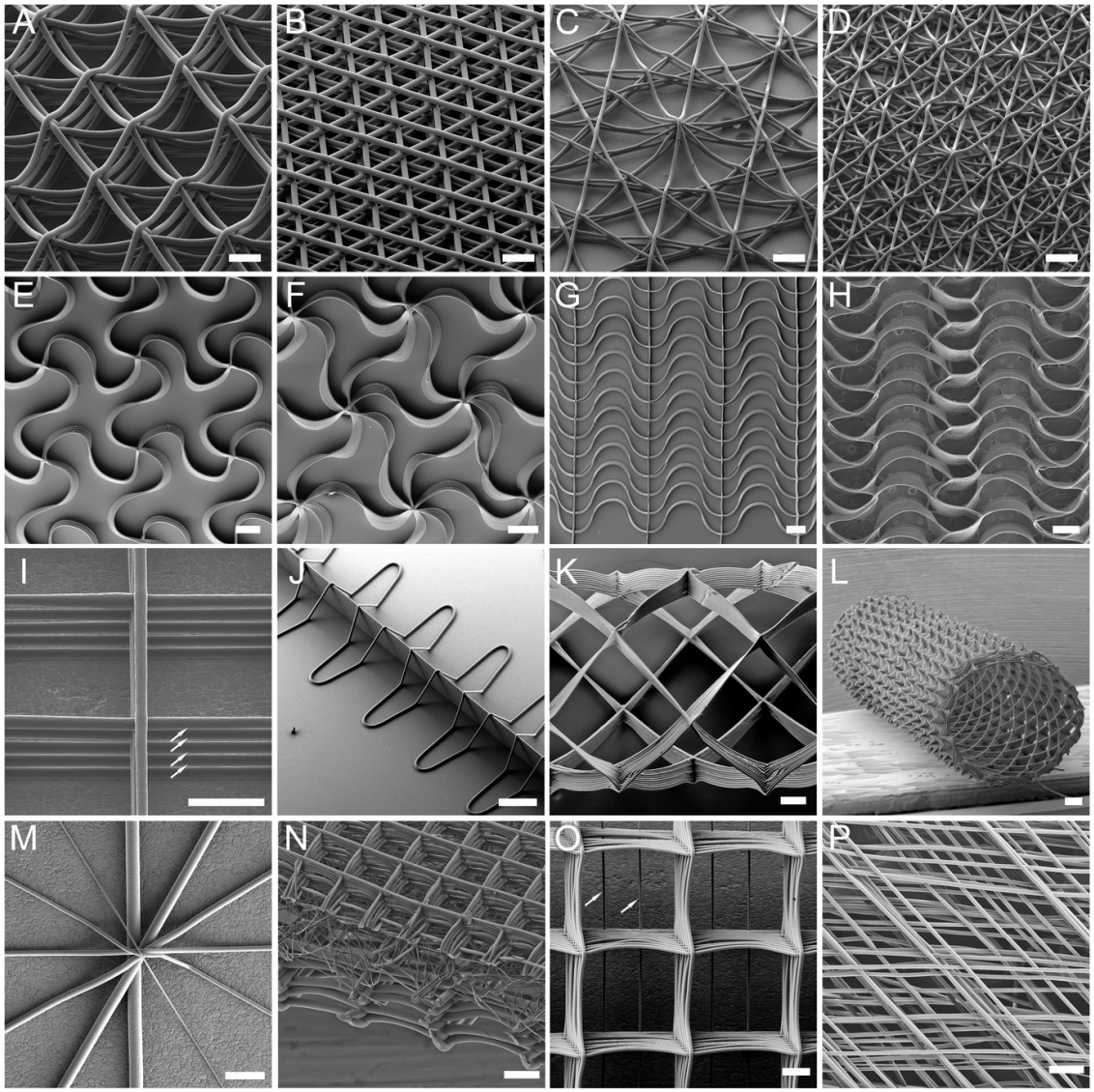

Figure 6. Scanning electron microscope (SEM) images of various melt electrowritten PCL scaffold designs. Different laydown patterns beginning with triangular/hexagon designs with **A**) 20 µm fibers at 250 µm spacing or **B**) 10 µm at 125 µm spacing, dodecagon designs with **C**) 10 µm fibers at 250 µm spacing or **D**) 20 µm at 125 µm spacing. Sinusoidal architectures with **E**) box and **F**) hexagonal designs while **G**) shows unidirectional and **H**) bidirectional structural design. **I**) Image of non-sagging fibers with small spaces between pores (white arrows), **J**) out-of-plane fibers, a highly ordered 3 mm diameter tubular scaffold with **K**) eight and **L**) 30 pivot points. **M**) An image of different diameter fibers crossing over at a single point. **N**) Shows a multiphasic scaffold design of three different porosity scaffolds. **O**) Shows a standard lattice scaffold with spheroid supporting fibers. **P**) A lattice scaffold design with each y-direction staggered by 50 µm forming larger channels through the depth of the scaffold. Scale bars = 100 µm **A**–**D**), 500 µm **E**–**H**), 50 µm **I**), 200 µm **J**–**L**), and 100 µm **M**–**P**). **A**–**D**) Reproduced from reference [127] as an open-access article distributed under the Creative Commons Attribution 4.0 license (CC BY-NC-ND 4.0).

On-demand manipulation of internal architecture and feature sizes of scaffolds is considered one of MEW's main offerings [127]. Using MEW, it is possible to design and fabricate micron-scale scaffolds applicable to the TE domain, considering each application area's case-specific requirements. Considering this design freedom, transitioning from traditional manufacturing technologies to a hybrid multi-technology

biofabrication approach employing MEW seems feasible [131]. In this way, the advantages of MEW in terms of precise geometrical control in micron-scale deposition can be combined with a variety of novel and traditional (bio)fabrication methods, which could compensate for some limitations in MEW, including the functionality, bioactivity, and production speed [131].

1.3.3 Sacrificial templating by MEW

Despite the increasing research on MEW, using this manufacturing process to fabricate sacrificial structures is still in its infancy. The embedded MEW sacrificial structures were mainly purposed to create hollow microchannels with a focus on their application in the field of microfluidics. The embedding matrices included polydimethylsiloxane (PDMS) [132] and fused silica glass [118]. To expand this approach to soft, more biologically relevant matrices, Haigh et al. successfully incorporated PCL sacrificial templates via MEW into photo-crosslinked poly(2-oxazoline) hydrogels later removed by selective dissolution of PCL fibers [133].

The few available studies in the literature showed great promise in using MEW to fabricate microchannels by sacrificial templating. An advantage of MEW over the other methods of sacrificial templating is the uniformity of the well-controlled fiber diameter across the geometry and the tunable process to produce fibers with different diameters depending on the intended design. These factors indicate the benefits of further investigation for expanding the applicability of MEW as a sacrificial templating method.

A sacrificial template produced by MEW can be embedded in a hydrogel matrix by either casting hydrogel precursors or controlled deposition of the hydrogel using a 3D bioprinting process. In this way, the hybrid manufacturing process depends on two sets of primary criteria; one controls the templating structure's geometrical features, and the other controls the deposition and formation of the surrounding matrix. This breaking down of the hybrid process enables individual control over the details of each step and tailoring the outcome based on the application requirements.

The tunability and control of the dimensions of MEW-generated structures have been briefly discussed and highlighted in the previous sections. The following section will discuss tuning and controlling the outcome of the 3D bioprinting process as a potentially complementary sequence in the multi-technology manufacturing of templated structures.

1.4 Extrusion bioprinting in multi-technology manufacturing

Between the commonly used biofabrication technologies (**Figure 2**), inkjet-based and extrusion-based bioprinting methods have the most potential to be used in a sacrificial-

templating biofabrication approach, either as a stand-alone or a complementary manufacturing step. The two methods significantly differ based on their working principles, and extrusion-based techniques became more widespread due to their simplicity.

Two main categories of parameters govern and control the success of 3D extrusion bioprinting, the process-related aspects and the material-related requirements. The process-related aspects include software and computer-aided modeling steps, and the material-related requirements are mainly related to the structure-property-processing relationship of the bioinks within the context of extrusion bioprinting [134].

The material-related requirements of 3D extrusion bioprinting determine the controlled deposition of bioinks and, in general terms, their printability. Printability of bioinks refers to the capacity to form and maintain the designed geometrical aspects of the structure and maintain them throughout and after bioprinting [135]. Multiple factors associated with bioink properties, printing process parameters, and the structure's final design affect printability. This resulted in significant complexities in controlling and directing the bioprinting process, as each bioink demands specific flow requirements to be printable in a known set of conditions, which stem from the bioink's physical and chemical properties.

Flow characteristics are the key to anticipating the compatibility of bioinks with extrusion-based biofabrication techniques [134, 135]. The flow behavior is primarily influenced by the chemical and physical properties of the bioinks. Ideally, a bioink should flow easily upon application of force through a fine nozzle, and it must retain its shape after extrusion, characterized as a non-flowing gel. However, most natural and synthetic hydrogels lack the requirements for printability. This led to the development of composite bioinks or formulations, which can be tuned according to the design requirements.

The rheological properties of bioinks play a significant role in the outcome of 3D extrusion bioprinting [136]. The rheology of hydrogel or polymer solutions involves multiple aspects of steady-state and time-dependent viscoelasticity. The resistance to flow, the resistance to time-dependent deformation, and the extent and stability of intramolecular and microstructural interactions are determined by rheological characterization. Each of these properties dictates a specific deformation pattern during the 3D extrusion-based bioprinting, and deep knowledge and understanding of their role and extent will critically influence the engineering of new bioinks and formulations.

Most natural polymers do not meet the requirement for 3D extrusion-based bioprinting [137]. This incompatibility resulted in extensive efforts to develop modified natural polymers or synthetic substitutes that approximate natural polymers' biological capacities. However, difficulties in recapitulating the rich biochemistry of natural polymers have hindered the further expansion of the biofabrication window [138, 139].

A facile and relatively growing approach for adapting natural polymers with bioprinting requirements includes using rheology modifiers. Rheology modifiers are common additives that alter the viscosity and viscoelasticity of the base polymer solution by altering the flow behavior or formation of secondary intra- and intermolecular interactions [136, 139]. Despite their widespread use for different bioink platforms, a general understanding of the mechanism and processes involved in creating a printable formulation using rheology additives is still missing, mainly correlated with the diversity of formulation systems.

1.4.1 Tailoring bioinks to meet bioprinting requirements

Bioink properties before, during, and after extrusion critically determine the outcome of extrusion-based bioprinting. In addition to the cytocompatibility criteria, bioinks must meet the mechanical and chemical stability requirements before extrusion to enable homogeneous and continuous delivery of viable encapsulated cells. Reactive unsaturated chemical functionalities could impose reactive oxygen species-dependent stress, influencing encapsulated cells' viability and function [140]. Moreover, the stability window for time-dependent crosslinking reactions before extrusion should be carefully designed to maximize the viability of encapsulated cells. Mechanical stability of bioinks before printing influences the distribution of suspended cells since sedimentation and aggregation of encapsulated cells would result in the inhomogeneous distribution of cells and, consequently, alteration of flow and mechanical characteristics of the bioink.

During extrusion, bioinks face severe mechanical forces. In response to such conditions, bioinks must show a shear-thinning behavior, which will aid in their flow by transitioning from solid-like behavior when facing low mechanical forces to fluid-like flow when experiencing high mechanical forces. Moreover, shear thinning behavior would protect encapsulated cells from prolonged exposure to high shear forces.

The properties of bioinks after extrusion are the most critical aspects in determining printability. Extrudability and formation of continuous flow are the first significant factors in determining the printability of a bioink [141]. Lack of filament formation results in disruption of the flow and formation of artifacts and loss of geometrical deposition precision.

After extrusion, bioinks transition back from a fluid-like to a solid-like state. At this stage, the index to retain shape is critically dependent on the capacity of bioinks to reform and reestablish their internal molecular and structural interactions or by using a post-curing secondary stabilization step through a physical or chemical crosslinking method. This would be done by introducing covalent or non-covalent bonds into the bioink matrix, either a naturally occurring feature of the bioink or an externally induced modality through chemical or physical modifications [137, 139, 142].

Tailoring the bioink properties to meet the requirements of extrusion bioprinting essentially involves modification of bioink behavior before, during, and after extrusion. Sophisticated chemical modification offered by often complicated methods can alter and tune the flow properties of bioinks based on the intended applications and their requirements [139]. However, the required experience and specialty for such chemical modifications limit the widespread use of these bioink libraries.

In contrast to complex chemical modifications, blending and using rheology additives proved accessible for developing and expanding printable bioink libraries [143]. Being cost-effective and facile, the number of research studies based on different additives has increased significantly [143]. Blending and using additives augment one material's biological and mechanical properties with another. This expands the processing window of previously not-printable bioinks, providing the advantages of the rich biochemistries of the natural polymers as the main components of a newly designed bioink. Additives and blends are used to either improve the extrudability of low-viscosity bioinks or to establish secondary intra- and intermolecular interactions, through which geometrical stabilization of the extruded bioinks would be achieved [136]. Bioinks with biological, chemical, and physical properties tailored based on the requirements of the hybrid biofabrication approaches potentially enhance and improve the success of a hybrid manufacturing process.

1.5 Aims and the scope of the thesis

Creating vascularized structures requires characterization and optimization of several factors, including those related to process parameters, selection of bioinks, and considerations about the processing-structure-properties-performance (PSPP) relationships. This is an inherently complex process, as each biofabrication technology has its requirements, and also, mutual dependencies regarding the processing limits in a multi-technology approach can be anticipated. This thesis investigated the optimization and engineering of the outcome of two main biofabrication technologies, MEW, and extrusion bioprinting, for fabricating vascularized structures. The scope of

this thesis involved investigating each of the mentioned biofabrication methodologies as a stand-alone technology.

In the first part of this thesis, MEW, as a novel method for templating microchannels, was investigated. In this respect, extensive characterization and optimization of the MEW process to control and predict the fabrication outcome was performed.

Chapter 2 presents the MEW of a carbohydrate glass as a tool for templating high-resolution microchannels. The results of this chapter show that the application of MEW as a templating fabrication method can address some limitations of current methods of sacrificial templating concerning the control over the process, adjustability, and, more importantly, the geometrical aspects and dimensions of the created microchannels.

A novel strategy for fabricating microvascular structures within bulk hydrogel structures is presented in **Chapter 3**. The presented methodology is based on the MEW of a thermoplastic polymer, which shows a temperature-dependent dissolution behavior. Moreover, an extensive optimization and analysis of the process of fabricating hollow microchannels are presented.

The second part of this thesis involves characterization and advanced analysis of the PSPP relationship in extrusion bioprinting. For this purpose, bioinks based on rheology modifiers were the main subjects of the studies, and the main objective was to shed light on some fundamental aspects of bioink development.

A model system based on a commonly used natural hydrogel bioink and a low molecular weight gelator peptide was briefly introduced in **Chapter 4**. This model system was meant to be a simple demonstration of how adjusting a few inherent design parameters of the bioink can lead to drastic changes in the final properties of the formulation.

To explore this further, an extensive and in-depth study on the PSPP relationship in formulations based on rheology modifiers is presented in **Chapter 5**. Using state-of-the-art and complex analytical methods, it was shown that a generalized understanding of the concept of printability could be achieved, and insights on the process of rendering printability in formulations based on rheology modifiers are presented.

A concluding discussion about the findings of this thesis is provided in **Chapter 6**, and the potential future research directions are highlighted.

Chapter 2

Melt Electrowriting of Isomalt for high-resolution templating of embedded microchannels

Chapter 2 was published as an original research article (Nadernezhad, A., Ryma, M., Genç, H., Cicha, I., Jüngst, T. and Groll, J., 2021. Melt electrowriting of isomalt for high-resolution templating of embedded microchannels. *Advanced Materials Technologies*, *6*(8), p.2100221), reproduced from reference [124], which is an open-access article under the terms of the Creative Commons Attribution-NonCommercial License 4.0.

This article is based on the work of the author of this thesis Ali Nadernezhad, who performed all the experiments, data evaluation, and drafting of the manuscript.

2.1 Abstract

Fabrication of microchannels using 3-Dimensional (3D) printing of sugars as fugitive material has been explored in different fields, including microfluidics. However, establishing reproducible methods for the controlled production of sugar structures with sub-100-micron dimensions remains a challenge. This study pioneers the processing of sugars by Melt Electrowriting (MEW) to enable the fabrication of structures with so far unprecedented resolution from Isomalt. Based on a systematic variation of process parameters, fibers with diameters down to 20 micrometers could be fabricated. The flexibility in the adjustment of fiber diameters by on-demand alteration of MEW parameters enabled generating constructs with perfusable channels within Polydimethylsiloxane (PDMS) molds. These channels had a diameter that could be adjusted from 30 to 200 microns in a single design. Taken together, our experiments show that MEW strongly benefits from the thermal and physical stability of Isomalt, providing a robust platform for the fabrication of small-diameter embedded microchannel systems.

2.2 Introduction

The impressive development of additive manufacturing (AM) is not only based on the freedom in design and the field's progress from prototyping toward manufacturing technologies but also on the increased accessibility of low-budget printers [144]. Based on availability, 3D printing activities have increased in a broad range of research areas. Particularly, this led to the acceleration of the development of novel materials for AM, and sugar-based glasses demonstrated their potential in extrusion-based 3D printing, mainly as support material or fugitive inks [115, 145, 146].

Especially in tissue engineering, rapid water solubility and ease of removal after printing rendered sugars into valuable fugitive materials for 3D printing as they help to tackle one of the main challenges in the field: perfusion and nutrient support of cell-laden tissue-engineered constructs quickly after fabrication. Miller et al. demonstrated this potential by fabricating delicate microchannels from a mixture of glucose, sucrose, and dextran solutions as glass ink within cell-laden bulk hydrogels using an extrusion-based approach [115]. The dimension of fabricated microchannels ranged from 150 to 750 microns. Since then, several other studies have attempted to systematically control and enhance the process of 3D printing of sugars [145, 147-149].

Nevertheless, tissue engineering was not the only research field that benefited from AM of fugitive materials. Since the early 2000s, microchannels created with 3D printing of fugitive inks have gained increasing attention as an alternative to the traditional soft lithography techniques within the field of microfluidics. These systems address a long-lasting limitation of soft lithography in expanding the microchannel networks from 2D to 3D. The pioneering work by Therriault et al. [150] demonstrated the possibilities of expanding AM towards microfluidics, including 3D microchannel networks. Although 3D printing principles promote exciting and new opportunities for microfluidics, soft lithography approaches still hold the advantage over conventional 3D printing technologies such as extrusion printing or stereolithography, when it comes to reaching small feature sizes and high surface qualities [151, 152]. While extrusion-based techniques mostly delivered millifluidic size scales, stereolithography could push the boundaries below 100 µm. However, the commercially available resins and printers to achieve such resolutions are very limited [151]. As an alternative to conventional 3D printing technologies, methods such as liquid-filled voids for PolyJet printing [153] and Two-Photon direct laser writing polymerization [154] allow the fabrication of feature sizes below 50 µm. However, these approaches are limited due to several technology-inherent challenges, including the very slow nature of the processes and small build volumes.

These limitations could be overcome by emerging 3D printing technologies, such as Melt Electrowriting (MEW). MEW provides the opportunity to fabricate delicate microstructures with excellent reproducibility and precision [155]. It is an AM process based on the application and manipulation of electrohydrodynamic forces to guide and deposit micron-sized fibers ranging between 0.82 µm [89] to 180 µm [156] in well-defined patterns. A computer-controlled movement of the collector delivers direct control over the deposited pattern. A significant aspect of MEW relevant for the applications involving embedded microchannels relies on the possibility of adjusting process parameters on-the-fly. This makes MEW a one-step fabrication process to realize on-demand feature sizes with great variety. Hrynevich et al. showed that by changing a single MEW factor in a controlled way, the fiber diameter in a simple mesh structure could be altered by one order of magnitude [125]. Despite these benefits, MEW is a demanding process concerning the choice of compatible materials. In addition to the high sensitivity of the direct writing process on material changes, the high resolution realized by the small fiber diameters implies extended fabrication times. In particular, the need for materials with low thermal degradation has limited the availability of materials and rendered poly(ε-caprolactone) the gold-standard material for MEW [157]. Despite that limitations, MEW has already proved its feasibility to generate micron-sized perfusable channels for microfluidic applications based on the fugitive approach [118, 158]. A limitation yet to be addressed for these approaches is the harsh conditions during the removal of the poly(ε-caprolactone) fibers from the microfluidic devices. Taken together, MEW would benefit from thermally stable, water-soluble materials to advance in the area of microfluidics as those used for conventional extrusion 3D printing.

Although sugar-based inks demonstrated their potential for extrusion 3D printing and might be potential candidates that help overcome the MEW limitations, some technical aspects should be noted. Incorporating water in formulations of sugar glass mixtures can significantly impact the crystallization, viscosity, and degradation kinetics of the sugar glass inks [145]. Moreover, the high temperature of the 3D printing process can result in the caramelization of the sugars, especially during the extended holding time of the sugar glasses at high temperatures during extrusion, which can alter the degree of polymerization [159]. This would consequently alter the ink's rheological and mechanical properties during and after the extrusion, resulting in difficulties in reproducibility and control of the fabrication process, especially if a process sensitive to small changes in material properties such as MEW is considered. A potential sugar candidate to overcome these limitations is Isomalt. Isomalt is a sugar alcohol derived from the sucrose in a two-step process and is an approximately equimolar mixture of α-D-glucopyranosyl–1-6-mannitol (GPM) and α-D-glucopyranosyl–1-6-sorbitol (GPS).

Crystalline Isomalt melts around 142–150°C, which yields a glassy state after cooling with a glass transition around 60°C [160]. The melting temperature of Isomalt is significantly lower than that of the two isomers, which is attributed to the formation of a simple eutectic between two sugar alcohols [161]. An interesting property of Isomalt is that, unlike other sugar alcohols, Isomalt does not degrade upon melting [161]. This behavior could play a significant role in considering Isomalt for processing methods that involve heating at elevated temperatures during processing, such as MEW. Moreover, Isomalt is a readily available material at low cost, with minimal variations in properties due to regulatory requirements for a sugar substitute in the food industry.

Based on these considerations, we hypothesize that Isomalt is a potential candidate material that enables the fabrication of fugitive fibers within a wide range of dimensions in a reproducible way via MEW. To prove this hypothesis, we show that by systematic variation, precise adjustment, and control of the process parameters, water-soluble Isomalt fibers in the range from 20 to 200 µm diameter can be generated with MEW for the first time. In addition to an analysis of process-related thermal properties of Isomalt and presenting an operational window based on fiber diameter *vs.* MEW process parameters, a preliminary proof-of-concept study demonstrates the flexibility of MEW in combination with Isomalt for the production of perfusable channels potentially relevant for microfluidic applications. The channels generated within PDMS after a water-based dissolution step of the fibers had adjustable shapes and varying diameters.

2.3 Materials and methods

2.3.1 Materials

Isomalt (E953) was supplied by a local vendor (TeKa Food GmbH, Germany) and used without further purification. The Silicon elastomer kit (Sylgard 184) was purchased from Dow Corning. The aqueous dispersion of 10-micron polystyrene (PS) microbeads was purchased from Sigma-Aldrich.

2.3.2 Thermal analysis

Netzsch DSC204 F1 Phoenix differential scanning calorimetry (DSC) was used to characterize the thermal properties of Isomalt. The heating/cooling rate was set to 10°K/min. Thermal gravimetric analysis of Isomalt was performed using Netzsch TG 209 F1 Iris within the temperature range of 30-900°C with a heating rate of 10°K/min.

2.3.3 Rheology

Viscoelastic properties of Isomalt at high temperatures were characterized through sequential frequency sweeps during 1°C stepwise cooling from 130°C to 65°C. For this purpose, Anton Paar MCR702 rheometer equipped with 25 mm parallel plate geometry was used. Frequency sweeps between 1-100 rad/s were performed at each temperature interval while the applied strain was kept constant at 0.1%.

2.3.4 Imaging

Optical imaging of the melt electrowritten Isomalt fibers was performed using a Discovery V20 stereomicroscope (Carl Zeiss Microscopy GmbH, Germany). Perfusion of microparticles through the embedded channels was photographed with Zeiss Axio Vert. A1 (Carl Zeiss Microscopy GmbH, Germany) inverted microscope equipped with a high-speed camera (Phantom High Speed, Vision Research, USA).

2.3.5 Melt electrowriting

The MEW device (**Scheme 1**) was enclosed in a closed chamber connected to an environmental controller for temperature and humidity (ACS Discovery, ATT Umweltsimulation GmbH, Germany). The chamber's relative humidity and temperature were set to 18 ± 1% and 39 ± 1°C, respectively. The MEW device included a heated reservoir mounted on a computer-controlled 3-axis platform. Pressurized nitrogen gas was connected to the melt reservoir through an automated valve. The high-temperature reservoir included two separate sections for heating the syringe-based cartridge and the

nozzle with dedicated controllers. The nozzle and the build plate were connected to a computer-controlled high-voltage source (HCP 14-20000, FuG Elektronik GmbH, Germany). A central control unit (Bosch Rexroth AG, Germany) was used to drive the 3-axis platform and trigger the corresponding signals for temperature, applied pressure, and applied electrical field controllers as integrated functions during the execution of the G-code path planning. For MEW of carbohydrate glass, glass syringes filled with the granules were placed in the heating unit preheated at 170°C to remove the thermal history by complete melting. After 30 min, the heating unit's temperature was gradually decreased to the set process temperature and was kept for 30 min before printing to ensure a thermal equilibrium was reached. The Isomalt fibers were printed on 1.1 mm thick glass slides (VWR, Germany), and placed on the stainless-steel collector.

2.3.6 MEW process parameters

The selected MEW process parameters were systematically changed between five equidistant levels according to **Table 1**. Only one parameter was changed at a time, and the other variables were set as the center values of corresponding ranges. The critical translation speed (CTS) was first identified for each set of parameters. To ensure the deposition of straight fibers and minimize the change in fiber diameter due to stretching of the fibers, the collector velocity for each series of experiments was set to 10% higher than the corresponding CTS value for the respective combination of process parameters. The measured fiber diameters (n=300) from microscopy images were evaluated with a one-way analysis of variance (ANOVA), and the differences with p-values lower than 0.05 ($p<0.05$) were considered statistically significant.

Table 1. MEW parameters and the corresponding values

Parameter	Parameter range/step size	Center value
Applied pressure (bar)	1.0-3.0 / 0.5	2.0
Applied voltage (kV)	4.0-6.0 / 0.5	5.0
Tip-to-collector distance (mm)	1.5-3.5 / 0.5	2.5

2.3.7 Numerical modeling

The impact of different substrates on the MEW process was modeled numerically in COMSOL multi-physics using the AC/DC module (COMSOL Inc., USA). The electric field distribution in a stationary DC field was done by solving the Maxwell equation with the boundary conditions based on the experimental parameters. The values of the electrical conductivity and permittivity of glass and PDMS were obtained from the COMSOL library and literature [162]. The influence of the substrate on electrical field distribution with different applied electrical potentials (4.0-6.0 kV with 500 V increments) was evaluated.

2.3.8 Fabrication of templated microchannels

Silicon elastomer resin was used to fabricate Polydimethylsiloxane (PDMS) slabs with a thickness of 1 mm. The resin was cast in an aluminum mold and cured at 150°C for 9 min. The cured slabs were used as substrates during MEW. The Isomalt fibers were directly deposited onto the PDMS surface. During printing, process parameters were extensively altered to precisely control the diameter of deposited fibers based on the design. After printing, the PDMS substrate and the deposited fibers were gently moved to an aluminum mold, and freshly prepared silicon elastomer resin was slowly poured over the printed fibers. The embedded fibers were left at room temperature for 48h to cure the resin completely. The inlet and outlet points of the resultant structure were generated using a 0.9 mm biopsy punch. The embedded fibers were soaked in Milli-Q water and kept at 60°C for 24h for the complete dissolution of Isomalt fibers. The PDMS slab with embedded channels was attached to a plasma-activated microscopy glass slide. The fabricated channels' patency was assessed by perfusion of 0.1 wt.% dispersion of 10 µm PS microbeads in 35% PEG 400 solution in Milli-Q water.

2.4 Results and discussion

MEW involves stretching and drawing a very thin fiber driven by the balance between mechanical, gravitational, and electrical forces opposing the viscosity and surface tension of molten material at the nozzle tip [163]. Due to the extremely hygroscopic nature of Isomalt, the stability and continuity of the formed jet and, more importantly, the fidelity of deposited Isomalt microfibers would significantly be influenced by environmental conditions. Our preliminary experiments (data not shown) confirmed that at normal laboratory environmental conditions, the extreme hygroscopic nature of Isomalt results in condensation and local dissolution of micron-sized Isomalt fibers caused by environmental humidity and consequently loss of shape and integrity. This effect was more pronounced when the fiber dimensions reached below 100 microns. To enable systematic control over experimental and environmental conditions, all the experiments were conducted in an environmentally monitored chamber (**Scheme 1** and **Figure 7**).

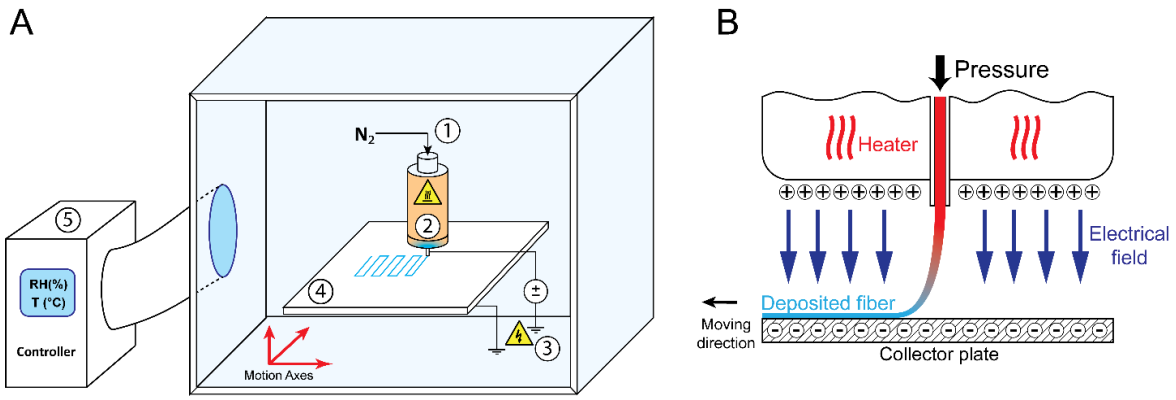

Scheme 1. A) Schematics of the MEW device including (1) Inlet pressurized nitrogen gas (2) Resistive heating element containing two separate elements for the cartridge and nozzle sections (3) High voltage source (4) Collector plate capable of moving in 3 directions (5) Environmental chamber controller to set the relative humidity (RH) and temperature of the chamber. **B**) Drawing to show the configuration of the nozzle and the formed jet due to pulling force of electrical field during fiber deposition.

By stabilizing the environmental conditions, the reproducibility of the MEW process was ensured, and at the same time, the influence of day-to-day variations of environmental temperature and humidity on the process was minimized.

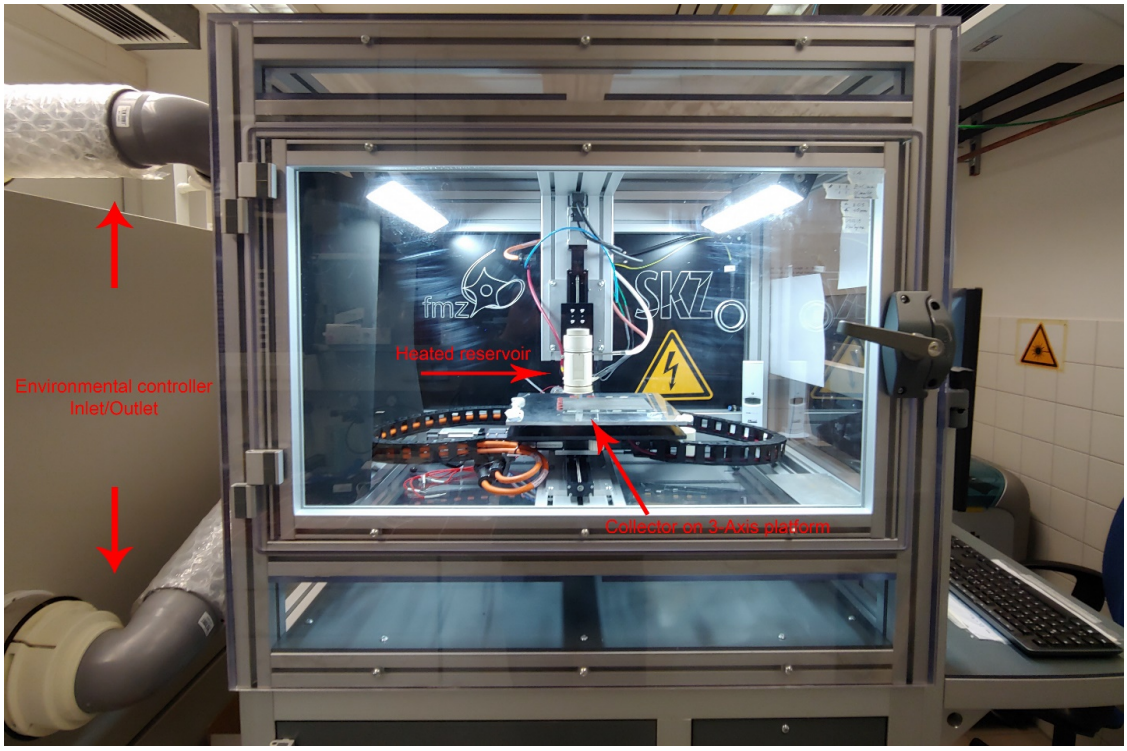

Figure 7. A photograph of the actual MEW setup used in this study for fabricating embedded microchannels from sacrificial Isomalt microfibers.

2.4.1 Characterization of the Isomalt glass

As the thermal properties of any candidate material for MEW play a significant role in the feasibility of the process, thermally stable materials with sufficiently high viscosity are a reasonable choice. **Figure 8**A and B show the DSC and TG thermograms of Isomalt. Within the early stage of heating up to 250°C, only 4.5% of mass loss was observed, which can be attributed to dehydration (**Figure 8**A). The onset of thermal degradation followed by a massive mass loss was found to be at 250.4°C. Overall, Isomalt showed excellent thermal stability at temperatures below 250°C, which contrasts with the other sugar candidate materials such as sucrose, fructose, and glucose. Although these sugars are water-soluble and stiff, sucrose-, glucose- and fructose-based glasses tend to easily oxidize with increasing temperature [164].

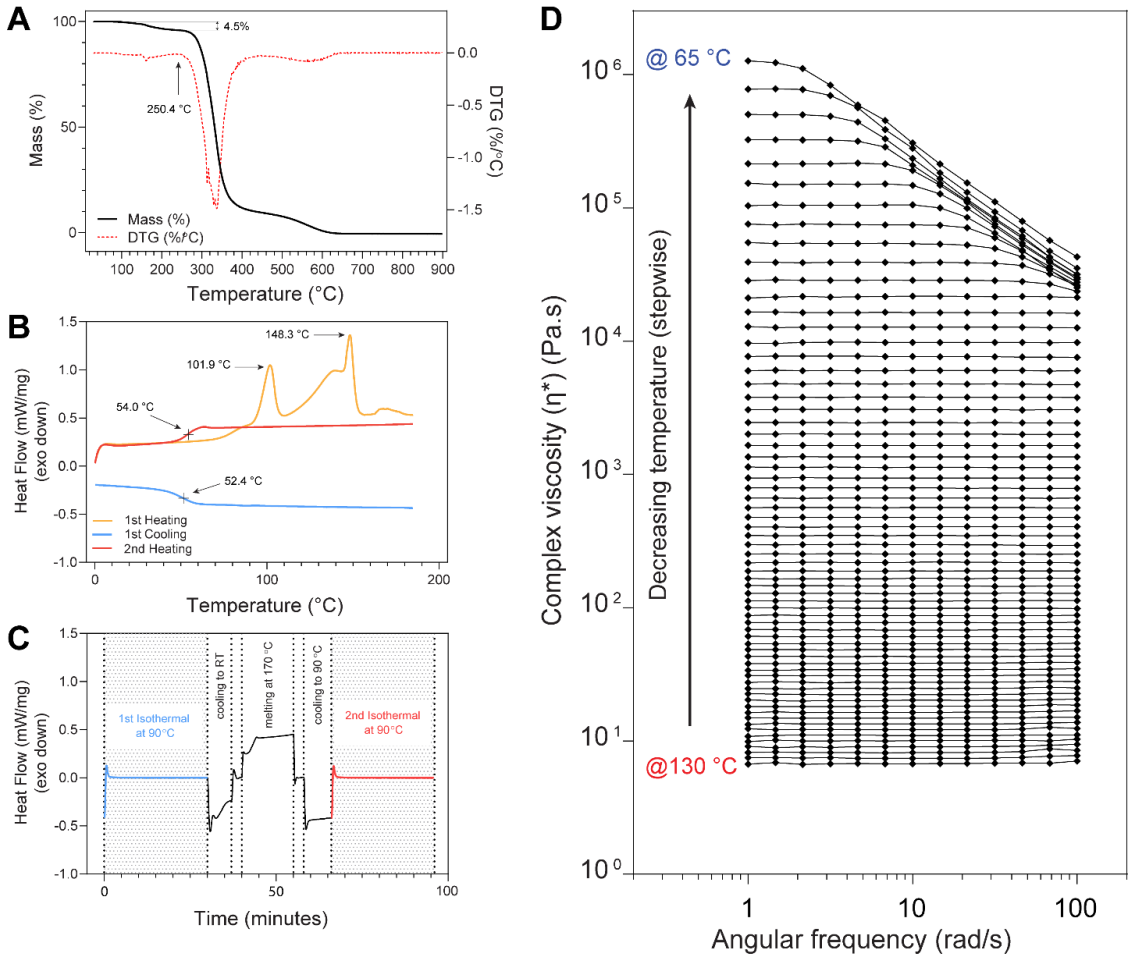

Figure 8. Thermal and rheological analysis of Isomalt to investigate compatibility with the MEW process. A) TG profile during heating from 20 to 900°C. **B**) DSC profile of first and second heating-cooling cycles showing the glassy state of Isomalt at high temperature. **C**) DSC profile of Isomalt during cyclic heating-cooling of glass after removing the thermal history. The applied thermal regime mimics the thermal protocol used in MEW. **D**) Rheological characterization of Isomalt shows a significant increase in complex viscosity over the experimental frequency range by decreasing the temperature of the glass from 130 to 65°C in a 1°C per step manner.

The phase transition during the heating and cooling of Isomalt was characterized by DSC, and the results are shown in **Figure 8**B. Isomalt is a hygroscopic sugar alcohol that undergoes crystallization upon hydration during storage. The first heating cycle in DSC showed two peaks, one related to dehydration with the peak at 101.9°C, and the second peak was due to the melting of the crystal domains. However, the first cooling cycle did not show any crystallization upon cooling, and only a glassy phase until reaching the glass transition was observed. On the other hand, the second heating cycle showed only a glass transition at T_g = 54.0°C, and further heating did not induce any phase transitions. Sugars can slowly undergo crystallization by being kept above their glass transition for a long time. Moreover, shear is known to accelerate the crystallization of sugars in a glassy state [164]. This can cause clogging of the nozzle during the extrusion of glass from a fine nozzle. Unlike the other heat-resistive sugars such as lactitol and maltitol, Isomalt is not prone to crystallization even when kept at high

temperatures for extended time periods like those expected during fabrication since the crystallization kinetics of Isomalt depends on the hydration degree. Crystallization of Isomalt occurs by the formation of dihydrates, which can be decelerated or almost prevented through dehydration [160]. Considering the mechanism and kinetics of crystallization in Isomalt, a single melting step followed by cooling above the glass transition temperature will result in the formation of a stable glassy state as long as the environmental humidity is monitored and controlled. The thermal stability and consistency in structural properties of Isomalt is a determining factors for the application of this material in processes such as MEW, which rely on continuous deposition of fibers from a material reservoir kept at elevated temperatures. Since the dynamics of processes such as MEW heavily rely on the establishment of a balance between several opposing factors, consistency and stability in the physical properties of the material are of great importance [127]. The phenomena such as degradation, polymerization, and crystallization could significantly alter the physical properties of molten or glassy sugars. A cyclic DSC study revealed that after the removal of thermal history, Isomalt glass shows a consistent thermal profile during a cyclic heating-cooling regime (**Figure 8**C). This would further confirm that by following a predefined protocol of removing the thermal history, the physical properties of Isomalt would remain unchanged during MEW processing. In this way, Isomalt offers a stable glassy state at high temperatures in controlled environmental conditions, hence contributing to the stability of the delicate balance governing successful jet formation in MEW.

We hypothesized that by maintaining a glassy state, Isomalt at high temperatures could be extruded or dispensed through a fine nozzle as long as the glass's viscoelastic properties allow the formation of a continuous jet. Rheological characterizations showed that the complex viscosity of Isomalt glass increased by about five orders of magnitude by decreasing temperature from 130 to 65°C (**Figure 8**D). At high temperatures, Isomalt glass could be easily deformed, and the low viscosity would result in the formation of droplets instead of continuous flow. However, decreasing temperature resulted in a significant increase in the viscosity of the glass, followed by exhibiting shear thinning behavior. At 65°C, the carbohydrate glass showed excessive shear thinning behavior in a wide range of frequencies, with almost one order of magnitude decrease in the value of complex viscosity by sweeping from low to high frequencies.

Considering the thermal and rheological characterization of Isomalt, it was envisioned that, by maintaining the glassy state at a suitable temperature, a continuous flow of material for the jet formation during MEW could be achieved. Initial screening experiments revealed that lowering the set temperature in the two-component heating

unit to 90°C (cartridge zone) and 65°C (nozzle zone) enabled a continuous flow of glass with proper flexibility of the fiber during the deposition. In this way, the bulk of glass within the syringe cartridge had enough viscosity to tolerate above-atmospheric pressures, while the extruded glass showed pronounced shear-thinning behavior enabling the drawing of very fine microfibers from the nozzle with the aid of the applied electrical field.

2.4.2 Melt electrowriting of Isomalt

A series of experiments were designed to investigate the processability of Isomalt glass with MEW. Three main parameters of the MEW process were selected and systematically changed between five equidistant levels to obtain and assess an operational window for the production of fibers with different diameters. **Table 1** shows the configuration of constants and the investigated parameters, and the corresponding values for each level. The investigated parameter space did not include different temperatures since our preliminary results indicated that alteration of the temperature of the nozzle results in a significant shift in parameter space, mainly due to a significant change in the viscoelasticity of Isomalt glass. For this reason, the influence of temperature on the resulting MEW fiber diameter was not considered.

Initially, the CTS for the production of straight fibers in each experimental set was determined. Determination of CTS, as the transition point between coiled to straight fiber deposition, is crucial in further analysis of printability [156]. **Figure 9**A shows the influence of different process parameters on the CTS, accompanied by an exemplary image of the transition between two deposition behaviors at CTS. An increase in CTS value usually indicates the formation of a faster jet during the MEW process. This phenomenon could be explained by considering the correlation between the pulling force induced by the applied electrical field and the mass flow through the nozzle [156]. Lower pressure resulted in less mass flow from the nozzle in a constant electrical field intensity, which resulted in whipping and deviation of the formed thin fibers from the designed path [156]. Similarly, at a constant pressure, increasing the applied electrical field resulted in more jet instability. To compensate for the induced whipping effect, the collector speed should be increased continuously to enable straight fiber deposition. Decreasing the distance between the nozzle and the collector also resulted in the formation of a faster jet. A faster jet could result from the increased electrical force exerted on the glassy jet, even though the same nominal value of the electrical field was applied to both poles.

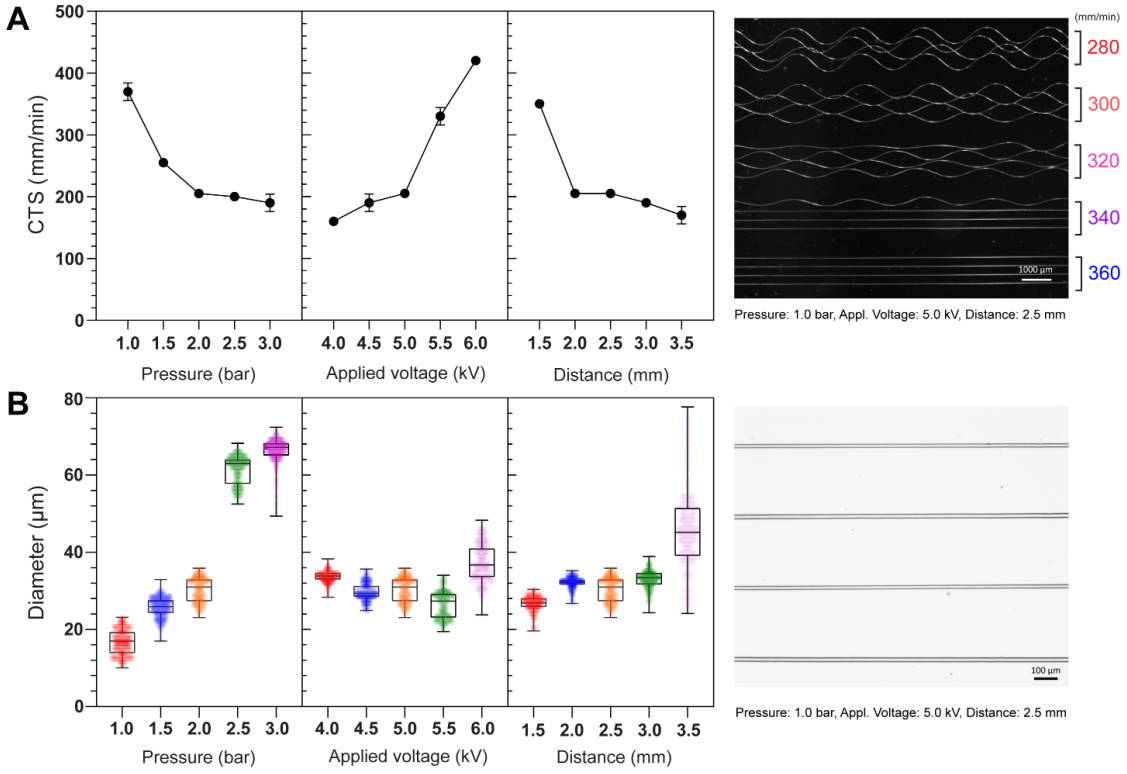

Figure 9. Influence of MEW parameters on CTS value and the resulting fiber diameter. A) Variation of CTS based on different parameter combinations in three categories of parameters. An exemplary image of MEW Isomalt glass fibers showing the transition of deposited fibers from coiled to straight by reaching CTS. **B**) Influence of three MEW parameters on Isomalt glass fiber diameter. The deposition velocity was set to 10% higher than the corresponding CTS value for the respective combination of process parameters. An exemplary image shows the morphology and quality of produced Isomalt fibers deposited in predefined patterns.

After determining CTS for forming a stable jet for each experimental condition, the next step was to investigate the influence of these sets of parameters on the deposited glass fibers' diameter. **Figure 9**B shows the measured values of deposited fibers by varying one process parameter at a time. The collector speed in these experiments was set to be 10% above the CTS value for respective sets, ensuring the observed changes in fiber diameters are not due to the stretching of the glassy jet because of a mismatch between mass flow and mechanical pulling forces.

In all three categories of parameters, changing the corresponding variable's value resulted in a significant fiber diameter change ($p < 0.05$). Despite the almost uniform change in each experimental category's diameter values, the occurrence of outliers at extreme values of each parametric range resulted in the deviation of measured average values from the expected trends. Increasing the applied pressure to 3.0 bars resulted in an imbalance of mass flow and electrohydrodynamic (EHD) forces applied to the glassy material at the nozzle tip and resulted in a phenomenon termed "pulsing" of the electrified molten jet [156]. Under these conditions, the diameter of the fiber changes periodically. During the increase of pressure from 2.0 to 2.5 bars, the experimental observations

showed that the jet's stability was significantly influenced by increasing the mass flow. However, this impact did not result in an evident periodic change in diameter, as was expected during fiber pulsing. We speculate that the jet's overall stability could be compromised by increasing the pressure above 2.0 bars, but the extent of this effect is proportionally dependent on the applied pressure. Noteworthy, the large variance of the fiber diameter observed by increasing the applied voltage to 6.0 kV was not mainly due to the pulsing effect. We speculate that the observed behavior could be attributed to the speed of the glassy jet descending upon the collector surface. Given a constant travel distance from the nozzle to the collector, a faster jet would result in a shorter travel time, leading to the deposition of softer glassy fiber at a higher temperature. This might cause the local spreading and deformation of the fibers with broader statistical deviations. It should be noted that experimental and computational data showed that in addition to natural convection and radiation, the EHD effect could enhance the heat transfer during the landing of the molten jet [122]. The possible counter-influence of EHD heat transfer enhancement on the cooling of the glassy Isomalt jet could compensate for the shorter cooling period during the landing of the high-speed jet, but confirmation of this hypothesis would need detailed characterizations, which are not in the scope of this study.

A significant variation in fiber diameter at large tip-to-collector distances was observed. This effect can be attributed to the plasticity of the jet, where the larger distance at constant applied voltage leads to weaker electrohydrodynamic forces and, thus, a slower landing of the jet. The slower travel speed promotes lower jet temperature upon landing, causing artifacts in deposited fibers due to mechanical forces induced by the lack of plasticity.

Despite the challenges in stabilizing fibers at the extremes of the investigated experimental window, it was observed that by adjusting easy-to-control parameters, successful deposition of Isomalt microfibers with reasonable control over the dimension could be achieved. In contrast to conventional extrusion 3D printing, the combined application of electrical and mechanical forces to draw a fine fiber in MEW provides the technical advantage of working with materials with higher inherent viscosity. On the one hand, this implies the possibility of lower process temperatures, which is in favor of avoiding the thermally induced deterioration of the material properties. On the other hand, the higher viscosity of the melted or glassy material could potentially enhance the resolution and stability of the drawn fibers at the same time. The excellent processability of Isomalt by MEW could be correlated with the ease of drawing a thin glassy jet with enough plasticity and viscosity to yield stable fibers with controllable dimensions.

2.4.3 High-resolution templating of microchannels

As mentioned in the introduction, MEW is a powerful method for the fabrication of fibrous constructs with well-ordered microstructure [127]. A significant aspect of this technology is the potential to alter the process parameters on-the-fly, meaning that deployment of continuous and on-demand features of the design is possible. Previous studies using poly(ε-caprolactone), the "gold standard" material in MEW, showed that by merely changing the collector's speed, a wide range of fiber diameters between 2-50 μm within the same construct could be achieved [125]. It has also been shown that a systematic variation of several process parameters enables optimization and parametric prediction of the MEW process [165]. With such flexibility in controlling the dimensional features using MEW, the fabrication of templating structures from Isomalt could provide the opportunity to create microchannels within a substrate with multiple scales of hierarchy. It should be noted that the experimental window for the fabrication of Isomalt fibers by MEW is not limited to the investigated sets of parameters reported so far in this study and their corresponding ranges. Practically, as long as the balance between mass flow and the electrohydrodynamic forces could be maintained, a stable jet formation would be expected [163].

The Isomalt fibers can be quickly and selectively dissolved by exposure to humidity or generally an aqueous media. Recent reports on the 3D printing of sugars showed that by embedding such structures in a matrix of choice, it was possible to generate channels for different application fields ranging from microfluidics to biofabrication. Selective casting and removal of sacrificial geometries is a well-established method for the generation of hollow structures, including microchannels; however, increasing the design's intricacy would practically limit its applicability [151]. In this respect, a fugitive structure made of a water-soluble sugar such as Isomalt with different dimensions and structural complexity levels would significantly extend the manufacturing possibilities. In order to facilitate the embedment of sacrificial fibers, the MEW of Isomalt was directly performed on PDMS substrates. Although the electrical conductivity of PDMS is less than glass substrate, glass is more prone to undergo polarization in a constant electrical field due to the higher relative permittivity. This combination resulted in almost similar behavior of the two substrates, and the jet formation was not significantly impacted. Modeling the electric field distribution and the applied electric potential on each substrate's surface showed consistency in the applied field's distribution and intensity during applying different electrical potentials to the nozzle (**Figure 10, Figure 11**). However, suppose a thorough characterization of the MEW process using a PDMS substrate is desired. In that case, the interested reader is encouraged to follow the

similar methodology described in the previous section to derive a more detailed correlation between fiber diameter and MEW parameters.

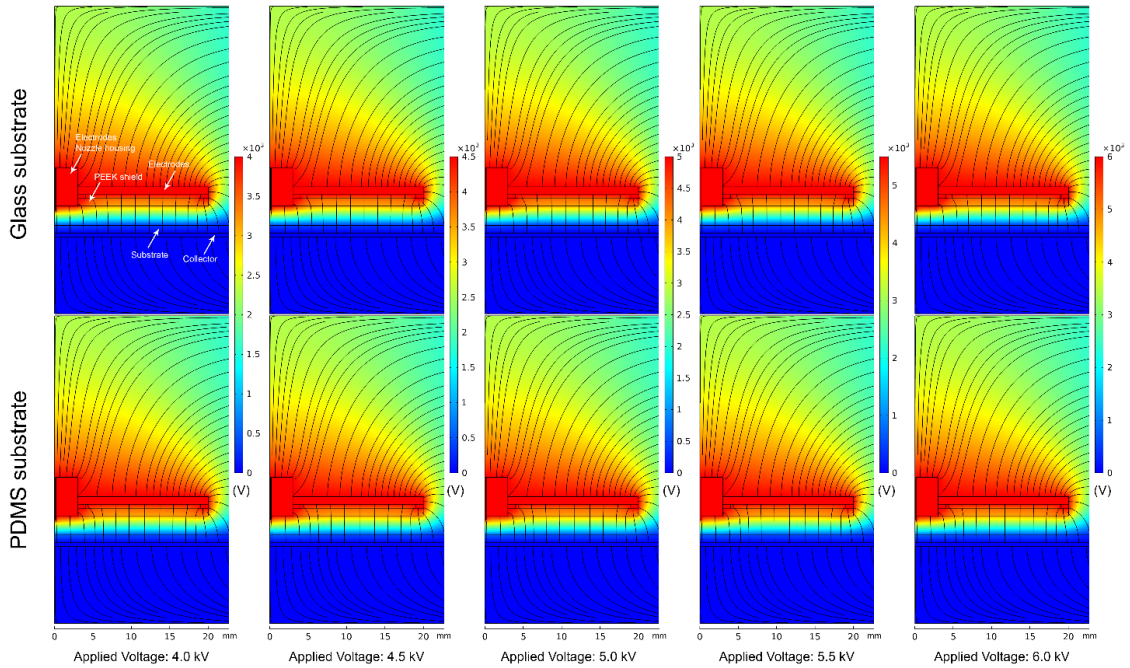

Figure 10. Numerical modeling of the applied electrical field with different magnitudes with both glass (top row) and PDMS (bottom row) substrate over the collector. The geometry of the printhead and the boundary conditions were based on experimental data.

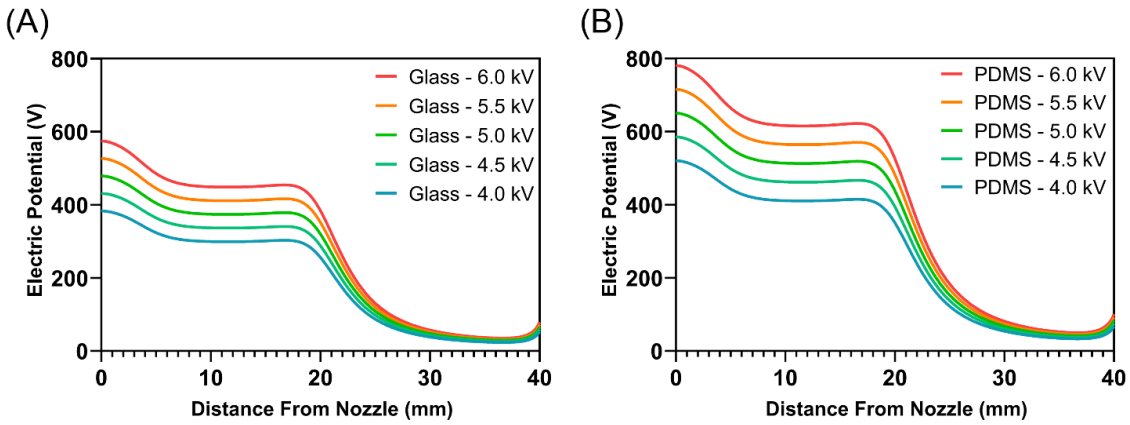

Figure 11. Results of the numerical modeling of the electrical field for the electric potential applied over the surface of the substrates A) glass and **B**) PDMS with respect to the distance from the nozzle. The geometry and values of boundary conditions were based on experimental data.

To investigate the suitability of Isomalt glass fibers produced by MEW for the fabrication of microchannels, intricate designs based on continuous fiber deposition with multiple levels of diameter change were evaluated and transferred to a proof-of-concept study. **Figure 12** shows the region-based alteration of MEW parameters to fabricate a continuous path with diameters varying between 30 to 200 µm. The first region of the microchannel design mimics the conventional inertial focusing/mixing design in conventional microfluidics. The curvature of the channel in this region led to a sequential

change in fiber diameter, which might be of interest in specific applications such as continuous inertial focusing of flow or microparticles [166]. In the study presented here, that region was added to demonstrate the flexibility of MEW in adjusting and altering the geometry of the deposition pattern. It is worth mentioning that the implementation of this region of the design by MEW was the most demanding portion of the process. The deposition of thick fibers in this region required pushing the MEW process to the limits that were not accessible in the previous section's parameter space. This was mainly due to the restrictions in translation speed and applied voltage imposed by the requirements in Section 2.4.2. Hence, a change in the parameter space was required. Further on, a region with a gradual reduction in diameter connected to a long microchannel with a fixed value of diameter was produced. A controlled change in the diameter of microchannels provides the possibility to achieve adjustable flow rates within the design, even with a constant inlet pressure or flow rate. This feature might be especially appealing for applications involving the analysis of flow behavior in microfluidics or tissue engineering. The significant technological aspect in the fabrication of such structures lies in the correlations between the actual diameter of the deposited glassy fibers and the on-demand and automated change of MEW parameters implemented within the G-code path plans. By removing the MEW Isomalt fibers from the PDMS matrix using a simple immersion in a water bath, a hollow and perfusable continuous microchannel platform with accurately designed dimensions was produced.

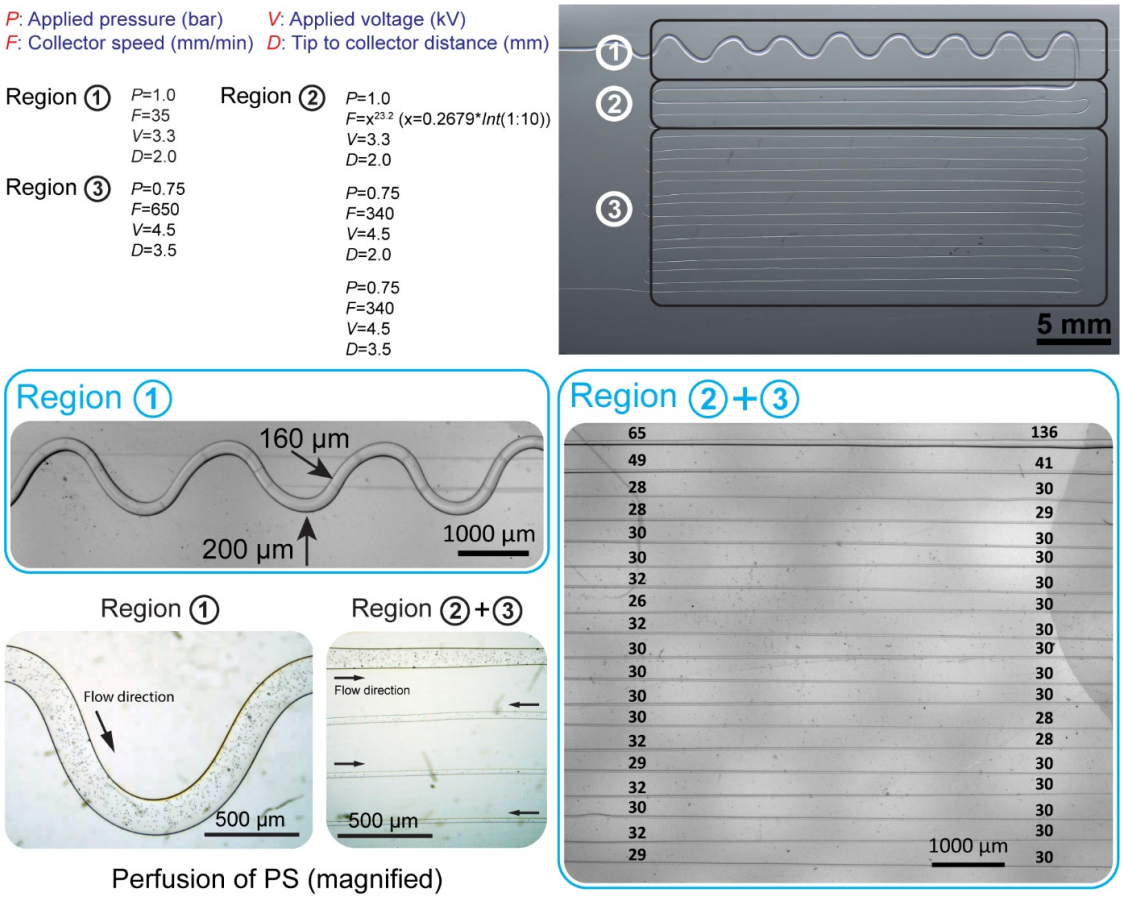

Figure 12. An example of an intricate design of microchannels produced from Isomalt glass fibers in a single run through controlled on-the-fly adjustment of MEW parameters. Region 1 and 3 of the design mimicked the conventional designs of microchannels in microfluidics with a transition Region 2 connecting both designs in a controlled and stable way. Fiber diameter was decreased from 200 µm in Region 1 to 30 µm in Region 3, with three steps of sub-transitions within Region 2 using four easy-to-control parameters. The collector speed in Region 2 was increased exponentially through a 10-step discrete incremental loop. The hollow channels embedded in PDMS could be further perfused with Polystyrene (PS) microparticles (magnified sub-panels).

The current literature on templating microchannels using 3D printing of sugar glasses reveals the technological limitations of reaching sub-100 µm dimensions [145-149, 151, 152]. Our demonstrated proof-of-concept study shows that by applying MEW, the resolution can be significantly advanced down to channel diameters of 30 µm. Beyond that, it additionally opens the possibility to fabricate geometries with a wide range of dimensions with size scales ranging from the domain of conventional 3D printing technologies down to the limits of lithography-based techniques in a one-step process.

2.5. Conclusion

We demonstrate the applicability of MEW for the well-controlled production of microfibers from Isomalt. The results show that by precise control over the MEW parameters, Isomalt glass microfibers with a wide range of diameters down to 20 µm can be fabricated. The water solubility of Isomalt provides an easy-to-implement method for the removal of embedded fibers in the final structure, resulting in the formation of perfusable microchannels with on-demand control of the diameter. The flexibility of this process was shown in a proof-of-concept design of microchannels with controlled alteration of fiber diameter between 30 to 200 µm in a one-step fabrication process. This one-step fabrication procedure represents a technological step ahead, which addresses the current limitations in the production of templating structures from fugitive sugar glasses in application areas such as microfluidics.

Chapter 3

A print-and-fuse strategy for sacrificial filaments enables biomimetically structured perfusable microvascular networks with functional endothelium inside 3D hydrogels

Chapter 3 was published as part of an original research article (Ryma, M.*, Genç, H.*, Nadernezhad, A.*, Paulus, I., Schneidereit, D., Friedrich, O., Andelovic, K., Lyer, S., Alexiou, C., Cicha, I. and Groll, J., 2022. A print-and-fuse Strategy for Sacrificial Filaments Enables Biomimetically Structured Perfusable Microvascular Networks with Functional Endothelium Inside 3D Hydrogels. *Advanced Materials*, p.2200653.), reproduced from reference [167], which is an open-access article under the terms of the Creative Commons Attribution-NonCommercial License 4.0.

* equally shared author contributions

This chapter is based on the work of the author of this thesis Ali Nadernezhad, who performed the optimization of the fabrication process, computational flow analysis, data evaluation, and composition of the manuscript. Development of the general strategy using Polyoxazolines for microvascular structure formation, the evolution of the print pattern, the design and fabrication of the bioreactor, and the relevant biological studies were performed by other co-authors, Mathias Ryma and Hatice Genc.

3.1 Abstract

Current methods of microvessel fabrication mostly rely on self-assembly in tiny volumes, prefabricated designs of microchannels, or demand complicated multi-step procedures based on sacrificial templating to achieve specific geometrical features. Such application-oriented geometries subsequently require a design-specific and functional perfusion system that must be developed in parallel. In this study, we present a facile and flexible approach for the integration of biomimetically branched microvasculature within bulk hydrogels. For this, sacrificial scaffolds of thermoresponsive poly(2-cyclopropyl-2-oxazoline) (P*cyclo*PrOx) are created using Melt Electrowriting (MEW) in an optimized and predictable way and subsequently placed into a customized bioreactor system, which is then filled with a hydrogel precursor solution. An aqueous environment above the lower critical solution temperature (LCST) of P*cyclo*PrOx at 25°C swells the polymer without dissolving it, resulting in the fusion of filaments that were deposited onto each other (print-and-fuse approach). Accordingly, an adequate printing pathway design results in generating physiological-like branching and channel volumes that approximate Murray's law in the geometrical ratio between parent and daughter vessels. After gel formation, a temperature decrease below the LCST produces interconnected microchannels with distinct inlet and outlet regions. Initial placement of the sacrificial scaffolds in the bioreactors in a pre-defined manner directly yields perfusable structures via leakage-free fluid connections in a reproducible one-step procedure. Using this approach, the rapid formation of a tight and biologically functional endothelial layer, as assessed not only through fluorescent dye diffusion but also by tumor necrosis factor alpha (TNF-α) stimulation, is obtained within three days.

3.2 Introduction

The growing awareness of the limitations of conventional two-dimensional (2D) cell culture techniques gave rise to an expanding interest in 3D tissue models, which enable obtaining more accurate results, particularly in biology, medicine, and pharmacy. This relies primarily on creating a more realistic cell environment since cell-cell and cell-matrix interactions in 3D models are more comparable to the *in vivo* conditions [168, 169]. Additionally, these artificial 3D tissues may potentially be used as tissue replacements for regenerative medicine [170].

There is a critical challenge in creating artificial 3D tissue models larger than 0.6-1 mm, depending on the matrix and cell density. According to the *in vitro* measurements in 3D spheroids reported by Grimes et al. [171], the upper limit of the oxygen diffusion distance of 232 ± 22 µm was observed experimentally. In larger tissue models, the supply of oxygen and nutrients cannot be ensured by osmosis, leading to a necrotic core generation [172]. *In vivo*, the vascular system guarantees the nutrient supply through a complex network of large arteries branching into smaller vessels and capillaries [5]. To overcome this size limitation in artificial tissues or cell-based organoids exceeding a certain thickness, it is necessary to generate microchannel networks to keep cells alive by supplying oxygen and nutrients. The microchannel networks must be perfused with media through a perfusion pump or other flow-inducing systems to ensure oxygen and nutrient supply, as well as metabolic waste removal.

The state-of-the-art technologies for the generation and utilization of reproducible microchannels are based on “organ-on-a-chip” (OoC) systems, which allow the emulation of physiological reactions of organ-like systems via connection to microfluidic systems [173]. Although OoC systems provide channel structures, they are only a part of an artificial molded container to which cells are attached. Furthermore, cell populations such as endothelial cells are divided by permeable membranes from other cell populations, which may inhibit both the mechanical stimuli and the direct interactions between different cell types. While the OoC system proved to be a valuable research tool in studying cellular metabolism and drug screening, their inherent limitation in mimicking the 3D cellular microenvironment has impacted their potential for creating large 3D tissues.

An artificial 3D matrix should mimic complex cellular interactions and facilitate cell attachment, survival, and proliferation in a 3D environment. Hydrogels are of particular interest in this context since they can provide a permeable microenvironment, which can be further physically and chemically tuned based on particular needs. Despite the

aqueous nature of hydrogel matrices, limitations based on diffusion distance demand the adaptation of microvascular systems into such 3D microenvironments.

During the past decade, advances in manufacturing technologies enabled the creation of complex 3D microvascular systems, and in particular, approaches based on Additive Manufacturing (AM) gained much attention in recent years. Among different AM technologies, 3D bioprinting allowed the generation of in situ microchannels within 3D-hydrogel constructs containing cells. In this way, the microchannels can be either created by introducing empty spaces during printing or by deposition of sacrificial inks, which can be removed afterward. Among other methods, techniques, including extrusion-based printing [150], in-gel printing [174], and stereolithography [175], were reported. However, these methods were mainly limited by the low resolution, the need to adapt hydrogel properties to the process criteria, and the shear-related cell viability issues [176]. In particular, the direct ink writing of templating fugitive inks extensively explored by the group of J. Lewis aimed to expand the scopes of printability and functionality of sacrificial templating by taking advantage of relatively easy-to-handle thermoresponsive sacrificial inks based on pluronics and gelatin [93, 113]. This approach has further evolved to direct sacrificial writing into functional tissues (SWIFT) by creating a sacrificial template within organ-specific and high-density cellular aggregates [114].

Alternatively, methods based on templating microchannels have been developed using sacrificial structures that are separately 3D-printed and subsequently embedded in hydrogel matrices. The rationale behind this new trend was mainly addressing the size and, more importantly, spatial limitations of the direct writing approach. The initial reports on this technique were based on embedding 3D-printed carbohydrate-based microfibers within the bulk hydrogel matrices [177, 178]. Although this approach could potentially improve the resolution and freedom of the design in creating microchannels, two main challenges still need to be addressed. The sacrificial structures based on carbohydrates readily dissolve in an aqueous environment, making the embedment of sacrificial scaffolds impossible in almost any hydrogel matrix without the loss of their geometrical features. Post-processing methods such as coating with polymers, hydrogels, or other materials are often required to increase the timeframe of gelation, increasing the difficulty with the increasing complexity of the scaffold [179, 180]. Furthermore, the high hygroscopicity of carbohydrate sugars limits scaffolds' storability in standard room conditions.

More importantly, while the majority of the studies focused on developing case-specific methods of creating microchannels, none thus far tried to propose efficient

methodologies for integrating the microchannels into perfusion systems. Most of the reported efforts were focused on the post-fabrication creation of in- and outlet regions by manual insertion of microneedles. Considering the small dimensions of the formed channels, especially in microvascular systems, the precision of embedment of the sacrificial scaffolds and establishing a closed perfusion loop is of tremendous importance. In this way, two main aspects of producing a functional microvascular model could be identified, which include (a) methodologies for the fabrication of microchannels and (b) their further integration into a perfusion system to enable the biological functionality of the created microvasculature.

By considering these two aspects, this study addresses the challenges in fabricating perfusable and functional microvascular structures by developing a novel approach based on embedding thermoresponsive sacrificial scaffolds made from poly(2-cyclopropyl-2-oxazoline) (P*cyclo*PrOx) integrated within a custom-designed, adaptable bioreactor. The sacrificial P*cyclo*PrOx structures with dimensions in the microvasculature range were produced by Melt Electrowriting (MEW) [156]. The precise positioning and fixation of the sacrificial scaffolds at the inlet and outlet of a newly developed bioreactor enabled blockage-free casting of the hydrogel matrix within the perfusion chamber, ensuring that the channels remain perfusable. P*cyclo*PrOx scaffolds with a lower critical solution temperature (LCST) of 25 °C were removed simply by a short incubation below the room temperature, providing enough time for gelation of the hydrogel matrix through a fully biocompatible process. Compared with state of the art in literature such as the SWIFT approach, the methodology presented here addresses the limitations in realizing low-dimension microchannels with significant flexibility in design and a generalized solution to integrate the microchannels within the perfusion systems. The proposed methodology resulted in the one-step fabrication of microchannels fully integrated within the bioreactor, ready for subsequent endothelialization and functional assessments. We demonstrated that a functional endothelial monolayer could be created inside these channels within 72 hours using a static seeding set-up followed by fluid perfusion. The advantages of this system, including adaptable channel diameters and designs, good storability at room conditions, facile removal of sacrificial structures, and rapid endothelialization, could make this system an important milestone in developing vascularized tissue constructs.

3.3 Materials and methods

3.3.1 Melt electrowriting

An in-house developed MEW printer was used to produce sacrificial scaffolds, and the related details are described elsewhere.[156] In order to produce homogenous fibers, the polymer reservoir in the MEW printer was equipped with two heating zones, one at the syringe body and another at the nozzle. Different temperature profiles for MEW of P*cyclo*PrOx are listed in **Table 2**. A heated collector plate connected to a temperature controller (C448, Hotset, Germany) was used to enable precise control over fiber deposition.

Table 2. Temperature (T.) profiles for MEW of P*cyclo*PrOx

Material	T. Syringe (°C)	T. Nozzle (°C)	T. Collector plate (°C)
P*cyclo*PrOx	210	225	70°C

The G-codes used in this study were based on the simplified geometry of bifurcated branching structures. In summary, bifurcated scaffolds were considered as two mirrored sections, each composed of 3 segments. **Figure 13** shows the drawing of the different regions of each scaffold used for the generation of G-codes. Starting and ending points of each line segment are identified in consecutive numbers. This single unit of bifurcated geometry could be used for structures with multiple levels of bifurcations. The geometrical distances between the design points of every single scaffold are vertically mirrored, as demonstrated in **Figure 13** (blue and pink design points).

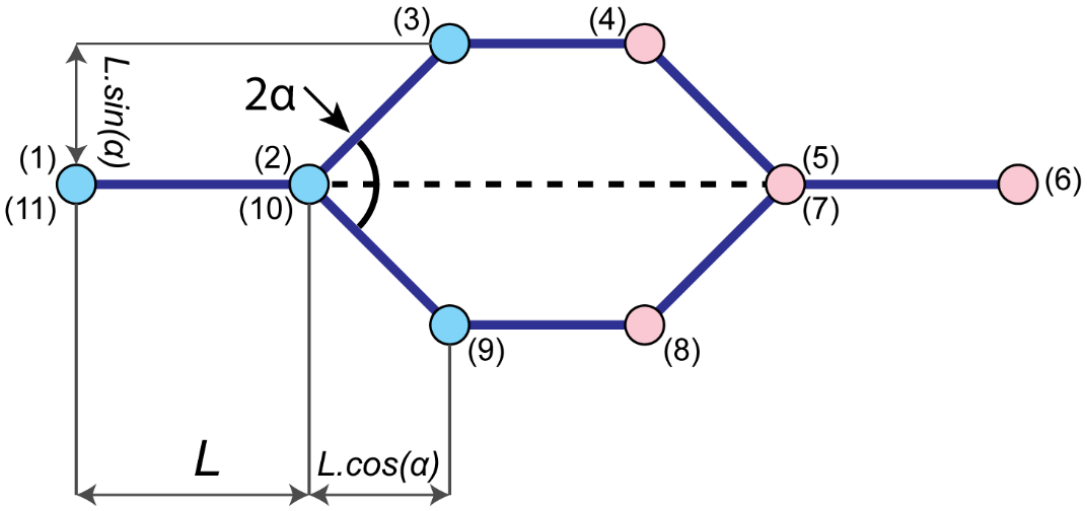

Figure 13. Parametrized geometry of each bifurcation unit and the corresponding order for developing the relevant G-code. The numbers indicate the order of the coordinates used for building the G-code for each scaffold with a single bifurcation. The length of the parent segments could be extended on demand.

3.3.2 Design of Experiments (DoE) for prediction of fiber diameter

Response surface methodology (RSM) was used to investigate the individual and interaction effects of MEW process parameters on the resultant P*cyclo*PrOx diameter. Three process parameters at three levels were chosen to construct the DoE based on a Box-Behnken design with three center points using Design-Expert software (version 13, Stat-Ease, Inc. Minneapolis, MN, USA). The details of the parameters and their values are listed in **Table 3**. Fiber diameters were measured using a stereomicroscope (DMS-1000, Leica Microsystems, Germany) on scaffolds printed with one level of bifurcation. The obtained images were quantified using Fiji [181]. The final diameter value for each run was based on the average value of diameter obtained from at least 150 measurements on 15 different scaffolds, randomly chosen from a pool of 30 generated with the same experimental conditions. A polynomial equation was used to fit the experimental data, and it was evaluated by analysis of variance (ANOVA) and coefficient of determination (R^2). The significant parameters were determined using F-value by calculating $F_{critical}$ and P-value with α=0.05. A power model transformation was used to find the best fit. The obtained model was validated by producing three sets of different one-level bifurcated scaffolds, with MEW parameters chosen randomly within the experimental range.

Table 3. Parameters and their corresponding ranges (coded and actual values) for the creation of different runs of the DoE

Parameters	**Coded**	**Coded Levels (actual values)**		
Pressure (bar)	P	-1 (1)	0 (1.5)	+1 (2)
Voltage (kV)	V	-1 (2.5)	0 (3.0)	+1 (3.5)
Distance (mm)	H	-1 (3.0)	0 (3.5)	+1 (4.0)

3.3.3 Creation of microchannels within bioreactors

Sacrificial P*cyclo*PrOx scaffolds were placed on the saddle supports of the bioreactors and fixed on their position using a 1:1 dilution of 30% wt./v P*cyclo*PrOx in MilliQ solution. After drying the adhesive at room temperature, glass coverslips with the standard dimension of 25×60 mm were attached to the bottom part of the bioreactor using a fast-setting silicone resin (Dublisil 15, Dvreve, Germany). After setting the resin, bioreactors with sacrificial scaffolds were sterilized under UVC light for 15 min. Gelatin-methacryloyl (GelMA, gel strength 300 g Bloom, 80% degree of substitution, Sigma-Aldrich, Munich, Germany) was dissolved in cell culture media at 7% final concentration

at 37^{o} C. Lithium-phenyl-2,4,6-trimethylbenzoylphosphinat (LAP) was used as the photoinitiator. A 0.5% wt./v stock solution of LAP in PBS was prepared and stored at 4^{o}C, and a final concentration of 0.05% wt./v was used to crosslink the GelMA hydrogel. Hydrogel precursors to prepare 400 µl of final hydrogel were inserted into the main chamber of the bioreactor and crosslinked by a UVA light source (Vilber Lourmat, Marne-la-Vallée, France) for 8 minutes. Once crosslinking was completed, PBS solution was added to the bioreactor chambers to dissolve the sacrificial scaffold, and if demanded, bioreactors were placed shortly on ice to reduce the dissolution time.

4.3.4 Computational flow analysis

3D modeling of bifurcated microvessels

The reconstruction of the 3D models was performed in Solidworks software (Dassault Systèmes, Vélizy-Villacoublay, France). The 3D model of the real geometry was produced based on the 3D mosaic stacks of the whole endothelialized microchannels acquired using multiphoton microscopy. The parent and daughter sections of bifurcated microvessels were generated by a controlled loft function of an ellipse cross-section with the ratio of the diameters of 4:3.1 along the degree 9 Bezier curves. The apex radius of the bifurcation zones was extracted from the microscopy images. The 3D models with different bifurcation angles were designed by a parametric approach described elsewhere [182]. For the parent and daughter segments, perfect circular cross-sections with diameters of 500 and 400 microns were considered, respectively.

Flow simulations in 3D models

The flow profile of cell culture media or blood in 3D models of bifurcated microchannels was computed using Ansys Fluent (Ansys, Canonsburg, USA). The inlet mass flux was determined based on experimental values. The viscosity and density of the cell culture media were obtained from the data reported by Poon [183]. The *in vitro* viscosity law developed by Pries et al. [184] at the parent vessel was adopted and implemented for both parent and daughter segments. The hematocrit for the determination of blood viscosity was fixed at 0.45. Both the cell culture media and the adopted blood viscosity profiles were assumed to behave as Newtonian fluids. The influence of gravity on flow during the perfusion was considered in all the computations with atmospheric pressure as boundary condition.

3.4 Results

3.4.1 Melt Electrowriting of sacrificial P*cyclo*PrOx scaffolds and their behavior in hydrogels

Prior to the MEW, the synthesized P*cyclo*PrOx was thoroughly characterized to confirm the desired chemistry and physical properties. A significant advantage of the MEW is the tunability of the process, by which one can produce fiber diameters ranging over several orders of magnitudes [89, 125, 165]. We showed this capacity of MEW by following a Response Surface Methodology (RSM) design of experiments to produce scaffolds with predictable fiber diameters. A three-factor design of experiments (DoE) with three-level for each factor was designed and applied to randomly generate the experimental runs, including three center points to assess the model's bias. By choosing a convenient jet-forming range of the simple-to-adjust parameters, namely the applied pressure (*P*), the applied voltage (*V*), and the tip-to-collector distance (*H*), it was possible to construct an optimized model to predict fiber diameter (*D*) (**Equation 1**).

$$\boldsymbol{D}^{-0.39} = 0.400708 - 0.177373\boldsymbol{P} - 0.004729\boldsymbol{V} - 0.081932\boldsymbol{H} - 0.018362\boldsymbol{PV} + 0.022047\boldsymbol{PH} + 0.016363\boldsymbol{VH} + 0.040540\boldsymbol{P}^2 \quad \textbf{(Equation 1)}$$

Table 4 summarizes the experimental runs, the values of each parameter per run, and the average diameter measured for each condition.

Table 4. List of experimental runs based on DoE

Run	P: Pressure (bar)	V: Voltage (kV)	H: Distance (mm)	D: Diameter (μm)
1	1.5	3.5	4	146.976
2	2	3	3	243.427
3	1.5	3	3.5	184.236
4	2	2.5	3.5	275.05
5	2	3.5	3.5	182.087
6	1.5	3.5	3	160.769
7	1.5	2.5	3	207.726
8	1.5	3	3.5	202.022
9	2	3	4	179.661
10	1.5	3	3.5	175.858
11	1	3.5	3.5	86.9934
12	1	3	4	121.732
13	1.5	2.5	4	265.886
14	1	3	3	108.087
15	1	2.5	3.5	162.458

A power transform based on the Box-Cox plot was applied to the response. The quadratic polynomial model used to fit the data was analyzed by ANOVA, and the results are presented in **Table 5**.

Table 5. Results of ANOVA for a full quadratic model

Source	Sum of Squares	df	Mean Square	F-value	p-value	
Model	0.0042	9	0. 000465	29.29	0.0008	significant
P-Pressure	0.0023	1	0. 002268	142.94	< 0.0001	
V-Voltage	0.0012	1	0. 001250	78.78	0.0003	
H-Distance	1.045E-07	1	1.045E-07	0.0066	0.9385	
PV	0.0001	1	0. 000084	5.31	0.0693	
PH	0.0001	1	0. 000122	7.66	0.0395	
VH	0.0001	1	0. 000067	4.22	0.0952	
P^2	0.0004	1	0. 000378	23.80	0.0046	
V^2	5.260E-06	1	0.000005	0.3315	0.5897	
H^2	2.839E-06	1	0. 000003	0.1789	0.6899	
Residual	0.0001	5	0. 000016			
Lack of Fit	0.0001	3	0. 000018	1.42	0.4396	not significant
Pure Error	0.0000	2	0. 000013			
Cor Total	0.0043	14				

Based on the results of ANOVA, the non-significant terms of the full quadratic model were removed, and the optimized model was selected. The results of ANOVA after optimization are presented in **Table 6**.

Table 6. Results of ANOVA for the optimized model

Source	Sum of Squares	df	Mean Square	F-value	p-value	
Model	0.0042	7	0.0006	47.39	< 0.0001	significant
A-Pressure	0.0023	1	0.0023	180.25	< 0.0001	
B-Voltage	0.0012	1	0.0012	99.34	< 0.0001	
C-Distance	1.045E-07	1	1.045E-07	0.0083	0.9299	
AB	0.0001	1	0.0001	6.70	0.0360	
AC	0.0001	1	0.0001	9.66	0.0171	
BC	0.0001	1	0.0001	5.32	0.0545	
A^2	0.0004	1	0.0004	30.48	0.0009	
Residual	0.0001	7	0.000013			
Lack of Fit	0.0001	5	0.000013	0.9868	0.5729	not significant
Pure Error	0.0000	2	0.000013			
Cor Total	0.0043	14				

The fit statistics were analyzed by evaluation of R^2 and Predicted R^2. The results showed that the obtained model fits the experimental data with about 98% accuracy, while it is capable of predicting the fiber diameter for an unseen set of process parameters with 88% accuracy. Although the results of ANOVA indicated that the contributions of the distance between the nozzle and collector (***H***) to the model are not statistically significant, this term was included in the final model to preserve its hierarchy.

To experimentally validate the obtained model, three random sets of parameters, according to **Table 7,** were selected. The measured fiber diameters for the validation sets were within the 95% Prediction Interval (PI) per each experimental run. **Table 8** summarizes the validation results for the obtained model.

Table 7. Level of randomly chosen parameters to validate the obtained model

Factor	Name	Level	Low Level	High Level
P	Pressure	1.50	1.0000	2.00
V	Voltage	2.50	2.50	3.50
H	Distance	3.50	3.00	4.00

Table 8. Measured diameters of validation experiments and their comparison with the predicted values based on the model

Analysis	Predicted Mean	Predicted Median	Std Dev	n	95% PI low	Data Mean	95% PI high
Diameter	244.215	243.2	1.43601	5	215.183	263.735	276.556
Diameter	140.933	140.551	0.541111	5	125.724	128.421	157.924
Diameter	137.349	136.983	0.516908	5	123.334	148.385	152.826

The fitted model's sanity check and the response surfaces generated for different binary combinations of process parameters are shown in **Figure 14**A-D. As expected from the literature, while the change in *H* imposes almost no significant change in fiber diameter, increasing *P* results in a significant increase in fiber diameter. In contrast, increasing *V* at constant *P* and *H* results in faster mass transfer, hence decreased fiber diameter. Experimental validation of the model showed that the predicted fiber diameters were within the 95% prediction interval. Within the range of process parameters used to build this statistical model, it was possible to fabricate bifurcated structures with average fiber diameters between 87 to 275 µm. However, it should be noted that the chosen range of process parameters was one of the possible combinations leading to the formation of the jet. Depending on the design requirements, a different range of parameters could be explored, leading to larger or smaller fiber diameters. Nevertheless, the application of RSM proved to be an efficient way to optimize and predict the diameter of P*cyclo*PrOx sacrificial scaffolds.

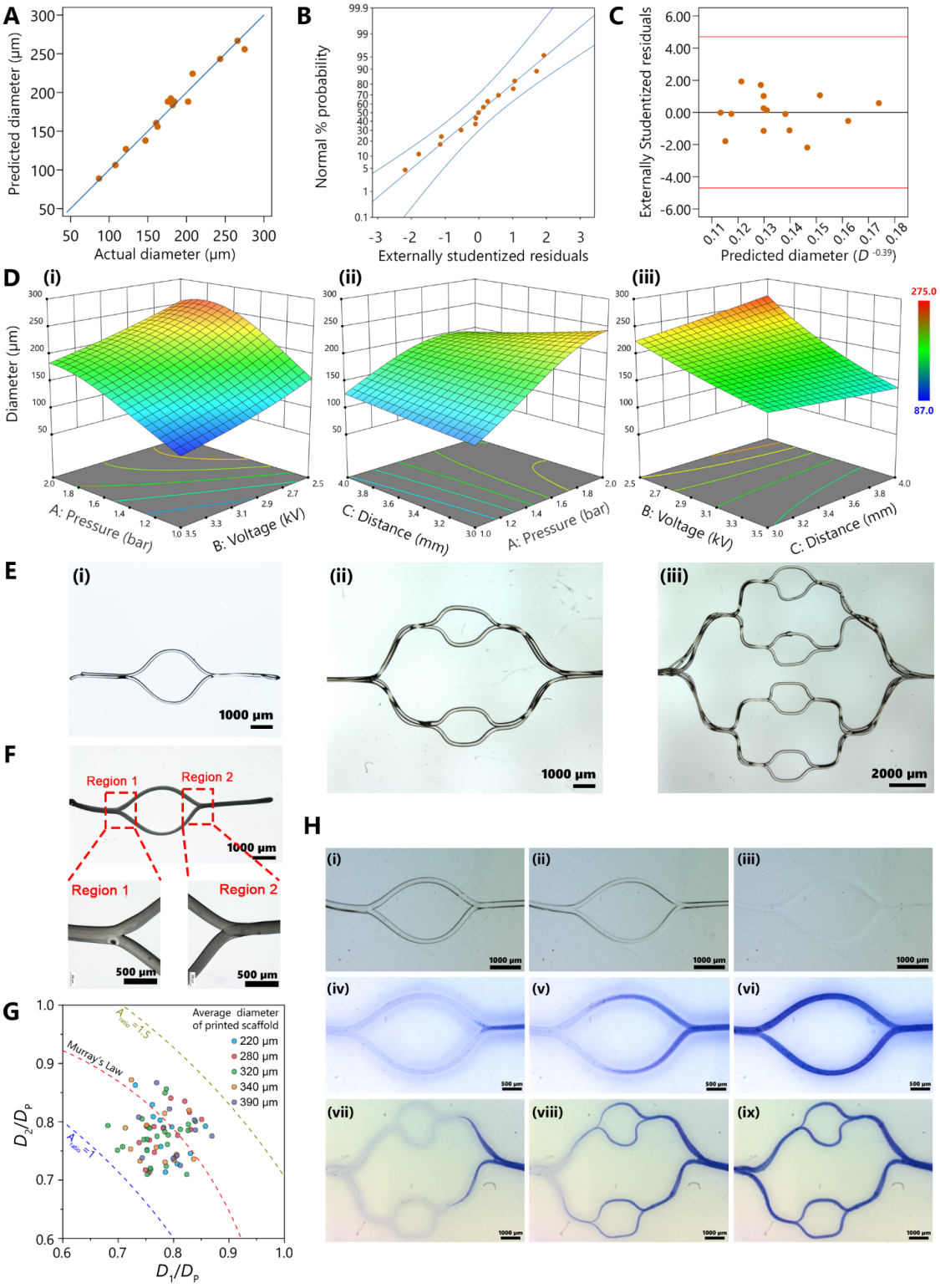

(Description on the next page)

Figure 14. Melt Electrowriting of scaffolds from P*cyclo*PrOx and their behavior in hydrogels. Sanity check for the derived statistical model by RSM to predict the fiber diameter: **A**) Actual versus predicted fiber diameters from the model, **B**) The normal plot of residuals (limits of the 95% confidence interval in blue lines), and **C**) Plot of the residuals versus predicted diameter to verify the random distribution of residuals. **D**) The response surfaces (i-iii) of binary combinations of MEW process parameters, showing the dependency of fiber diameter on model parameters. **E**) Examples of one (i) and multiple (ii, iii) steps of bifurcation in scaffolds as printed (in a dry state before the fusion step). **F**) Behavior of P*cyclo*PrOx -Scaffolds in GelMA hydrogel matrix: Upon immersion in the hydrogel precursor, the fibers swell, leading to the fusion of adjacent fibers (water-induced plasticity). The hydrogel precursors simultaneously evolve into a hydrogel network through crosslinking, resulting in the spontaneous formation of natural bifurcation structures. **G**) The correlation between parent and daughter vessel diameters with different initial dimensions of fugitive scaffolds. **H**) Time-lapse images of (i-iii) dissolution of P*cyclo*PrOx after temperature reduction below the LCST, (iv-vi) perfusion of interconnected channel system with one and (vii-ix) two levels of branching. Images in panels **E**, **F**, and **H** were taken by co-author Matthias Ryma and are provided here to preserve consistency in the follow-up discussions.

A simple G-code for the fabrication of sacrificial scaffolds was adopted. The implemented G-code for fiber deposition was designed to resemble natural bifurcating structures (**Figure 14**E). In order to produce multiple bifurcation steps, the level of complexity could be further increased by a few adjustments in the G-code (**Figure 14**E). However, increasing the complexity also increases the susceptibility to inaccuracies, as shown in **Figure 14**E-iii.

In the dry state, the printed constructs retain their shape exactly as printed, and filaments deposited on top of each other remain separate filaments. However, upon hydration of melt-electrowritten P*cyclo*PrOx scaffolds in an aqueous environment above the LCST, for example, by embedment in hydrogel precursors, spontaneous fusion and merging of neighboring filaments occurs (**Figure 14**F). The progressive softening and swelling of the fibers results in volumetric expansion, leading to the spontaneous fusion and formation of a single “parent channel” from two (or more) adjacent filaments. This process produces smooth surfaces by merging insoluble P*cyclo*PrOx filaments inside the hydrogel matrix so that small gaps between adjacent filaments are filled by swelling P*cyclo*PrOx unless the distance between neighboring filaments is too large. As stated above, this probability increases with the higher complexity of the structures (see, for example, **Figure 14**H-ix). The balance between the surface energy and viscosity of the P*cyclo*PrOx during the crosslinking of the hydrogel matrix aids the formation of natural branching structures. The formation of such natural bifurcations was observed in different embedding hydrogel matrices, including gelatin-methacrylol (GelMA), agarose, alginate, and gelatin crosslinked with transglutaminase.

Reducing the temperature below 25 °C resulted in swelling and dissolution of P*cyclo*PrOx fibers. Free swelling of P*cyclo*PrOx (i.e., open inlet and outlet regions within

the bulk hydrogel) resulted in rapid removal of the sacrificial scaffold without the aid of any external perfusion (**Figure 14**H-i–iii).

The water-induced plasticity of microfibers below the glass transition, simultaneously controlled by the increasing elasticity of the surrounding hydrogel matrix, thus resulted in the formation of bifurcated lumens, which were in good agreement with the extent of Murray's law (**Figure 14**G). The diameter ratio between parent and daughter microchannels created by the removal of fused filaments was between the expansion ratios of 1.0 and 1.5, as defined by the ratio between the sum of the squares of the diameter of daughter microchannels and the square of the diameter of the parent microchannel (**Equation 2**). This equation is derived as a measure of volume conservation during flow by considering the ratio between the area of cross-sections of the parent and daughter segments of a given channel by assuming circular lumens.

$$A_{ratio} = \frac{D_1^2 + D_2^2}{D_P^2} \qquad \textbf{(Equation 2)}$$

The expansion ratio is a geometrical index and can be described as “a measure for the expansion in cross-section area available to flow along the microvessel from parent to daughter branches.” This index is especially useful in analytical and computational solutions of the flow in microvasculatures and was preferred over a simple linear measure, as the latter does not necessarily reflect the geometrical correlations governing the branching and may not truly represent area and volume in any given segment of the microchannels with consideration of volume preservation. It must be noted that the expansion ratio as defined by **Equation 2** does not, in any form, describe the swelling of P*cyclo*PrOx fibers after placement in aqueous media but only refers to the channels generated in the hydrogel after the dissolution of the sacrificial template. Accordingly, the values of diameters in **Equation 2** refer to the diameter of microchannels, not the microfibers. This is also reflected by the color coding in **Figure 14**G, which shows that the correlation between the channel diameters created by the print-and-fuse method is not dependent on the as-printed fiber diameters.

Swelling of P*cyclo*PrOx resulted in creating microchannels with larger diameters than the templating fibers, with the swelling ratio ranging from 1.3 to 1.5 depending on the initial fiber diameter (**Figure 15**). The perfusion of formed structures with a dye (Coomassie blue) revealed that the channels and bifurcations remain interconnected (**Figure 14**H), even in more complex geometries.

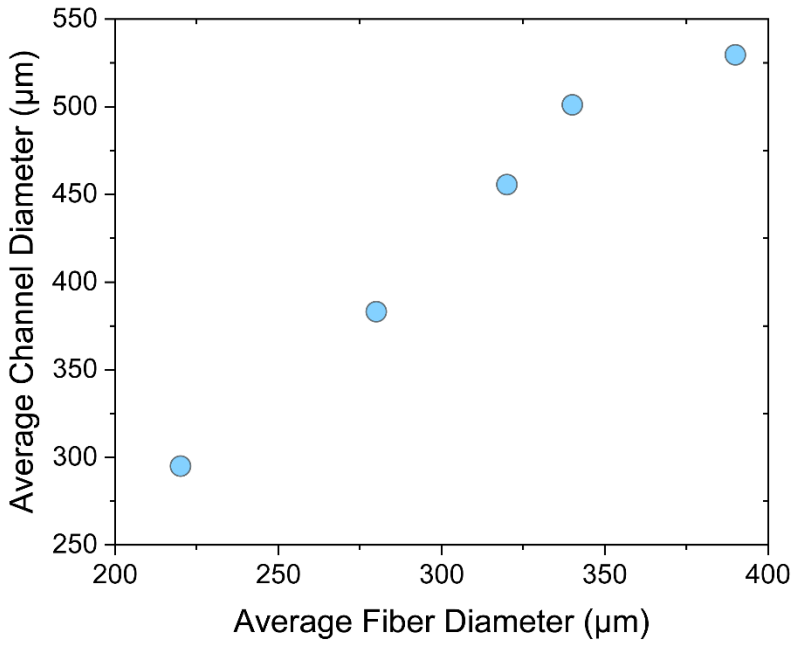

Figure 15. Swelling of microfibers results in forming channels with a larger diameter than the initial templating fiber.

3.4.2 Numerical analysis of flow within the embedded microchannels

A numerical flow simulation of the cell culture medium through the bifurcated channels was performed based on the 3D reconstruction of an endothelialized microchannel (**Figure 16**A). The expansion ratio above one resulted in decreased velocity of medium passing through the daughter branches, although minor irregularities in generated CAD model resulted in a slight increase in velocity at the outlet of one of the branching segments. However, this increase did not affect wall shear stress significantly, as the simulated value of flow-induced wall shear stress was generally minimal (0.05 Pa), except for the beginning and end of the bifurcating regions, where it reached about 0.1 Pa (1 dyn/cm^2) which was due to the lack of smoothness in generated 3D model. It should be noted that because of the simplifications made for the boundary conditions in numerical simulations, the outlet region was set to be at atmospheric pressure. This contributed to the absence of any back pressure within each perfusion half-cycle and, consequently, the slight overestimation of the outlet's flow velocity.

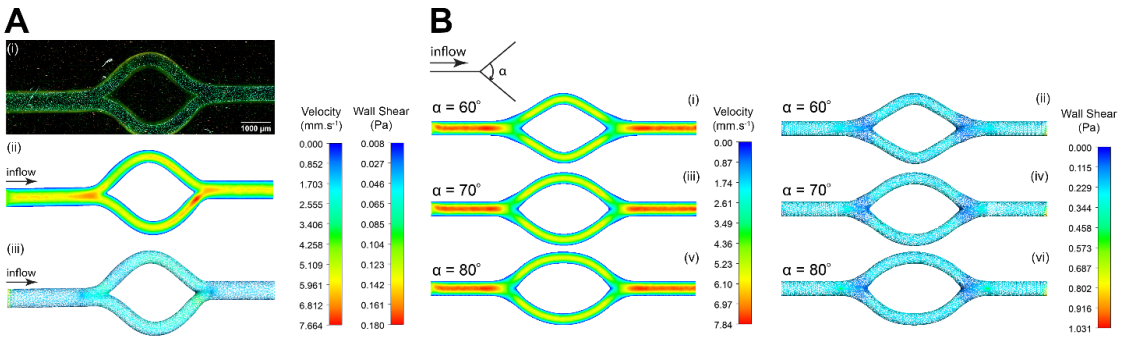

Figure 16: Characterization of endothelialized micronetworks. A) Numerical analysis of flow in embedded microvessels. Flow profile and the induced wall shear stress for perfusion of cell culture media in a 3D constructed model based on the geometrical features of endothelialized sample. The 3D model was based on data extracted using multiphoton microscopy images (not included here). **B**) Flow profiles and induced wall shear stress calculated for the perfusion of blood in parametrized 3D design of microchannels with different bifurcation angles. The confocal image of the endothelialized microchannels in Panel A was produced by co-author Dominik Schneidereit using a sample endothelialized by co-author Hatice Genc.

The influence of the bifurcation angle on three different microchannels' designs was analyzed using a numerical simulation of blood flow through the channels with different bifurcation parameters (**Figure 16**B). The comparison between different induced flow profiles showed that blood velocity at a fixed Ht of 0.45 flowing within microchannels in parent and daughter vessels was not significantly altered by increasing the bifurcation angle. The same was observed for the wall shear stress, where the daughter branches in all models experienced similar wall shear stress of about 0.22 Pa, independent of the bifurcation angle. The calculated flow profiles showed that the blood velocity within the daughter branches decreased compared to those of the parents, indicating a unique biomimetic design due to the volumetric redistribution of plasticized sacrificial scaffolds at the later stage of the print-and-fuse methodology.

3.5 Discussion

This study presents an integrated approach for fabricating 3D bulk-hydrogels with embedded biomimetically branched microvasculature inside a perfusable bioreactor system. It comprises the print-and-fuse approach to generate sacrificial templates for the microchannels that can be tuned regarding the channel diameter, with a good approximation of Murray's law to estimate the parent channel diameter based on the daughter's vessels. The integration of these scaffolds with flexible design within a customized bioreactor ensures the perfusability of the final construct. This system allows a broad range of flexibility and freedom regarding the choice of hydrogels to cast into the bioreactor.

Optimized by RSM, it was possible to fabricate sacrificial templates using MEW to form a naturally branching and interconnected microchannel network in hydrogels. During the past years, the demand to form intricate and interconnected networks mimicking the vascular system led to the development of various sacrificial templating methods. The wider accessibility, a larger user community, and technological simplicity contributed to the popularity of extrusion-based (bio)printing for sacrificial templating. Nevertheless, limitations in the resolution of the process and the spatial considerations in the fabrication of 3D structures are two challenging factors in realizing microvascular systems by this method. Compared to conventional 3D extrusion printing, MEW provides the possibility to deposit fibers in micrometer size [185]. Moreover, by introducing commercial bioprinters with MEW-enabled modules or standalone MEW printers, MEW technology is on its way to being as accessible as conventional extrusion printing. High resolution in the production of sacrificial structures [186] and tunability of the process in fabricating a wide range of dimensions are two essential advantages of MEW.

Production of low-dimension templates by MEW is especially interesting, as achieving high resolution is a critical challenge for the other methods of channel creation. Fabrication of geometrically consistent microchannels is essential in ensuring the uniform distribution of nutrients and oxygen in a large hydrogel structure. The optimization capacity of MEW through DoE adds to the flexibility of the templating design, and depending on the dimension requirements; it is possible to create predictable and defined architectures with this method.

Biocompatible templating of microchannels is mainly performed using thermoresponsive sacrificial inks [93, 94, 113, 114] or water-soluble carbohydrate-based structures [179, 180]. Pioneered by the group of J. Lewis, extensive studies on

vascularization by sacrificial inks such as pluronics or gelatin have been performed [93, 94, 113, 114]. These methods could achieve a significant level of geometrical complexities. However, critical bottlenecks include design aspects, such as the microchannels' circularity and creating overhang branching sacrificial structures. Additionally, microchannels created by carbohydrate-based templates need post-fabrication stabilization by dip- [179] or spray-coating [180] methods to control the fast dissolution rate in hydrogel matrices, resulting in complexities in the fabrication process and the formation of a barrier between endothelium and tissue.

As an alternative to current sacrificial materials, we used thermoresponsive P*cyclo*PrOx because of its intrinsic biocompatibility [187], its LCST within the physiological range [188] at 25°C, and its unique water-induced plasticity. P*cyclo*PrOx fugitive scaffolds show progressive plasticity in contact with water below the glass transition temperature. However, the rate of this behavior is slow enough to enable the casting of the hydrogel precursors without loss of the scaffold's integrity and, at the same time, quick enough to result in the fusion of adjacent fibers and formation of biomimetic branching structures during gelation of hydrogel matrix. Nevertheless, P*cyclo*PrOx shows low hygroscopicity and sensitivity to the temperature at room conditions. These properties practically extend the applicability of P*cyclo*PrOx sacrificial scaffolds compared with the traditional fugitive materials, as the latter demand special storage and handling procedures [178-180] or should be produced and manufactured just prior to embedding in the hydrogel matrix [93, 113]. P*cyclo*PrOx structures can be quickly dissolved and removed by cooling to slightly below room temperature. This provides a more convenient and cell-friendly process than other fugitive inks with LCST behavior, such as pluronics. Additionally, the distinctive feature of P*cyclo*PrOx sacrificial structures is the water-induced plasticity, a property that results in the fusion and merging of adjacent microfibers in contact with water without significant loss in shape fidelity.

Conventionally, fugitive inks such as Pluronics show an excellent recovery after the extrusion, enabling the creation of singular channels with high fidelity; however, the high elasticity results in poor merging or fusion of adjacent or overlapping strands. This behavior contributes to creating generally overlooked geometrical inaccuracies such as grooving. Other fugitive inks, such as gelatin, show improved smoothness and merging behavior in branching [93], although shape fidelity is impacted. The print-and-fuse strategy demonstrated in this study relies on a combination of the plasticity of adjacent P*cyclo*PrOx fibers, confined by the evolving elasticity of the hydrogel matrix undergoing crosslinking. A direct result of this structural development is the formation of smoothed

branching with a good degree of circularity of the lumens and in good agreement with Murray's law, independent of the size of the initial fibers. To explain why such dynamics of fusing and arrangement of filaments embedded in hydrogel matrix were observed, we considered the principle of minimum work in Murray's law, which, in its general form, describes the balance and tradeoff between the energy needed to transport a mass through the microvessels and the energy needed to maintain the mass within [189]. Assuming that such correlation applies to the systems in which the viscosity only depends on the shear [190], the driving force to form branching structures in this study could follow the same principles and be based on the balance between residual pressure due to swelling, surface energy at the interface, and the viscosity of the plasticized P*cyclo*PrOx confined by a hydrogel matrix. *In vivo*, the correlation between the diameter of parent and daughter vessels in the vascular system is such that the combined cross-section areas of daughter vessels are greater than that of the parent's [191]. The measured diameters of microchannels created in this study were above the expansion ratio of 1.0, indicating that the merging of the P*cyclo*PrOx microfibers resulted in a mass flow during the fusion process. This effect was independent of the initial diameter of fugitive scaffolds. Combining this mass flow with the smooth merging of the microfibers resulted in branching microchannels approaching the two requirements of minimum wall material and constant wall stress for microvessels [192].

To gain an understanding of the flow conditions prevailing in the 3D bifurcating microchannels exposed to perfusion by rocking, numerical flow analysis was performed. The results showed that the small diameter of microchannels in this study with no active pressure during cycling resulted in slower flow velocity within the microvessels in different regions (approximately 0.33 cm/s, with a maximum value of 0.78cm/s) as compared to the data measured *in vivo*. As an example, in human finger vessels with diameters of 800 μm to 1.8 mm, arterial blood flow velocities ranging from 4.9-19 cm/s and venous blood flow velocities at 1.5-7.1 cm/s were reported [193]. In smaller human cortical venules (below 20 μm), time-averaged flow velocity was 0.5 cm/s in non-pulsatile veins and 1.1 cm/s in pulsatile veins [194]. The average wall shear stress in different regions during each rocking half-cycle was also significantly below the values reported for the small arteries and veins [195], which is mainly associated with relatively slow perfusion velocities and also operation in atmospheric pressure. Despite these differences in flow velocities and wall shear stress, we noted the protective effect of perfusion on the ECs exposed to TNF-α stimulation, both in 2D and 3D conditions. Therefore, the slow bi-directional flow used in the present experimental setup can, to some extent, mimic the beneficial effect of laminar flow in the vasculature. Considering the unique biomimetic characteristics of this model and its straightforward assembly, the

print-and-fuse methodology promises a much broader use of vascularized 3D tissue models in the biological community, where the need for such methods is dramatically growing.

3.6 Conclusion

This study introduces an integrative and facile approach for the reproducible generation of perfusable and functionally endothelialized microvascular networks within bulk hydrogels. The described method based on thermoresponsive P*cyclo*PrOx scaffolds produced by MEW allows precise fabrication of sacrificially templated microchannels with good control over the dimensions within a hydrogel matrix. A specifically useful feature of the system is the high degree of freedom concerning the choice of hydrogel system, which makes it broadly applicable to a range of commonly used hydrogel formulations with specific biochemical features. Furthermore, the print-and-fuse approach described here allows the generation of biomimetic bifurcations in a wide range of diameters and complexities. By integrative design of the bioreactors tailored to the scaffold dimensions and characteristics, perfusable and interconnected channel networks are easily created and ready for subsequent endothelialization and microscopic assessments. By providing a functional endothelial monolayer, our model can serve as a tool to investigate cell activation and signal transduction, macromolecular or drug transport, and intracellular processes associated with changes in endothelial permeability.

The advantages of the presented design for creating microvascular networks include precise, reproducible, and adaptable biomimetic channel diameters and designs, facile removal of sacrificial structures, flexibility regarding the choice of hydrogel matrix, as well as rapid functional endothelialization. Those advantages thus make our print-and-fuse approach, which addresses some of the limitations of the current methods for creating microvascular constructs, a broadly applicable alternative platform for the generation of vascularized tissue models.

Chapter 4

Rheological Analysis of the Interplay between the Molecular Weight and Concentration of Hyaluronic Acid in Formulations of Supramolecular HA/FmocFF Hybrid Hydrogels

Chapter 4 was initially published as a note (Nadernezhad, A., Forster, L., Netti, F., Adler-Abramovich, L., Teßmar, J. and Groll, J., 2020. Rheological analysis of the interplay between the molecular weight and concentration of hyaluronic acid in formulations of supramolecular HA/FmocFF hybrid hydrogels. *Polymer Journal*, *52*(8), pp.1007-1012.), and is reproduced from reference [196], Copyright (2022) Springer Nature Limited.

This article is based on the work of the author of this thesis Ali Nadernezhad, who performed all the experiments, data evaluation, and drafting of the manuscript. Slight modifications in the structure of the article were made to increase legibility and consistency concerning the other parts of this dissertation.

4.1 Abstract

Hydrogel formulations based on self-assembling low molecular weight gelator (LMWG) peptides offer tunable physical, chemical, and biological properties, which could be tailored according to the desired application requirements. The dynamics of interactions between host polymer solution and LMWG peptides play a significant role in the alteration of the physical properties of the formulations, which is of great interest for applications such as bioprinting. In this note, we evaluated the complex relationship between molecular weight and concentration contributions in formulations based on hyaluronic acid (HA) and the self-assembling Fmoc-diphenylalanine (FmocFF) peptides. The results showed that the change in molecular weight of HA significantly alters the viscoelasticity and plastic flow of the formulations and the kinetics of self-assembly.

4.2 Introduction

Self-assembled hydrogels of low-molecular-weight gelator (LMWG) peptides offer the benefits of a highly porous fibrous network with tunable biological properties, while the reversible noncovalent interactions among the molecular building blocks enable the application of such systems as injectable hydrogels in regenerative medicine. This physically cross-linked class of biomaterials permits minimally invasive implantation strategies as an alternative to conventional methods or facilitates the use of emerging techniques such as three-dimensional (3D) bioprinting. Moreover, the well-defined chemical structure of these peptides, in contrast to that of natural biopolymers, can be tuned to introduce desirable biofunctionality. This can be achieved by controlled alteration and insertion of amino acid sequences, each serving a designed purpose, such as inducing antimicrobial effects or attachment, proliferation, and differentiation of cells [197, 198].

Incorporating LMWG peptides within a hybrid supramolecular polymer/peptide design extends the applicability of both systems, mostly by providing intended chemical functionalities within a more mechanically responsive network. To realize this idea, two main strategies—one based on the covalent linking of peptides to polymers and the other based on noncovalent interactions between both components—have been employed [199]. Both approaches inherently possess limitations and advantages regarding phase continuity, homogeneity, ease of synthesis, and the need for chemical modifications of constitutive blocks. Nevertheless, both offer synergistically enhanced mechanical properties together with engineered biofunctionality. Moreover, the application of such hybrid systems in advanced 3D bioprinting methods could potentially introduce a new class of bioinks [200], providing diverse capabilities to tune rheology and form multifunctional hydrogels.

In contrast to hydrogel formation by self-assembly of polymer-peptide conjugates, the co-assembly of peptides with biopolymers often follows a more facile approach with great flexibility to fabricate diverse biomaterials. Although such systems facilitate the formation of mechanically and biologically improved hydrogel networks, the role of the inherent physical characteristics of biopolymers on the development and progression of the self-assembly process has not been thoroughly investigated.

In this study, we used rheology as a tool to investigate the interplay between the molecular size and the amount of hyaluronic acid (HA) in supramolecular hybrid hydrogels based on HA and the self-assembling Fmoc-diphenylalanine (FmocFF). We chose HA due to its inherent bioactivity and ability to undergo further bioactivation [201]

and its previously demonstrated suitability as a bioink component [202, 203]. FmocFF dipeptide belongs to a family of LMWGs with characteristic N-terminal fluorenyl-9-methoxycarbonyl (Fmoc) group with an apparent pK_a value higher than 7.4, which makes it one of the few gelators in this class capable of forming hydrogels at physiologic pH [204, 205]. There are two main approaches in the literature for the formation of FmocFF hydrogels: pH switching and solvent switching [206]. The former results in a more homogeneous formation of the 3D fibrous network at the cost of risk of destabilization and cleavage of the Fmoc end-group under basic conditions, while the latter is often capable of producing mechanically more rigid systems but forms an inherently heterogeneous state prior to self-assembly. The solvent-switch method permits the formation of FmocFF hydrogels under physiologic conditions, a property that is of great importance in the presence of biologically active substances or living cells [207].

In a single-component dipeptide hydrogel system, several parameters, including the type of organic solvent, aqueous buffer composition, dispersion state, and agitation, could significantly influence the process of self-assembly by the solvent-switch method [206]. However, the solvent-switch-triggered self-assembly of FmocFF dipeptides in a matrix containing a biopolymer such as HA adds an extra level of complexity due to the presence of long charged polymer chains, which might interfere with network formation. A previous study by Aviv et al. demonstrated the influence of the inclusion of FmocFF peptides on the enhancement of the rigidity of HA [208]. The available literature on such hybrid systems highlights the role of charge and viscosity in the nucleation and diffusion of self-assembled fibers [209, 210]. The nucleation and diffusion of a heterogeneous phase is significantly affected by the spatial arrangement of biopolymer chains. This correlates directly with the molecular weight and concentration of the biopolymer; larger polymer chains and higher concentrations might delay the diffusion and nucleation process to a greater extent. Studies on the kinetics of self-assembly and the viscoelastic properties of the formed network in such systems are thus of great interest for the evolution of these systems into injectable or 3D bioprintable hydrogels.

4.2 Results and discussion

Based on this background, in the present study, we focused on the correlation between the characteristics of the formed network and the molecular weight and amount of HA in the supramolecular HA/FmocFF hybrid hydrogels. The insight into the counterbalance between these inherent properties is expected to serve as a foundation in the formulation of hybrid bioinks to be used in 3D bioprinting in further studies. Moreover, highlighting the role of such factors in the development of viscoelastic properties is expected to be of great importance in adjusting injectability or printability. It should be noted that the current study is more inclined towards understanding the influence of intrinsic properties of components in such supramolecular hybrid systems rather than presenting candidate formulations for the mentioned applications. For this purpose, we employed rheology to study the kinetics of network formation and the resulting viscoelastic properties in different formulations. In this way, three different molecular weights of the biopolymer and three different mass ratios were examined.

Hydrogel formulations with different mass ratios of HA:FmocFF (1:0, 3:1, 1:1, 1:3, 0:1) were prepared by diluting the stock solution of peptide in dimethyl sulfoxide (DMSO) with a solution of HA in Milli-Q ultrapure water. The total solid content of each formulation was kept constant at 5 mg.mL^{-1}. The mixtures were vortexed for 10 seconds and subsequently subjected to rheological characterization. HA with three different molecular weights was used as received. The results of SEC-MALS characterization of used HA batches are listed in **Table 9**.

Table 9 Molecular weight and correlating properties of as-received HA

Polymer	Nominal M_w[a] (kDa)	M_w[b] (kDa)	M_n[b] (kDa)	M_w/M_n[b]	R_g[b] (nm)	c^*[c] (mg.mL^{-1})
HA1	200-500	388.57	116.38	3.339	39	1.36
HA2	600-1000	765.04	475.21	1.610	56	0.90
HA3	1000-2000	984.3	736.5	1.336	85	0.33

[a] Reported values from the manufacturer based on the Ubbelohde method

[b] Determined by SEC-MALS

[c] Calculated based on the assumption of random coil chain dimensions using the equation: $c^*=M_w/[N_A(2R_g)^3]$

The calculated R_g values indicate an increasing radius of gyration with increasing molecular weights, which was already expected. The critical overlapping concentration (c^*, calculated from [211]) of each polymer showed that at the given working

concentration of 5 mg.mL^{-1} or less, the polymers would not behave as a dilute polymer solution, especially with the increasing molecular weight of HA. During the process of self-assembly, in addition to the charge-dependent interaction between polymer chains and the formed peptide fibers, the viscosity of the biopolymer solution would be a critical factor, which could hinder the process of diffusion and nucleation [209, 210]. Hence, the increasing viscosity of samples above the *c** value would further affect the kinetics of the self-assembly of the peptide phase.

The kinetics of the self-assembly and establishment of long-range interactions were rheologically studied by performing time sweeps for 60 minutes after mixing the formulations. The measurement parameters were set to be within the linear viscoelastic range as 0.1% strain at an angular frequency of 10 rad/s in a time sweep experiment and 0.1% strain, while the angular frequency changed from 0.1 to 100 rad/s in frequency sweep experiments for all the formulations (**Figure 17**). Compared to the formation of single-component FmocFF hydrogels, the process of self-assembly was hindered in the presence of HA regardless of the amount and molecular weight of the polymers (**Figure 17**A-C). However, this effect became more prominent by increasing the amount of HA, which directly translates to an increase in the concentration of polymer in each formulation. Increasing the concentration consequently resulted in increased viscosity of the polymer matrix, which hindered diffusion and nucleation. This led to slower fiber formation during the self-assembly process and the possibility of forming thinner fibers, as reported in previous studies [210].

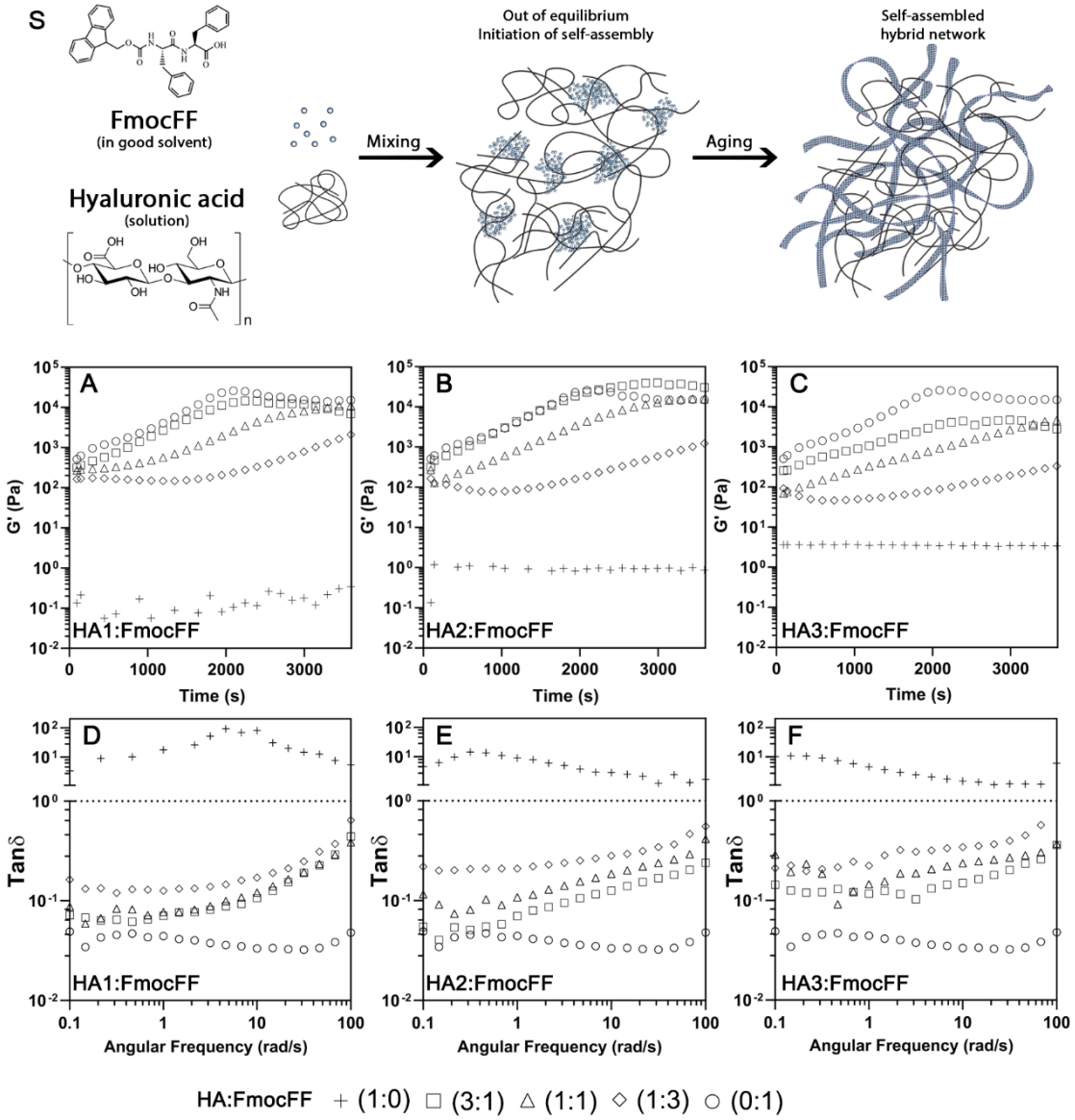

Figure 17. Schematic showing the process of self-assembly in the solvent-switch method. A-C) kinetics of self-assembly and **D-F**) the values of the loss factor over a range of frequencies in different formulations

The corresponding frequency sweep data for each type of HA (**Figure 17**D-F) confirmed that the presence of HA within the network resulted in increased viscous behavior of the hydrogels, while increasing the content of HA resulted in less stable networks over the probed frequency ranges. Evaluation of variations in the loss factor (tanδ) in each HA batch with different concentrations of the polymer showed that increasing the HA content in each category resulted in a more viscous network and a higher loss factor at almost every frequency investigated, indicating that the rheological properties of the system are controlled by the highly structured continuous peptide phase rather than the physically entangled polymer chains. Formulations of HA alone showed the characteristic behavior of polymer solutions, with relaxation times far shorter than

the experimental window. Thus, regardless of the molecular weight, the inclusion of HA shifted the viscoelastic spectrum of hydrogels towards higher frequencies and led to the weakening of the long-range interactions with increasing polymer content.

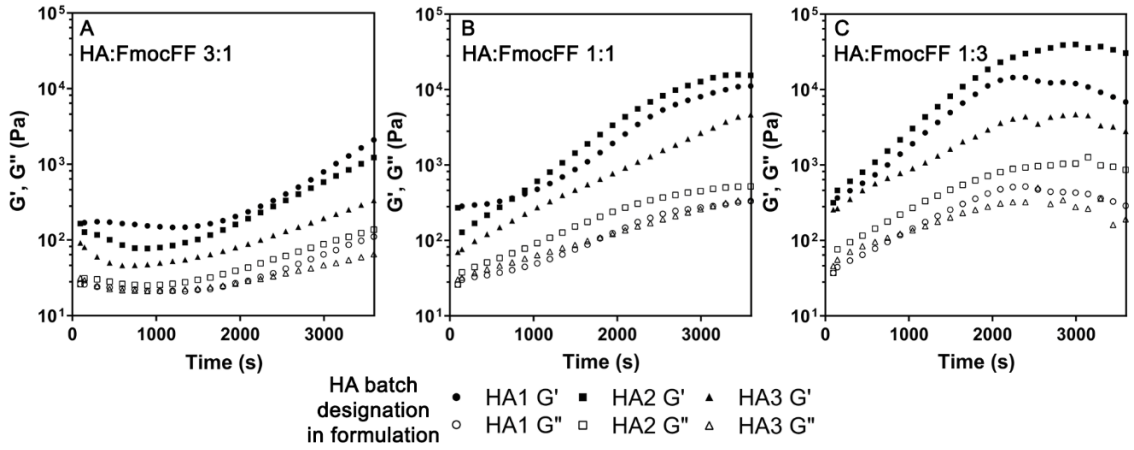

Figure 18. The evolution of the self-assembled network in formulations with different molecular weights of HA, with the HA:FmocFF ratio changed as **A**) 3:1, **B**) 1:1, and **C**) 1:3

The process of self-assembly and the subsequent development of the interconnected fibrous structure could not be solely associated with the presence of the HA phase; rather, the peptide concentration plays an essential role in the kinetics and outcome of network formation. It has been reported that decreasing the peptide content also results in slower kinetics and weaker interactions [212] by decreasing the density of the fibrous network and consequently weakening the elasticity of the system. However, the kinetics of self-assembly in a complex hybrid polymer/peptide system could not be exclusively correlated to the contribution of the peptide fraction. **Figure 18** illustrates the influence of HA molecular weight on the kinetics of self-assembly while the polymer:peptide mass ratio was kept constant. It is clear that the incorporation of extremely large polymer molecules resulted in the development of weaker interactions (lower elastic moduli) at a slower pace (slope of modulus evolution). This behavior could be correlated to two factors: the inherent viscosity of the HA matrix and the physical interactions between two components. As mentioned before, the high viscosity of HA hindered the diffusion and nucleation of the peptide phase, eventually leading to the formation of a weaker peptide network. High-molecular-weight HA, even at lower concentrations, contributed to the high viscosity due to the dense packing of coiled polymer chains above the critical overlapping concentration. Moreover, the possible secondary interactions between HA and FmocFF at the beginning and throughout the self-assembly dynamically influenced the process of fiber formation. Gong et al. argued that the formation of strong hydrogen bonds between the molecules also disrupted the movement of the Fmoc-FF molecules and their aggregation, hence also prolonging the self-assembly process [213]. A study

by Chakraborty et al. showed that the presence of positively charged chitosan chains during the self-assembly of Fmoc-RGD significantly altered the gelation kinetics due to the formation of strong electrostatic interactions [214]. Such behavior strongly suggests that the cumulative effects of greater viscosity and a higher possibility of establishing secondary interactions in HA with longer chain lengths might strongly influence the spatial arrangement of the fibrous network. Nevertheless, increasing the FmocFF content induced faster kinetics of network formation, which, in combination with moderate HA chain lengths, resulted in the formation of relatively stable long-range interactions, and the corresponding elastic moduli surpassed that of pure FmocFF hydrogels. We speculate that the combination of efficient formation of the peptide network and the stabilizing effect of HA chains by hydrogen bonding contributes to the observed reinforcement behavior.

Table 10. Flow points and relevant modulus ratio for different formulations. Data obtained through oscillatory shear strain sweeps

		Strain at flow point (%)					**$G_{crossover}/G_{0.1}$ (%)**				
HA:FmocFF ratio		1:0	3:1	1:1	1:3	0:1	1:0	3:1	1:1	1:3	0:1
	HA1	N/A	39.2	40.6	24.3	6.1	N/A	6.9	4.3	4.8	9.5
HA source	HA2	N/A	31.9	23.8	18.2	6.1	N/A	11.7	8.6	4.9	9.5
	HA3	N/A	18.1	12.8	6.5	6.1	N/A	12.2	5.1	6.0	9.5

Significant alteration of mechanical behavior in supramolecular polymer/peptide hydrogels originates from the essentially different viscoelastic properties of the two systems. Changes in the molecular weight and concentration of HA altered the ductility and plastic flow in hybrid hydrogels, the extent of which was determined through oscillatory shear strain sweeps between 0.01 and 100% strain values at an angular frequency of 10 rad/s. **Table 10** lists the storage and loss modulus crossover values in self-assembled hydrogels. Increasing the concentration of HA was reflected in the increased ductility of the hydrogels as the plastic flow started at higher shear strains, while the ratio of moduli at the flow point ($G_{crossover}$) to the elastic moduli below the limit of the linear viscoelastic range ($G_{0.1}$) was proportionally larger in hydrogels with higher HA contents. Compared with pure FmocFF hydrogels, all the hybrids showed improved ductility; however, increasing the molecular weight resulted in the development of plastic flow at lower strains and higher modulus ratios. This could further confirm the hypothesis that larger HA molecules would interfere with the process of self-assembly and that the formation of a continuous fibrous peptide network would be significantly interrupted. The current state of research in emerging fields, such as 3D bioprinting, constantly demands

the development of injectable biomaterials with suitable flow behavior. Although self-assembled Fmoc-FF hydrogels have been shown to possess excellent shear thinning properties and elasticity, the rigid nature of hydrogels from this class of peptides results in fragmentation upon extrusion. In this respect, extension of the range of ductility in supramolecular HA/FmocFF hybrids would be of great importance for application in this field of research.

4.3 Conclusion

In this note, we evaluated the relationship between the contributions of two constitutional factors in the formulation of supramolecular HA/FmocFF hybrid hydrogels and their cumulative effects on the viscoelastic behavior of such systems. The results showed that increasing the molecular weight of the polymer significantly alters the kinetics of self-assembly, generally yielding weaker hydrogel networks. Moreover, increasing the concentration of HA induces a more viscous behavior, reflecting less stability in the frequency response of the network and increased ductility by plastic flow at higher oscillatory shear stresses. Although the reported findings were explicitly analyzed for the mentioned compositions, we believe that the discussed methodologies and data could provide insight into similar systems. Our results thus show that the interplay between molecular weight and concentration in such complex systems can be utilized to tune the final properties of the desired formulations, also considering additional criteria such as biological functionalities and serving as the basis for precise adjustment of printability or injectability.

Chapter 5

Machine learning reveals a general understanding of printability in formulations based on rheology additives

Chapter 5 was published as an original research article (Nadernezhad, and Groll, J., 2022. Machine learning reveals a general understanding of printability in formulations based on rheology additives. *Advanced Science*, p.2202638.), reproduced from reference [215], which is an open access article under the terms of the Creative Commons Attribution-NonCommercial License 4.0.

This article is based on the work of the author of this thesis Ali Nadernezhad, who performed all the experiments, data evaluation, and drafting of the manuscript.

5.1 Abstract

Hydrogel ink formulations based on rheology additives are becoming increasingly popular as they enable 3D printing of non-printable but biologically relevant materials. Despite the widespread use, a generalized understanding of how these hydrogel formulations become printable is still missing, mainly due to their variety and diversity. Employing an interpretable machine learning approach allowed us to explain the process of rendering printability through bulk rheological indices with no bias towards the composition of formulations and the type of rheology additives. Based on an extensive library of rheological data and printability scores for 180 different formulations, we identified 13 critical rheological measures that describe the printability of hydrogel formulations. Using advanced statistical methods, we demonstrated that even though unique criteria to predict printability on a global scale are highly unlikely, the accretive and collaborative nature of rheological measures provides a qualitative and physically interpretable guideline for designing new printable materials.

5.2 Introduction

By introducing additive manufacturing technologies to the field of tissue engineering, and in particular 3D bioprinting, a significant expansion in the scope and applicability of tissue engineering approaches was achieved [216]. The advancement of 3D bioprinting significantly depends on development in three critical frontiers, technological innovations [88], the discovery of new functional biomaterials [139], and the deepening of our understanding of regenerative biology [217]. While addressing all the requirements for a successful regenerative approach might seem out of reach for the moment, significant resources have been dedicated to approximating this process. In this respect, engineering biomaterial inks and bioinks includes a relatively large portion of research in the field, exclusively exploring the enabling possibilities by introducing new synthetic and natural biomaterials and formulations [139].

Apart from meeting the strict biological requirements, the materials used in the 3D bioprinting approach, or in general terms, the 3D printing of soft biomaterials, need to fulfill some physical and mechanical criteria. The primary materials used as the ink for this purpose include hydrogels or polymer solutions. Traditionally, the natural biocompatible hydrogel inks failed to meet the 3D printing prerequisites, categorized primarily by lack of printability [139]. The phrase printability refers to the capability of the ink material to allow the 3D printing process to form the designed structure with acceptable shape fidelity, mechanical stability, and structural integrity [218]. Despite the extent of these measures, the printability of a hydrogel ink or polymer solution is greatly influenced by its chemistry and mechanical properties [139]. Additionally, bioprinting parameters such as flow rate, printing speed, nozzle size, process temperature, and subsequent post-printing steps could significantly influence the outcome of 3D printing [219].

Due to the biological requirements, many attempts were made to enable or enhance the printability of promising known bioactive hydrogels and polymer solutions that formerly lacked physical and mechanical needs. These mainly included chemical modifications or blending with a secondary material that could induce printability. The latter generally referred to as formulations, is becoming increasingly popular for two main reasons. Firstly, several highly efficient additives are already available that meet the biological requirements and can significantly enhance the printability of the base hydrogel or polymer solution. Secondly, and more importantly, the low cost and the straightforward know-how of creating new formulations constitute a significant advantage over developing sophisticated chemistries to induce comparable functionalities. Although this ease of processing does not replace the offerings of an

application-tailored chemical modification, the literature shows an increasing trend in applying formulations in different domains related to the 3D printing of biomaterials.

Successful engineering of a new formulation for 3D printing needs a profound understanding of the material properties on micro and macro scales. However, in an interdisciplinary field of research such as biofabrication, there are tendencies to approximate the materials' related requirements, mostly towards more established biological measures. In this context, the performance of an additive is mainly weighted by the corresponding biological response rather than quantification and analysis of the material's properties. Nevertheless, the available literature shows increasing awareness and willingness of research groups to design the formulations based on traditional and state-of-the-art physical characterization methods [139]. These mainly included the rheological characterizations of inks and finding the correlations between the printing conditions and printability of the inks.

Analysis of such systems usually requires a degree of simplification, as increasing the number of parameters and variables could quickly deteriorate the interpretability of the readout by the conventional methods. A promising tool to overcome this limitation might be the data analysis techniques employing Machine Learning (ML) principles [220]. ML methods include statistical and mathematical tools which can reveal and exploit the relationships in data and deliver complex models to describe the system. Despite the visions and hopes for applying ML tools in the scope of 3D bioprinting [221-223], there are a few reports on using ML techniques to analyze correlations in 3D bioprinting of hydrogel inks [224-227], which mainly focused on providing a metric on the predictability of the printability of similar inks, based on a few materials- and 3D printing process-related parameters. Moreover, process optimization is the central focus of the available literature on extrusion and droplet-based bioprinting techniques, as the process requirements for optimization of printability in a defined material system can be approximated with reasonably low degrees of simplifications [224-226, 228-231]. Although these studies provide a deeper insight into the dependency of printability on 3D printing process parameters by considering the performance-processing relationship, they generally overlook the fundamental material-related aspects due to the increased complexity of the problem.

A common approach in applied ML techniques is providing metrics and models that enable a system's predictability based on hidden correlations. By increasing the complexities of the models and their predictability power, the combinations and correlations of variables become more obscure, and the interpretation of the process of making a particular decision by the model becomes inherently complicated. This

problem gave rise to interpretable models, mostly recognized as explainable artificial intelligence (AI), which provide a technically equivalent but more understandable approach than black-box models for data analysis and predictions [232-234].

An intriguing question in the context of 3D bioprinting is whether explainable AI can describe the process of rendering printability in an unknown formulation and interpret it through measurable physical indices. To answer this question, we used bulk rheology indices (hereafter called *features*) in an extensive library of different formulations based on hyaluronic acid polymer solutions and three different rheology modifiers with distinct microstructural interactions. After developing a predictive ML model with high precision, we described how the knowledge from the modeled data could interpret a particular model's decision to classify a formulation and demonstrate the dependency of printability on many correlations of the features.

5.3 Materials and methods

5.3.1 Materials

Hyaluronic acid sodium salt with three different molecular weights was purchased from Carbosynth (Mw 0.6-1.0 MDa, 1.0-2.0 MDa, and 2.0-2.5 MDa; Biosynth Carbosynth, Compton, UK). Carbopol 980 NF was purchased from Lubrizol (Lubrizol Pharmaceuticals, OH, USA). Laponite XLG was purchased from BYK Additives (BYK-Chemie GmbH, Germany). N-fluorenylmethoxycarbonyl diphenylalanine (Fmoc-FF) was purchased from Bachem (Bachem, Switzerland). Dimethylsulfoxide (DMSO) was purchased from Sigma-Aldrich (Sigma-Aldrich, USA). Sodium hydroxide was purchased from Merck (Merck KGaA, Germany).

5.3.2 Formulations

HA-Carbopol (HAC), HA-Lapointe XLG (HAL), and HA-Fmoc-FF (HAF) formulations were prepared with different concentrations and starting HA molecular weights by thoroughly mixing the required amounts of HA and the respective additive's stock solutions as listed in **Table 11**. All the formulations were incubated at 4 °C for 24h after mixing. One hour of equilibrium time at room temperature was administered before each measurement.

For HAC formulations, the stock solution of Carbopole at 30 $mg.mL^{-1}$ was prepared in MilliQ water, and the pH of the solution was neutralized with the dropwise addition of 10N sodium hydroxide solution. The 100$mg.mL^{-1}$ stock solution of Fmoc-FF in anhydrous DMSO was used to prepare HAF formulations. The Fmoc-FF stock solutions were prepared freshly. To prepare HAL formulations, 55 $mg.mL^{-1}$ stock solutions of Laponite-XLG in MilliQ water were prepared. Stock solutions of HA with different concentrations and molecular weights in MilliQ water were prepared by vigorous shaking at 250 rpm at 40 °C overnight, using New Brunswick Innova 40 incubator shaker (Eppendorf, Germany).

Table 11. Different formulations based on additives used in this study

Formulation	HA: Additive	Total concentration (mg.mL^{-1})	HA M_w (MDa)
HAC	10:10 to 10:01	15	0.6-1.0
			1.0-2.0
			2.0-2.5
		30	0.6-1.0
			1.0-2.0
			2.0-2.5
HAL	10:10 to 10:01	15	0.6-1.0
			1.0-2.0
			2.0-2.5
		30	0.6-1.0
			1.0-2.0
			2.0-2.5
		45	1.0-2.0
			2.0-2.5
		50	0.6-1.0
HAF	10:10 to 10:01	5	0.6-1.0
			1.0-2.0
			2.0-2.5

5.3.3 Rheology

An Anton Paar MCR702 rheometer with a 25 mm parallel plate geometry at a 500 µm gap was used to analyze the formulations. A general protocol for rheological measurements was designed and followed for each experiment. The protocol included the following steps: 1) homogenizing the sample by constant rotation at 1.0 s^{-1} for 60 s 2) frequency sweep between 0.1-100 rad.s^{-1} at 0.1% strain 3) amplitude sweep at 10 rad.s^{-1} in logarithmic scale between 0.01-500% strain 4) 3-Interval Thixotropy Test (3ITT) at 1.0, 100, and 1.0 s^{-1} shear rates. The recovery viscosity was calculated as the percentage of the rest viscosity at 5, 10, and 30 seconds 5) 3-Interval Oscillatory Test (3IOT) at 10 rad.s^{-1} with 0.5, 50, and 0.5% strain. The recovery storage modulus was calculated as the percentage of the rest storage modulus at 5, 10, and 30 seconds. 6) shear stress sweep in rotation in linear scale from 1.0 to 100 Pa with 0.5 Pa increments 7) transient shear steps with shear rates in logarithmic scale from 0.1 to 100 s^{-1}, using a

dynamic data acquisition method. The viscosity at each discrete shear rate value was monitored every 100 ms, and the corresponding viscosity value was reported if a 0.5% tolerance threshold over 10 observed values was met. A viscosity vs. shear rate curve was generated using the acquired data, followed by fitting with the Carreau-Yasuda model.

A rest period between each measurement step was implemented to recover the sample after deformation. Samples were gently loaded from standard 5 mL syringes on the lower plate without any needles attached for each experiment.

In order to benchmark the change in rheological properties induced by the additives, the equivalent HA solution of each formulation with the relevant concentration and molecular weight was tested with the same general protocol.

5.3.4 Printability assessment

The induced printability of each formulation was quantified based on the ability to resolve 2D mesh patterns with varying intra-fiber distances (**Figure 18**). Printing was performed using the RegenHU Discovery bioprinter (RegenHU, Switzerland). The hydrogels were loaded in 3 mL Luer lock syringe barrels (Nordson EFD, USA), equipped with a blunt G22 general-purpose dispensing tip (inner diameter 410 µm, Nordson EFD, USA). For each formulation, the minimum air pressure of the pneumatic dispensing unit, which resulted in constant flow, was used. The path plans and the printing speed for each formulation were created using an in-house developed VisualBasic program created in VisualStudio (Microsoft, USA). The layer height for printing was set to 2/3 of the nozzle diameter to ensure sufficient contact during printing. The printing speed for each sample was automatically calculated based on the extruded mass during 20 seconds of extrusion with the set pressure. The images of 3 printed grids were acquired 3 minutes after printing and were further quantified using Fiji [181]. The printability index was calculated as the ratio between the resolved and expected area of the grid, weighed by the difficulty index of resolving a specific mesh area (**Figure 19**). Larger grid areas of the designed path plan were penalized by a lower weight. A ratio above 0.33 was considered printable.

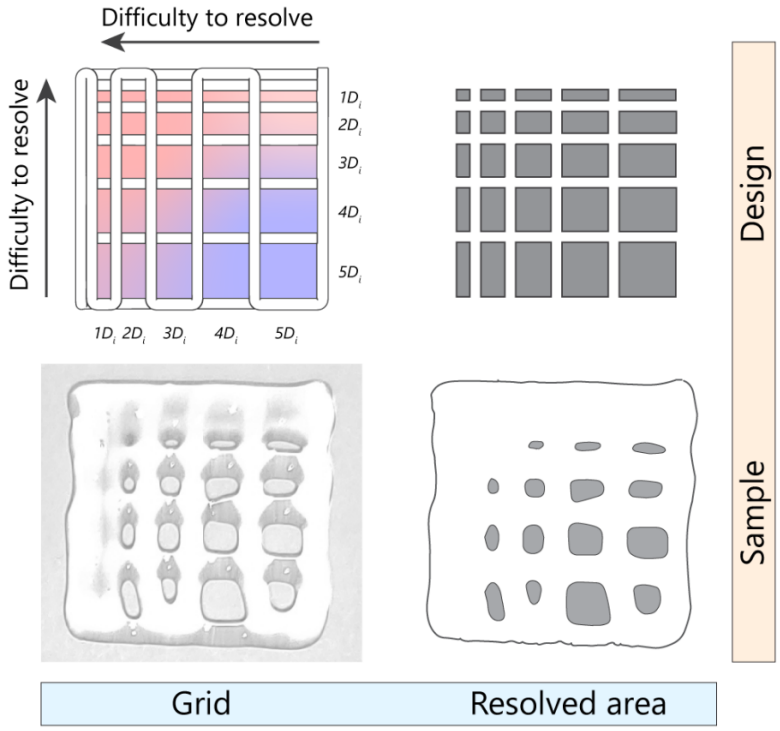

Figure 18. A schematic and experimental representation of the metric used in this study to quantify printability. Top-left) a 2-layer grid design with varying fiber spacing was used to assess the printability of the formulations. The fiber spacing was increased by increments of inner nozzle diameter (D_i = 410μm). Bottom-left) an image of an actual sample printed according to the grid design. Top-right) The resolved area of design is used for benchmarking printability. Bottom-right) The segmented image of a printed formulation is used to calculate the percentage of resolved area.

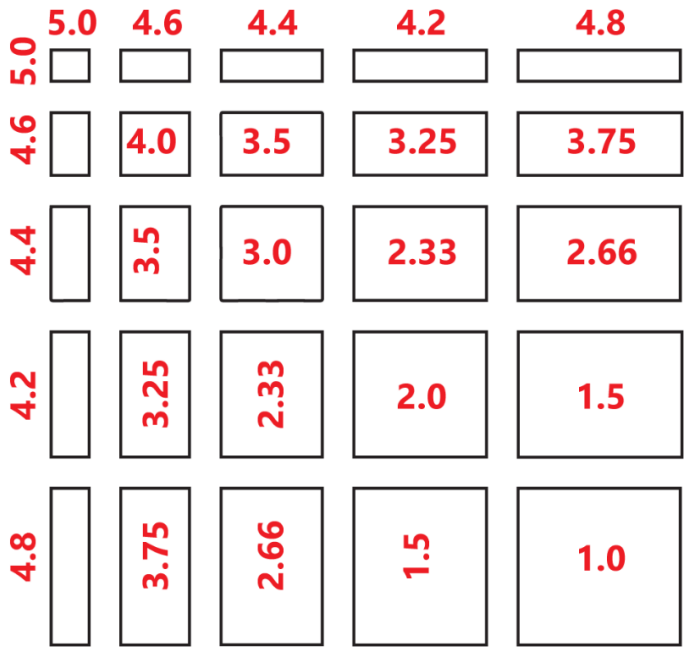

Figure 19. The weighting approach was used to penalize the easy-to-resolve areas of the grid. The numbers next to or inside each grid show the multiplication factor.

5.3.5 Machine learning algorithm

Data generation

Rheological data and printing conditions related to each formulation were processed according to the template provided in **Table 12**. To avoid skewness of the dataset due to possible measurement errors at the high and low ends of the frequency and strain sweeps, a clipped range of data was used by limiting the angular frequency and oscillatory strain values between 1.0-10 rad.sec^{-1} and 0.1-100%, respectively. Using a MATLAB script, the generated tabulated data were consolidated into a randomly distributed dataset with 65 features per formulation (MathWorks, USA).

Table 12. List of rheological data used for further processing and generation of features

Test type	Measured quantities	The range used for further processing
Frequency sweep	Storage modulus (G)	Angular frequency: 1.0-10 rad/s
	Damping factor (DF)	Angular frequency: 1.0-10 rad/s
Amplitude sweep	Storage modulus (G)	Oscillatory strain: 0.1-100%
	Damping factor (DF)	Oscillatory strain: 0.1-100%
3-Interval Thixotropy Test (3ITT)	The percentage recovery of viscosity during the third interval	Time: 5, 10, and 30 seconds
3-Interval Oscillatory Test (TIOT)	The percentage recovery of storage modulus during the third interval	Time: 5, 10, and 30 seconds
Shear stress sweep	Viscosity	shear stress: 1-100 Pa
Transient shear steps	Viscosity	Shear rate steps: 0.1-100 s^{-1}

ML model and selection and evaluation of relevant features

A classification ML model based on Random Forest (RF) algorithm was implemented in Python using the scikit-learn package [235]. The RF classifier is an ensemble non-parametric model based on many decision trees. In order to build an ML model including the features with relevant and statistically meaningful contributions, a Python implementation of the Boruta all-relevant feature selection method [236] was used

(BorutaPy). No data was rejected during training to compensate for the dataset imbalance (positive sample population ~14%). Instead, iterative randomization steps were employed to compensate for the imbalance in the dataset. Initially, a subset of the dataset with a balance of 75:25 for not-Printable: Printable classes was randomly chosen from the original dataset. An RF classifier was trained with the subset, and if the F-score (**Equation 3**) of the trained model on the test portion of the subset was above 0.80, a Boruta feature screening was subsequently applied. This process was iterated 10000 times, and the most-occurring relevant features were selected from the accumulated responses of the Boruta feature screening algorithm. The F-score was calculated by the following equation:

$$\mathrm{F-score} = \frac{TP}{TP+\frac{1}{2}(FP+FN)} \qquad \textbf{(Equation 3)}$$

where TP, FP, and FN are the classifier's true-positive, false-positive, and false-negative predictions, respectively.

Shapley values were used as the principal way of describing features' contributions in the implemented ML model. For this purpose, Shapley Additive Explanations (SHAP) were employed to explain features' correlations, interactions, and contributions to predictions [237]. SHAP values were obtained and accumulated through n-repeated k-fold cross-validation of the trained ML model on random splits of the dataset (n=20, k=5).

5.4 Results

5.4.1 Production of data with minimized bias

Figure 20 shows an overview of the multiple steps taken in this study to identify and explain the contributing factors in enabling printability by adding rheology modifiers into a not-printable polymer solution. In the first stage, three different rheology modifiers with significantly different physical properties were selected to alter the rheology and printability of plain HA solutions with three different molecular weights at various additive ratios (**Table 11**). In addition to the interactions between HA molecules and the additives, each rheology modifier had unique interaction mechanisms to alter the viscoelasticity of the final formulation: colloidal and granular interactions of Carbopol microgels, formation of a secondary network by electrostatic interactions between Laponite nanodiscs, and entanglement and network formation of one-dimensional self-assembled Fmoc-FF fibrils. The information regarding the polymer: additive ratio, the additives' type, and the initial polymer's molecular weight were not revealed to the ML algorithm at the later stages to avoid creating any bias throughout the analysis and potentially decreasing the universality of the outcome.

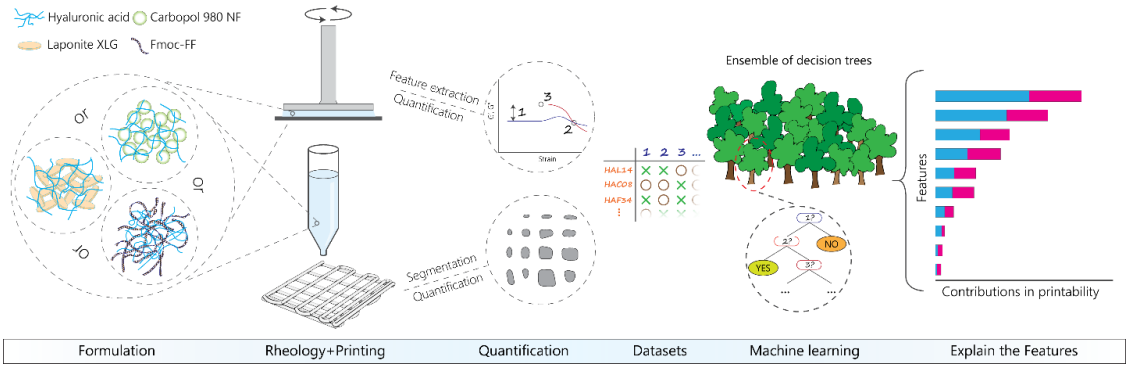

Figure 20. A demonstration of the multi-steps taken in this study to explain the printability. The flow of this study is depicted from left to right in the figure. First, the formulations based on different additives and starting HA solutions were prepared. In the second step, rheological characterizations and printing experiments were performed. The quantification step involved the extraction of various rheological features and quantitative analysis of the printability of formulations. In the next step, datasets based on combining all acquired features and printability scores were fabricated. By using the generated datasets, a random forest ML algorithm was trained. In the final step, a post-analysis of the obtained model revealed the correlations between data and the influence on making a decision by the model.

A multi-step rheological testing protocol was designed to acquire information on the viscoelasticity and flow properties of samples holistically. The complete list of rheological data obtained from each test step and the extracted ranges are provided in **Table 12**. Notable, the apparent yield behavior of formulations was identified by whether a peak in the viscosity-shear stress plot was observed, and if so, the corresponding value

was recorded. From the physical point of view, this peak and its value corresponding to the buildup of resistance against the flow on a macroscopic scale. The testing protocol was aimed to maximize the obtained information with minimum complexities. Especially, creep-related tests were avoided since the preliminary experiments (data not included) for optimization of protocol showed the sensitivity of creep tests towards not-printable formulations, potentially resulting in a bias in the analysis.

The printing experiments were conducted considering that no pure HA solution was printable. The printing experiments were performed considering the volumetric flow of each formulation during printing. A recent study by Fisch et al. [238] demonstrated the sensitivity and susceptibility of pneumatic-driven extrusion systems to over-or under-extrusion if the volumetric flow and the cartesian translation feedrate are mismatched. For this reason, each formulation was printed at a unique combination of applied pressure and feedrate; the latter was derived automatically based on the extruded mass of the formulation during a given time. Two features of the printing process, the ability to form a filament and the proportionality of the volumetric flow to printing pressure, were recorded as the characteristics of the printing process per formulation.

The designed path for the printability assessment included a 2-layered rectangular mesh with a directional increase in fiber spacing based on increments of the inner diameter of the nozzle (D_i) (**Figure 18**). The 3D assessments of printability were deliberately avoided since criteria such as general 3D shape fidelity and fiber sagging supposably demand a certain extent of viscoelasticity, which could interfere with the objectives of this study in the unbiased evaluation of induced printability by rheology additives [141]. Based on our preliminary screening experiments, a weighting approach to penalizing the easy-to-resolve areas was employed (**Figure 19**). In general, the induced printability in different formulations was not significant, as only about 14% of the formulations could resolve more than 33% of the designed area. We speculate that several factors contributed to such behavior. Among them, the concentration restrictions (maximum concentration of additives was 2.5 wt./v% in a 1:1 additive:polymer ratio) imposed by the experimental design and potential biological requirements, and the wide range of physical properties of initial polymer solutions (resulted by variation of concentration and molecular weight) would play the critical role.

The printing parameters could significantly influence printability [239]. This influence is more evident in resolving geometrical features for which an abrupt change in the printing process, such as a change in direction, is expected [238]. In addition, other factors, such as extrusion rate and substrate interactions, potentially influence the spreading and fidelity of extruded filaments. As described earlier, the printing speed

adjustment based on the volumetric flow was employed to eliminate the factor of over- and under-extrusion, while the same substrate was used to print all the formulations. However, to avoid complexities caused by pressure-dependent extrusion delay, no changes in the printing speed at turning points were implemented. This phenomenon resulted in the underscoring of weakly printable formulations, as revealed by the review of the raw quantitative analysis of individual printing experiments. However, in an equally conditioned set of experiments, this could be considered a result of the lack of meeting the viscoelasticity requirements for extrusion printing.

After acquiring the rheological and printing data, the dataset was generated for further analysis by considering two feature types. Concretely, some aspects of the raw data from rheological experiments were used as the *primary* features. To include the additive nature of the rheology modifiers in the analysis, most of the extracted primary features of formulations were individually divided by the corresponding values of the respective HA solutions of different concentrations and molecular weights to include the proportion of change in further analysis.

The second type included *combinatory* features. The combinatory features were generated based on combining some aspects of the data collected during experiments, and as a principle, all the primary and combinatory features were selected based on physically explainable factors rather than abstract quantities. The details of the complete list of features are provided in **Table 13**.

Table 13. List of full features and their corresponding descriptions

Feature	Description	Proportioned[1]
logical_FS_CO	If a crossover in frequency sweep was observed	NA
FS_DF_6	Damping factor at 1.0 rad/s angular frequency	Yes
FS_DF_5	Damping factor at 1.58 rad/s angular frequency	Yes
FS_DF_4	Damping factor at 2.51 rad/s angular frequency	Yes
FS_DF_3	Damping factor at 3.98 rad/s angular frequency	Yes
FS_DF_2	Damping factor at 6.31 rad/s angular frequency	Yes
FS_DF_1	Damping factor at 10.0 rad/s angular frequency	Yes
ratio_FS_DF@1.0/FS_DF@10	Proportioned ratio between Damping factor at 1.0 rad/s to DF at 10.0 rad/s	NA
logical_SS_CO	If a crossover in Amplitude sweep was observed	NA
SS_G_1	Storage modulus at 0.1% strain	Yes
SS_G_2	Storage modulus at 0.148% strain	Yes
SS_G_3	Storage modulus at 0.217% strain	Yes
SS_G_4	Storage modulus at 0.318% strain	Yes
SS_G_5	Storage modulus at 0.467% strain	Yes
SS_G_6	Storage modulus at 0.685% strain	Yes

The table continues on the next page

From the previous page

Feature	Description	Proportioned[1]
SS_G_7	Storage modulus at 1.0% strain	Yes
SS_G_8	Storage modulus at 1.48% strain	Yes
SS_G_9	Storage modulus at 2.17% strain	Yes
SS_G_10	Storage modulus at 3.18% strain	Yes
SS_G_11	Storage modulus at 4.67% strain	Yes
SS_G_12	Storage modulus at 6.85% strain	Yes
SS_G_13	Storage modulus at 10.0% strain	Yes
SS_G_14	Storage modulus at 14.8% strain	Yes
SS_G_15	Storage modulus at 21.7% strain	Yes
SS_G_16	Storage modulus at 31.8% strain	Yes
SS_G_17	Storage modulus at 46.6% strain	Yes
SS_G_18	Storage modulus at 68.5% strain	Yes
SS_G_19	Storage modulus at 100.0% strain	Yes
SS_DF_1	Damping factor at 0.1% strain	Yes
SS_DF_2	Damping factor at 0.148% strain	Yes
SS_DF_3	Damping factor at 0.217% strain	Yes

The table continues on the next page

From the previous page

Feature	Description	Proportioned[1]
SS_DF_4	Damping factor at 0.318% strain	Yes
SS_DF_5	Damping factor at 0.467% strain	Yes
SS_DF_6	Damping factor at 0.685% strain	Yes
SS_DF_7	Damping factor at 1.0% strain	Yes
SS_DF_8	Damping factor at 1.48% strain	Yes
SS_DF_9	Damping factor at 2.17% strain	Yes
SS_DF_10	Damping factor at 3.18% strain	Yes
SS_DF_11	Damping factor at 4.67% strain	Yes
SS_DF_12	Damping factor at 6.85% strain	Yes
SS_DF_13	Damping factor at 10.0% strain	Yes
SS_DF_14	Damping factor at 14.8% strain	Yes
SS_DF_15	Damping factor at 21.7% strain	Yes
SS_DF_16	Damping factor at 31.8% strain	Yes
SS_DF_17	Damping factor at 46.6% strain	Yes
SS_DF_18	Damping factor at 68.5% strain	Yes
SS_DF_19	Damping factor at 100.0% strain	Yes

The table continues on the next page

From the previous page

Feature	Description	Proportioned[1]
SS_LVER_strain	Strain at the limit of the linear viscoelastic range	No
SS_LVER_G	Storage modulus at the limit of the viscoelastic range	Yes
SS_CO_strain	Crossover strain in Amplitude sweep	No
ratio_SS_CO_strain/SS_LVER_strain	The ratio between crossover strain and the strain at the limit of viscoelastic	NA
ratio_SS_CO_G/SS_G@0.1	The ratio between storage modulus at crossover and proportioned storage modulus at 0.1% strain	NA
ratio_SS_CO_G/SS_LVER_G	The proportioned ratio between storage modulus at crossover and storage modulus at the limit of the viscoelastic range	NA
logical_FC_yield	If a peak viscosity in the stress sweep test was observed	NA
FC_yield_Eta	Peak viscosity in the stress sweep test	No
FC_CY_Eta0	Zero-shear viscosity from the Carreau-Yasuda model	Yes
FC_CY_Lambda	Consistency index (λ) from the Carreau-Yasuda model	No
3ITT_Re_5s	Recovery of viscosity in 3ITT after 5 seconds	Yes

The table continues on the next page

From the previous page

Feature	Description	Proportioned[1]
3ITT_Re_10s	Recovery of viscosity in 3ITT after 10 seconds	Yes
3ITT_Re_30s	Recovery of viscosity in 3ITT after 30 seconds	Yes
3IOT_Re_5s	Recovery of storage modulus in 3IOT after 5 seconds	Yes
3IOT_Re_10s	Recovery of storage modulus in 3IOT after 10 seconds	Yes
3IOT_Re_30s	Recovery of storage modulus in 3IOT after 30 seconds	Yes
Print_Flow	Proportionality index of the extruded volume to the applied pressure	No
logical_Print_Filament	If a filament was formed during extrusion (no filament, broken filament, yes)	NA

[1] Proportioned ratio was calculated by dividing the respected value by that of the corresponding HA solution with the same molecular weight and concentration (Yes, No, NA=Not Applicable)

5.4.2 Selection of relevant features influencing printability

The data from rheological and printability experiments of all the formulations were prepared and consolidated into a single structured data frame. An intuitive nomenclature system was devised to identify the different features in the dataset. The complete list of nomenclature used to address different elements in the dataset is provided in **Table 13**. To increase the legibility of the manuscript, **Scheme 2** provides the guideline for interpreting the coded nomenclatures.

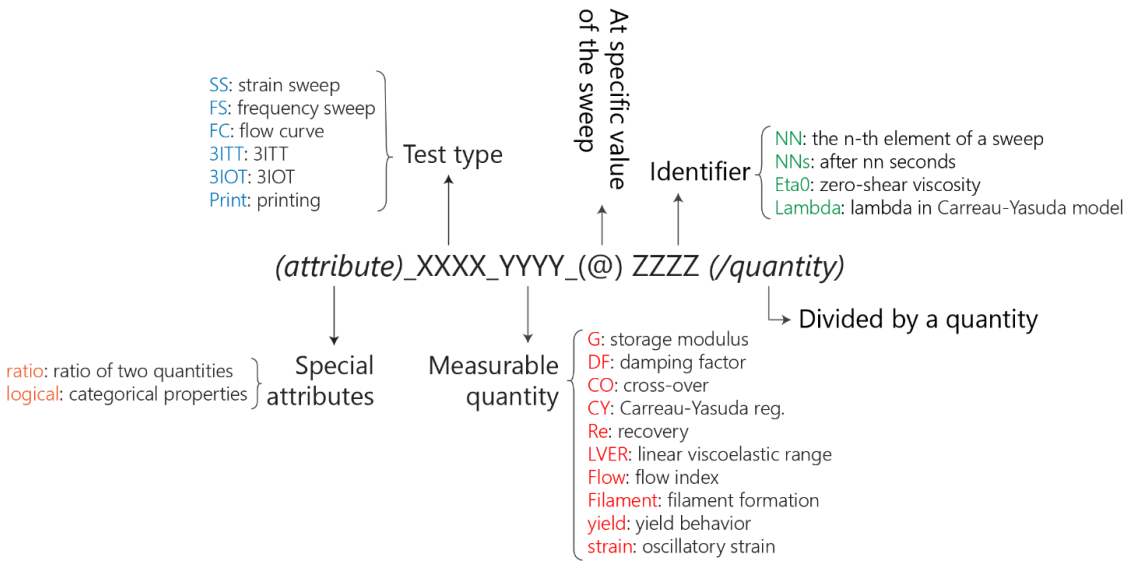

Scheme 2. Reference for the nomenclature used to address different features in this study.

Spearman's correlation analysis of the raw data showed significant dependencies between features (**Figure 21**). By implementing the statistically robust algorithm of Boruta feature selection [236], the original features were refined to those significantly contributing to printability prediction with a high F-score of a trained RF model. The performance and relative metrics for the RF model are provided in Supporting Information. Boruta algorithm identifies the importance of the features for constructing the ML model based on the performance of a randomized version of the features through many iterations. Eventually, the statistically impactful features are selected from the top 0.5% of the binomial distribution of the iterations. This procedure resulted that, among the initial 65 features, only 13 were identified as having a significant influence on the predictability of the RF model. To explore and understand the existing correlations between these essential features, the Spearman rank-order correlation matrix and the linkage based on hierarchical cluster analysis of Spearman's correlations are demonstrated in **Figure 22**. This analysis showed two main clusters of features (as indicated by different colors of the dendrogram) with distinct linkage distances from each other.

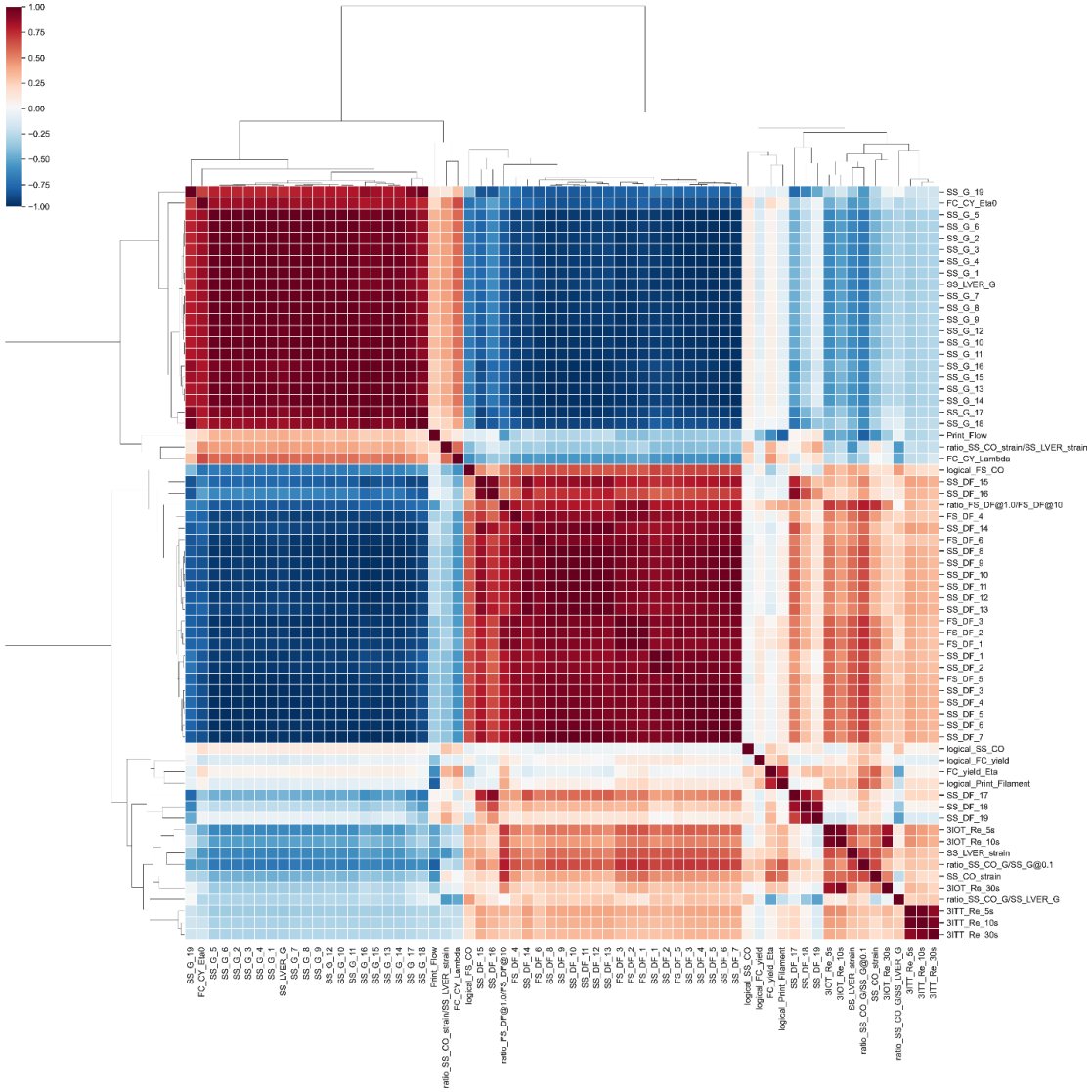

Figure 21. The results of Spearman's correlation analysis. A value of 1 or -1 denotes high correlation, and the direction of association depends on the sign of the correlation coefficient.

These two clusters include features that could be physically interpreted as 1) describing the ease of creating flow and its plasticity (orange leaves in **Figure 22**) and 2) describing the homogeneity of the flow and the viscoelasticity of the formulation before and after the flow (green leaves in **Figure 22**).

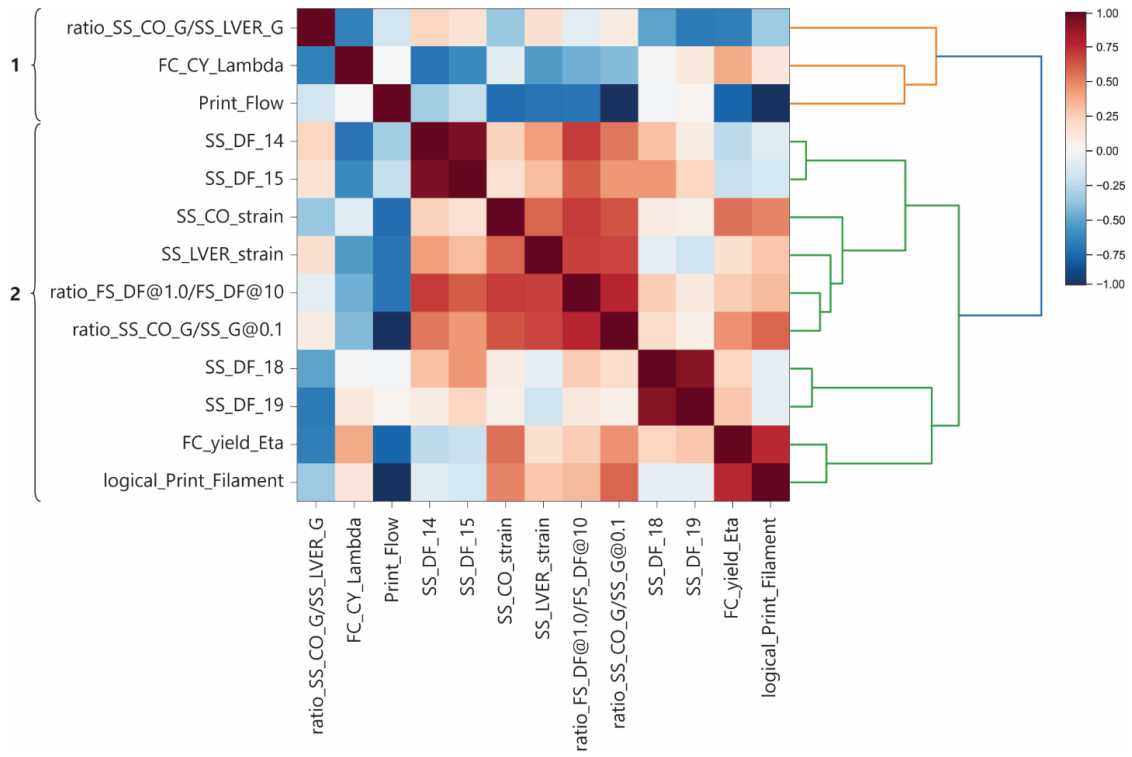

Figure 22. The dendrogram shows the Spearman rank-order correlation matrix and the linkage according to hierarchical cluster analysis of Spearman's correlations. The numbers on the left identified two clusters. A value of 1 or -1 in the correlation matrix denotes high correlations, and the direction of association depends on the sign of the correlation coefficient.

The first cluster involves the ratio between storage modulus at the flow point and the limit of the linear viscoelastic range, the consistency index determined by the Carreau-Yasuda model, and the proportionality index of the flow during printing. The first feature describes the plasticity of the formulation before the flow, while the consistency index indicates the necessary shear rate for the transition from Newtonian to non-Newtonian flow regime. The flow proportionality index reflects the requirements for maintaining the formulation's flow during the extrusion through a fine nozzle. The information from these three features complements each other, describing correlations between the ease of creating the flow in a formulation and the force requirements to maintain the flow during the extrusion.

The second cluster includes two primary nodes, one describing the viscoelasticity of the formulations, and the other includes features related to the resistance against initiating the flow and the extent of viscous deformation afterward. On the one hand, the viscoelasticity of the formulation prior to flow was critical in predicting printability. The dominancy of the viscous portion of deformation prior to flow, determined by the damping factors at moderate shear strains (14.8 and 21.7%), was correlated with the required strain to initiate the flow, the extent of linear viscoelasticity, the extent of stability of the interactions by changing the frequency of deformation, and the energy required to induce

the flow of formulation with consideration of the elasticity of the starting HA solution (ratio between storage modulus at low strain and flow point multiplied by the storage modulus of corresponding HA at 0.1% strain).

On the other hand, the closely correlated damping factors at high shear strains (68.5 and 100%) highlight the contributions of the viscous nature of the formulation in its printability, which is linked to the likelihood of filament formation during the extrusion and the yield viscosity of the formulations.

Although the correlative analysis showed the contribution of different rheological characteristics of the formulations in creating printability, their extent is yet to be determined.

5.4.3 Global and local explanation of printability

Despite identifying the important features that contributed to printability prediction, the extent of the contributions is unknown. This is a typical characteristic of models generated with most ML methods, as interpreting the predictive model's output is tedious, especially by increasing the complexities in non-linear models. Shapley additive explanations are a powerful tool for interpreting the prediction by ML models [234]. SHAP has a solid theoretical foundation in game theory and can provide contrastive explanations and analyze the model's output locally and globally.

The extent of the contribution of different features in the predicted printability of formulations is demonstrated in **Figure 23**A. The average SHAP value quantifies the impact of each feature on the model output by interpreting the average expected contribution of the feature after all the possible combinations of other features are considered.

The SHAP feature importance plot shows that the most important features in the global scale for printability prediction included the yield viscosity and the storage modulus ratio at the flow point to that of the limit of the viscoelastic range (plasticity of the formulation before flow). Although the impact of the other features on the model's output is to a lesser degree, their contributions to the model's accuracy can not be disregarded since the SHAP analysis was performed on all the relevant features selected by the Boruta algorithm.

The average SHAP value provides information about the contribution of the features on a global scale. However, on a local scale, the evaluation of individual observations and the corresponding SHAP value demonstrates how each feature contributed to predicting a printable formulation experimentally (**Figure 23**B). A careful analysis of

Figure 23B indicates that different features contributed in different directions to enabling printability.

For instance, a high yield viscosity of the formulation resulted in a higher printability score, while lower plasticity prior to the flow contributed to more printable formulations. The lack of filament formation ability negatively influenced the printability of the formulations. Additionally, formulations with a lower flow proportionality index were statistically more susceptible to being identified as printable, meaning that either a lesser extrudate mass at constant pressure or a larger force to extrude the same mass of the ink determines a printable formulation. This feature directly corresponds to the microstructural interactions of the formulation; the stronger the interaction, the better resistance to deformation and better printability. Moreover, moderate to high values of the consistency index in the Carreau-Yasuda model correspond to printable formulations, translating to a transition to a shear thinning behavior at moderate to low shear rates.

A higher ratio of storage modulus at the flow point to the one at 0.1% strain (proportional to the starting HA's storage modulus) resulted in a higher probability of printability, meaning that the higher elasticity of starting HA solution could contribute to more printability of the formulation. Similarly, a higher ratio between the damping factor at low and high deformation frequencies contributed more to the printability of the formulation. From the physical point of view, this meant that lesser variation of the damping factor in a range of frequencies results in a higher chance of printability. In other words, more stability of the interactions at the moderate to the low portion of the frequency spectrum results in better printability.

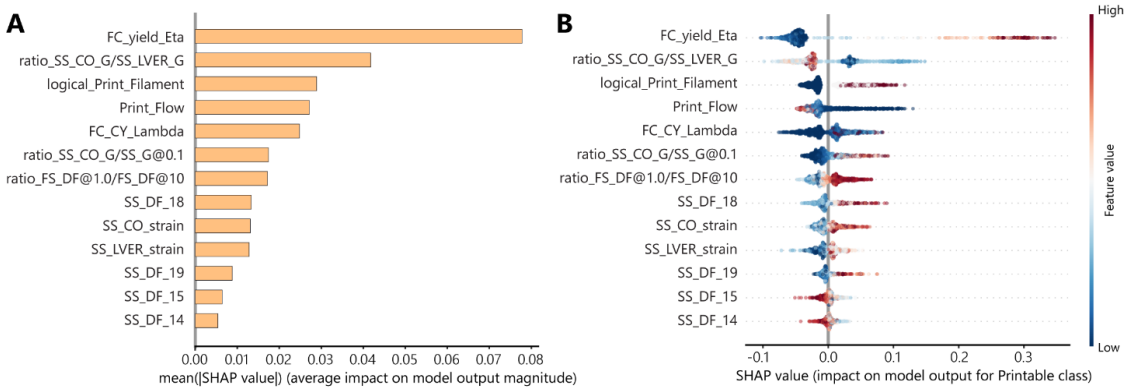

Figure 23. SHAP values of different features show their contributions to the model output on two scales. A) on a global scale, the mean SHAP value represents the feature's average impact on the predictions made by the model. **B**) on a local scale, the rank-ordered features explain the margin output of the model, which is the change in the printability of formulations. The plot also shows the range of influence over the dataset. The color shows how the change in the value of a feature affects the change in the printability prediction.

More pronounced viscous behavior after the flow (at shear strains of 68.5 and 100%) contributed more to the printability of formulations. Moreover, the higher flow strain also resulted in better printability of the formulations, and similarly, formulations with moderate to high levels of the limit of linear viscoelastic range showed more printability. Finally, the dominant elastic behavior at lower shear strains (14.8 and 21.7%) contributed positively to printability, indicating that the dominancy of elastic behavior at low strain values positively influences the formulations' printability.

The outcome of SHAP feature importance in a complex model is inevitably context-dependent, meaning that a contrastive SHAP statement might not hold for all experimental conditions. The dependency of the model's outcome on every single feature, and eventually on their combinations, can show the relationship between the features and the target. In order to clarify the validity of the SHAP analysis, we performed the partial dependence (PD) analysis to show the average marginal effects of features on the outcome of the printability assessment (**Figure 24** and **Figure 25**). Although the assumption of independence for highly correlated features (such as damping factors at low or high strain values) is not necessarily valid, however, the outcome of PD analysis showed that with some degrees of simplifications, the extent of dependency of the output on the features is likely to increase by increasing the feature importance determined by SHAP.

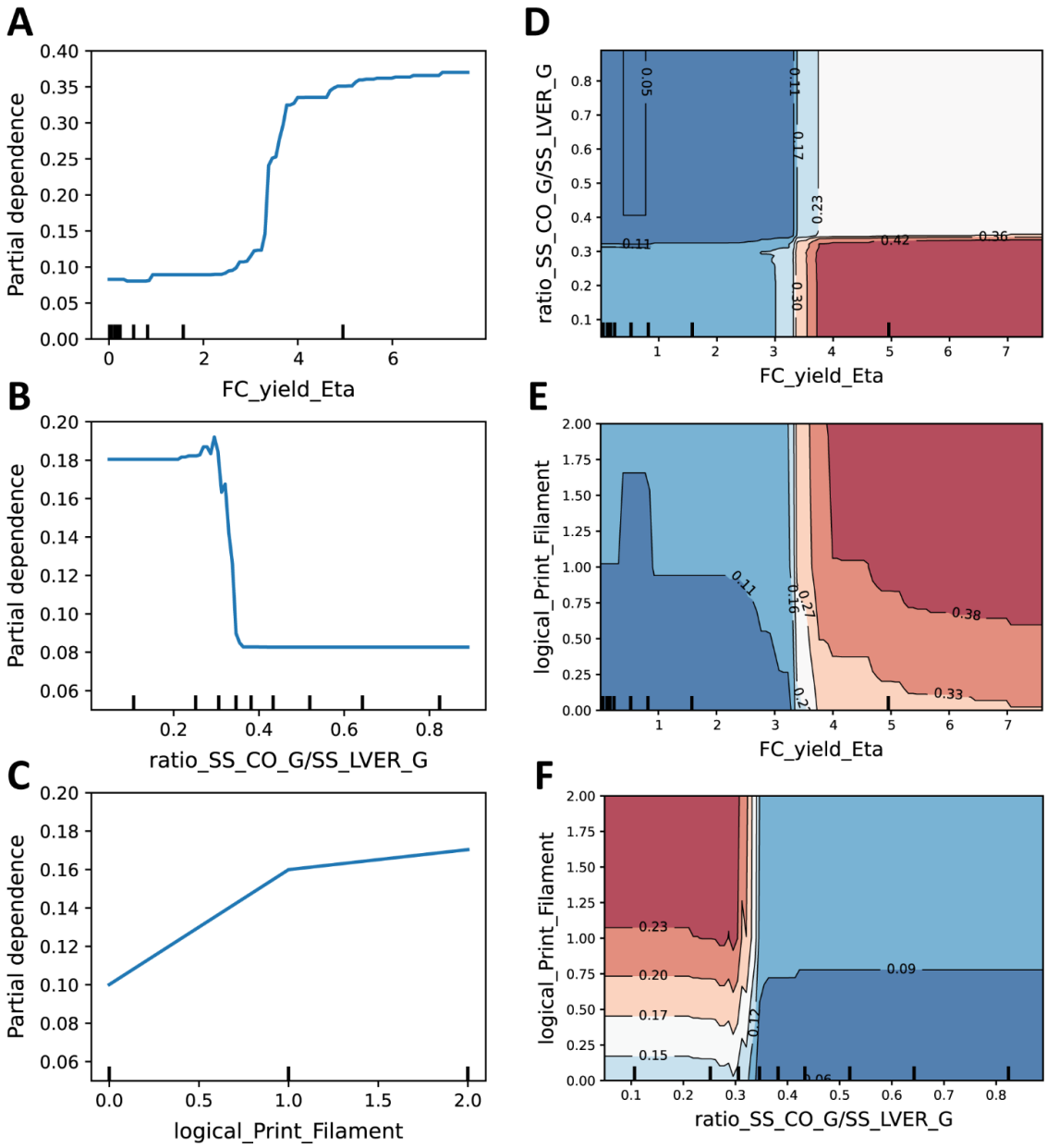

Figure 24. Partial dependence plots of the three most important features on the predicted printability. A-C) dependence of the predicted printability on each feature's value. **D-F**) the two-way PDPs showing the dependence of predicted printability on the joint values of three important features.

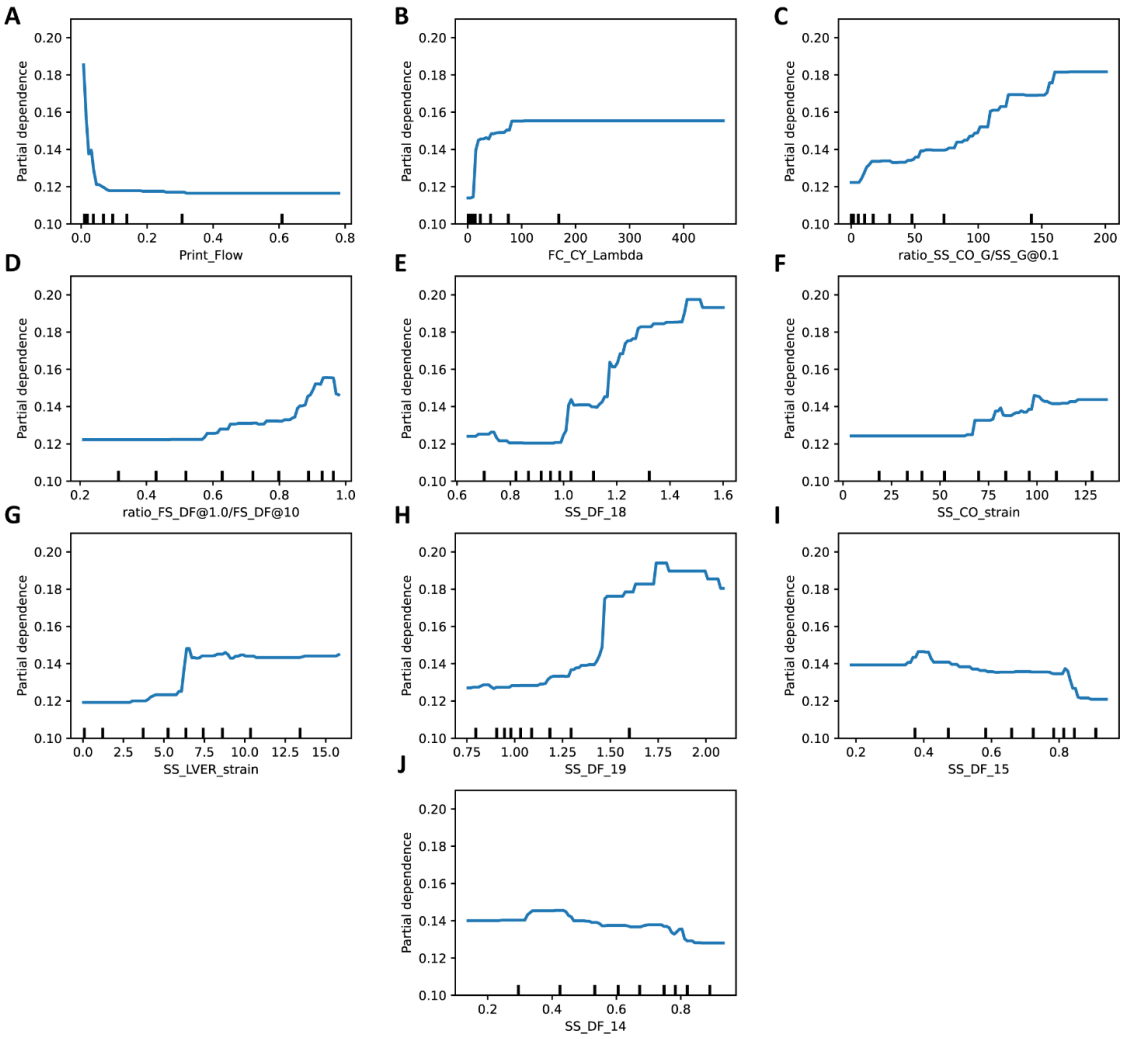

Figure 25. Partial dependence plots show predicted printability's dependency on each feature's value. Features were ranked from **A** to **J** based on their importance determined by SHAP analysis.

Evaluation of decision rules for every decision tree of the random forest algorithm revealed that by increasing the importance of a feature, a narrower range for the feature's threshold value could be identified (**Figure 26**). As a result, only a few features could be used to determine relatively more precise boundaries for distinguishing a printable formulation from a non-printable one. In contrast, the major part of the features contributed to determining printability across a wide range of values. This was a significant finding, as it hints towards the collaborative role of rheological characteristics of a formulation in rendering printability rather than introducing a dominant single measure to classify formulations.

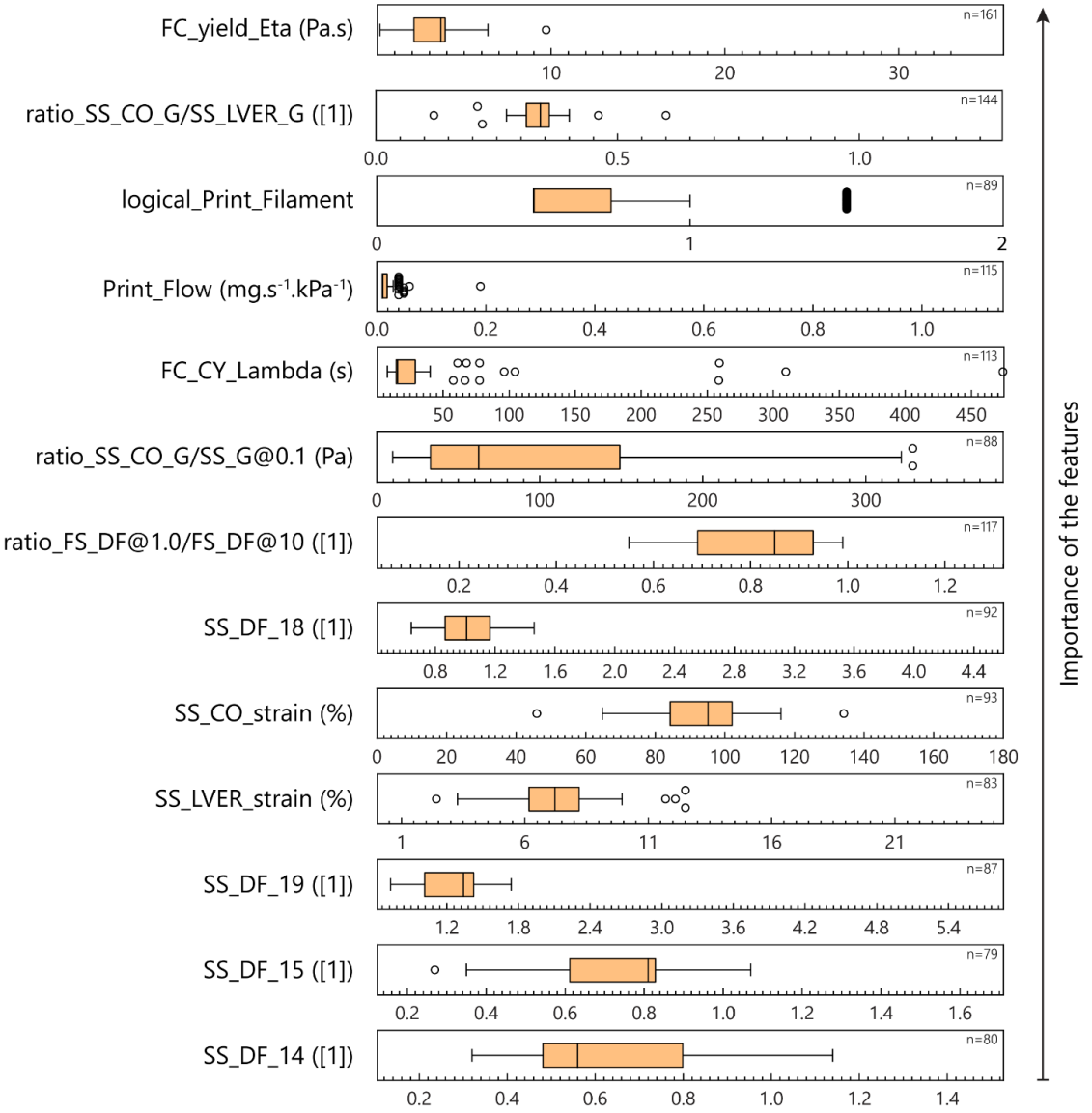

Figure 26. Decision rules in the random forest algorithm are shown by box-and-whisker plots (Tukey, outliers in open circles) across the full range of each feature. The importance of the features increased from the bottom to the top of the graph. The number of total splitting nodes based on each feature is indicated by *n*.

The collaborative contributions of a formulation's rheological characteristics toward printability are better demonstrated within the observations made by the algorithm (**Figure 27**A, B). **Figure 27**A shows the contributions of all the rheological features in a randomly picked observation by the model, which was later identified as a printable formulation. As expected, the most impactful features contributed significantly toward printability. However, the minor contributions of the other rheological characteristics are critical, as also demonstrated in a scenario where the more important model features have a less dominant or negative influence on the output based on their values (**Figure 27**B). In such cases, certain contributions of the features might be canceled out with the others, eventually leading to a decision based on mixed contributions of the rheological characteristics to the model.

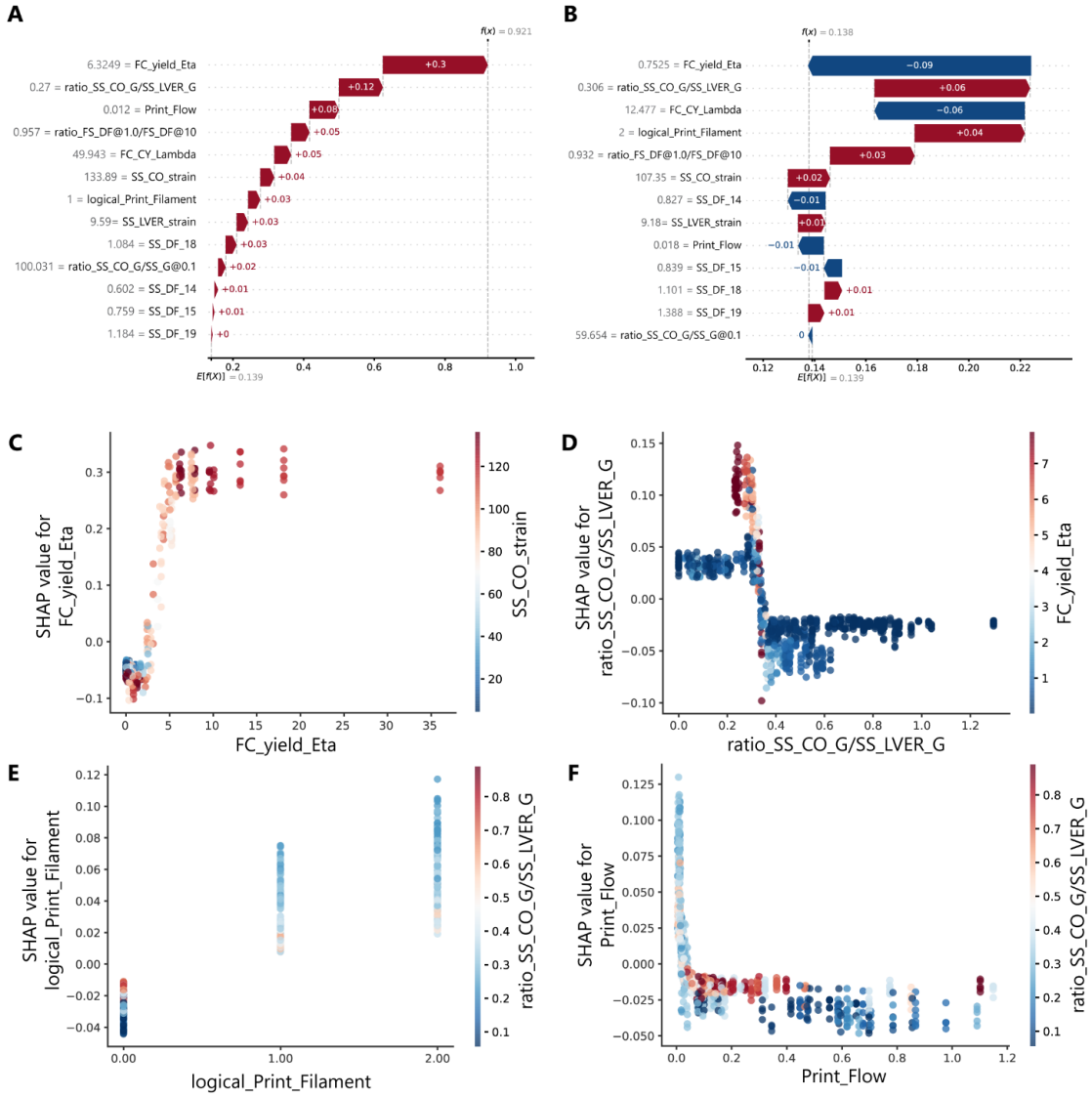

Figure 27. The explanations for individual predictions and SHAP dependence plots of some notable combinations of features. The Waterfall plots showing the collaborative influence (positive: red, negative: blue) of rheological characteristics in a randomly chosen prediction resulted in **A**) a significantly positive offset of the model's output (dashed vertical lines) from the baseline value of the model ($E(f(x))$, and **B**) an accumulative contribution resulting in a negligible offset of the model's output from the baseline value. Grey numbers indicate the actual value of the features per observation. The dependency plots show the SHAP value for **C**) yield viscosity, **D**) plasticity of formulation before the flow, **E**) the likelihood of filament formation during the extrusion, and **F**) the proportionality index of the flow.

In addition to the individual contributions, a significant amount of mutual impacts from different factors could occur in a multi-variable system. **Figure 27**C-F shows four of the most notable dependencies observed between the features of the models. Every dot in plots of **Figure 27**C-F corresponds to one prediction, and a SHAP value above zero meant a positive contribution of the feature in that prediction towards being classified as a printable formulation. In contrast, a value below zero negatively influenced the prediction outcome. It should be noted that a positive SHAP value for each feature in these dependency plots does not mean that predicting a formulation as printable is

guaranteed. Instead, it shows that a particular feature's positive contribution could depend on another feature's value. In this way, the higher strain required to create the flow resulted in a higher SHAP value for the yield viscosity, or a higher SHAP value for the degree of plasticity was observed when the formulations with lower plasticity before the flow had a higher yield viscosity (**Figure 27**C, D). While the formulations with no filament formation during the extrusion had negative SHAP values regardless of the degree of plasticity of the formulation, the lower degree of plasticity resulted in positive SHAP values for the likelihood of filament formation during the extrusion in case one was formed (**Figure 27**E).

Moreover, a dependency between the flow's consistency index and the degree of plasticity was observed. A moderate degree of plasticity at low consistency indices resulted in a more prominent contribution of the flow index to printability, as reflected by the higher SHAP value for the flow's consistency index. (**Figure 27**F).

5.5 Discussion

Current literature on assessing, evaluating, and predicting the printability of soft inks and bioinks mainly relies on case studies or the correlation between 3D extrusion-based printing process parameters [218, 239, 240]. Several studies focused on optimizing the 3D bioprinting process in terms of printability and cell viability in extrusion and droplet-based techniques [219]. The printability of a formulation is a result of the complex interactions between the different physical properties of additives and the base inks, together with the requirements of the process. The formulations investigated in this study involved a range of characteristic behaviors and included three rheology additives with essentially different physics for inducing printability. From a general point of view, the mechanisms driving the reinforcement and variation of viscoelasticity in these formulations could vary.

Additionally, some factors, such as the chemistry and affinity of the additives and base polymer solutions, could significantly change the mechanisms and outcome of interactions. These fundamental aspects were not separately considered in this study. Nevertheless, the rheological features investigated in this study reflected the formulations' material-dependent properties.

Similar to some of the findings of this study, it has been shown previously that in a colloidal system, critical flow-related and viscoelastic indices such as yield stress, stiffness and plasticity of the system, flow strain, and the flow transition index exhibited some patterns and distinct behaviors, which could hint towards a printable formulation [241]. However, such criteria's universality and applicability to different material systems have not been further studied.

The ML model identifies printable formulations in a pool of many observations based on knowledge of correlations and interactions during training. Apart from metrics to describe the model's accuracy, the conditions that resulted in recognizing the printable formulations with high accuracy are the key subjects in explaining how a new formulation with a given set of attributes would be classified. Analogically, the rationale behind making a particular model prediction is comparable to tuning some principal and dependent physical properties of the base polymer solution by adding additives that would enhance or worsen printability from an experimental point of view.

The few available studies on the application of ML in the field of 3D (bio)printing focused on either investigating a group of inks with similar characteristics or a set of process parameters with minimum alterations in ink properties [224-227]. The rationale behind limiting the factors is very reasonable, considering the interpretability of the

outcome and the required resources. However, we showed that it is possible to generate a physically interpretable model by diversifying the training pool to include several types of formulations. The quantification of the decision rules revealed that only a few features showed a distinct threshold that might be used as metrics in the rough data screening. Beyond that, it is highly unlikely to accurately describe printability by disregarding the rest of the rheological features, as they showed a collaborative influence on the overall printability induced in the formulation.

For the first time in the literature, we showed a generalized correlation between different rheological factors describing the printability of a hydrogel ink formulation. Accordingly, the obtained model predicts that from a statistical point of view, a formulation becomes printable when it shows a high yield viscosity and a low degree of plasticity before the flow, while the transition from Newtonian to non-Newtonian behavior of the flow occurs at relatively low shear rates. The formulation tends to flow at higher pressures during printing, and extruding through a small nozzle forms a filament rather than a droplet. The formulation based on polymer solutions with higher elasticity tends to be more printable, and a higher degree of stability of microstructural interaction over a range of frequencies is favored. While generally, a more extended range of linear viscoelasticity is desired, the damping factor of the formulations at low and high strain values should follow a pattern, as a formulation with more elasticity at the lower range and high viscous nature at the higher range is more desired.

Chapter 6

Concluding discussion and further perspectives

Sacrificial templating using biofabrication augments the advantages of different fabrication technologies, sometimes with concepts borrowed from different fields, into an application-oriented approach with a tailored scope based on the design requirements. Although the offerings seem promising, many prerequisites regarding the process, design, and material-related requirements should be met. To address this critical challenge, a deep and mechanistic understanding of the applied biofabrication technology would enable more efficient control over the manufacturing's outcome.

This doctoral thesis aimed to provide a systematic and in-depth analysis of two biofabrication technologies, which are shown to be capable methods for sacrificial templating. With the final objective of creating microchannels for guided vascularization, the applicability of MEW for generating templating structures was demonstrated in the first part of this thesis. This was followed by two chapters, where the characterization and optimization of PSPP for extrusion bioprinting were presented from the materials engineering viewpoint.

As an emerging biofabrication technology, MEW has shown great potential in delivering highly reproducible micron-scale structures in a tunable manner. However, using this technology for sacrificial templating is still in its infancy. This thesis showed that by controlling the MEW process parameter and choosing a suitable sacrificial material, it is possible to fabricate highly organized and low-dimension microfibers that could support the formation of microchannels in different embedding matrices.

Two sacrificial materials for templating microchannels were used, fully responsive to the adjustments of MEW process parameters and forming microfibers ranging from a few to hundreds of micrometers in a controlled manner. It was shown for the first time in the literature that a carbohydrate glass could be processed by MEW, and automated control of MEW parameters made the on-demand adjustments of fiber diameter based on the design reproducibly possible. It was shown that the fiber diameter could range between 20 to 200 microns in a one-step process, which is a technological step toward using fugitive carbohydrate glasses for application areas such as microfluidics.

Direct follow-ups on this study would explore two aspects of this methodology. Firstly, this method could be used to fabricate continuous and dimensionally compartmentalized microchannels with pre-defined diameters, which can be further endothelialized to study the influence of flow velocity and mechanical stimulation on the function and organization of the endothelial layer. The available literature on microfluidic platforms for studying vascularization often rely on channels with non-circular flow paths, which eventually deviate from the physiological *in vivo* flow profile and induced wall shear conditions. The methodology based on MEW of carbohydrate glass fibers provides a nearly perfect

circular cross-section of microchannels, a feature that results in the mimicry of flow profiles *in vivo*. Secondly, using the MEW of carbohydrate glasses, it is possible to fabricate uniform microchannels with precise diameters, which can be used to study the influence of shear rate during the flow of cells in a medium with defined viscosity and flow rate. This platform could enable in situ monitoring of shear-induced cell damage during processes involving high shear rates, such as extrusion bioprinting and injection of cell-laden hydrogels and polymer solutions. By controlling simple parameters of length and diameter of the microchannels, and flow rate and viscosity of carrier fluid, a versatile analytical tool for evaluating cell response to exerted fluid shear stress and its dynamics over time can be realized.

It was shown in this thesis that by MEW of a thermoplastic polymer with thermoresponsive dissolution behavior, branching microchannels for endothelialization within bulk hydrogel matrices can be fabricated. Implications of this approach, print-and-fuse strategy, in the field of tissue engineering are significant, as the optimization capacity of MEW allows fabrication of controlled sacrificial fiber dimensions, eventually resulting in the formation of branching microchannels approximating Murray's law. This distinctive feature has not been reported in any other study in the literature based on sacrificial templating. By deploying microvasculatures with high dimensional *in vivo* mimicry within hydrogel matrices, the flow profiles of branching microchannels can resemble *in vivo* conditions, and further stimulation and organization of the endothelial layer could be engineered with high precision.

Based on the principles of the print-and-fuse approach, vascularized *in vitro* platforms to study tissue regeneration or disease modeling in matrices with dimensions beyond the diffusion limit *in vivo* can be investigated. Specifically, by harnessing the predictability and precision of this approach for fabricating vascularized microchannels, geometrically defined placement of cellular aggregates for drug screening and the cell-ECM interactions can be anticipated.

So far, only a few studies have employed hybrid approaches based on MEW and extrusion bioprinting, or simply casting a hydrogel matrix [242-244], and the primary goal of converging two technologies was to reinforce the hydrogel matrices mechanically. Despite the complexities, the hybridization of MEW and extrusion bioprinting could provide exciting opportunities for vascularization using sacrificial templating. Although a direct study of the hybrid approach was not conducted in this thesis, a thorough and systematic investigation of each of the individual processes was performed.

The second part of this thesis was dedicated to an in-depth study of the PSPP in extrusion bioprinting from the bioink engineering perspective. The success of extrusion-

based biofabrication depends mutually on an in-depth understanding of the process and material-related aspects. Within the scope of this thesis, a great effort was made to reveal a general understanding of the concept of printability when formulations based on rheology modifiers are used as bioinks.

Recent trends in the literature showed a great interest in the biofabrication community to use blend and ink formulations due to their accessibility. In Chapter 4, it was shown that the physical properties of a simple formulation system based on HA and FmocFF are greatly influenced by the compositional design of the formulation, which was mainly reflected as alteration of gelation and self-assembly kinetics, and with change in the mechanical properties of the final formulations. This simple model system showed a glimpse of the available design tools to tune and alter the physical properties of the formulations in the context of extrusion bioprinting.

A direct follow-up on the study presented in Chapter 4 includes exploring fundamental design tools in formulations based on LMWG peptides in different hydrogel systems. It is anticipated that using FmocFF as a single gelator component, polymer solutions and hydrogels that were not previously printable can be processed as bioinks in extrusion bioprinting. This includes but is not limited to natural bioactive hydrogels such as collagen and gelatin, which often need additional post-processing steps to meet the shape fidelity criteria for extrusion-based biofabrication.

Taking a step further, it was shown in Chapter 5 that a generalized understanding of printability with respect to the ink's intrinsic physical properties could be conceived. The findings of this chapter are unique since it was for the first time in the literature that a large-scale analysis of the concept of printability with a minimum bias regarding the choice of the base material was conducted. For this purpose, an advanced descriptive machine learning approach was implemented, and the results showed that although unique criteria to benchmark printability in a diverse bioink library are highly unlikely, a generalized guideline for assessing and optimizing bioinks for extrusion bioprinting based on their rheological properties could be drawn.

Multiple follow-up studies based on the findings of Chapter 5 can be suggested. In the first step, the feasibility of building a generalized "predictive" model to predict the printability of formulations based on rheology additives should be addressed. For this purpose, the findings of Chapter 5 can be implemented as a kernel component in a machine learning algorithm, as the existing physical relationships lead to printability. Taking a step further, using the generalized descriptions of printable formulations presented in Chapter 5, one can build closed-loop monitoring and optimization algorithms to be a part of an automated biofabrication strategy. A few studies available

in the literature showed the potential of machine learning-powered automation approaches, which benefit from in situ monitoring and optimization tools to enhance the outcome of the biofabrication method [225, 226, 228, 230]. However, these studies were mainly concerned with the process parameters, limiting their outcome to a particular material system. Such automated biofabrication procedures are particularly interesting in a hybrid biofabrication approach, where geometrical considerations in the placement of bioinks are critical.

The vision of developing automated hybrid biofabrication technologies has never been closer to being realized in the literature. In a possible futuristic setting of a multi-technological biofabrication approach, the conclusions made by this thesis could be used to optimize and predict the outcome of a hybrid platform, which is based on MEW for the fabrication of templating microvascular structures, and extrusion bioprinting to deposit biologically engineered matrices according to the design requirements. The tools and methods presented in this thesis can enable researchers to precisely engineer the outcome of such complex processes. In the first step, the size and architecture of the sacrificial structure for templating microvasculature can be tuned by changing MEW process parameters, and multiple levels of hierarchy can be realized. In the next step, tuning the rheological and physical properties of the bioinks would ensure the successful deposition of inks at desired locations with high shape fidelity.

References

1. Jensen, C. and Y. Teng, Frontiers in molecular biosciences, 2020. **7**: p. 33.
2. Jain, R.K., et al., Nature biotechnology, 2005. **23**(7): p. 821-823.
3. Heinke, J., C. Patterson, and M. Moser, Frontiers in Bioscience (Elite Edition), 2012. **4**: p. 2269.
4. Meng, X., et al., Frontiers in Cell and Developmental Biology, 2021. **9**: p. 937.
5. Yang, G., et al., Progress in Biomedical Engineering, 2020. **2**(1): p. 012002.
6. Stratman, A.N., et al., Blood, The Journal of the American Society of Hematology, 2009. **114**(2): p. 237-247.
7. Mongiat, M., et al., International journal of molecular sciences, 2016. **17**(11): p. 1822.
8. Rioja, A.Y., et al., Acta biomaterialia, 2016. **29**: p. 33-41.
9. Fercana, G.R., et al., Biomaterials, 2017. **123**: p. 142-154.
10. Jiang, B., et al., Biomacromolecules, 2016. **17**(12): p. 3940-3948.
11. Ngo, M.T. and B.A. Harley, Biomaterials, 2020. **255**: p. 120207.
12. Abdul Sisak, M.A., F. Louis, and M. Matsusaki, Polymer Journal, 2020. **52**(8): p. 871-881.
13. Risau, W., Nature, 1997. **386**(6626): p. 671-674.
14. Jiang, M., et al., The international journal of biochemistry & cell biology, 2008. **40**(10): p. 2284-2295.
15. Ma, B., et al., Journal of Biomedical Materials Research Part A, 2020. **108**(1): p. 7-18.
16. Shang, T., et al., Stem cell research & therapy, 2019. **10**(1): p. 1-12.
17. Mastrullo, V., et al., Frontiers in Bioengineering and Biotechnology, 2020: p. 188.
18. Ross, A.M., et al., Small, 2012. **8**(3): p. 336-355.
19. Lai, E.S., et al., Regenerative medicine, 2012. **7**(5): p. 649-661.
20. Huang, N.F., et al., Biomaterials, 2013. **34**(16): p. 4038-4047.
21. Derricks, K.E., V. Trinkaus-Randall, and M.A. Nugent, Integrative Biology, 2015. **7**(9): p. 1011-1025.
22. Wragg, J.W., et al., Microcirculation, 2014. **21**(4): p. 290-300.
23. Bai, K., et al., Journal of biomechanics, 2010. **43**(6): p. 1176-1181.
24. Song, J.W. and L.L. Munn, Proceedings of the National Academy of Sciences, 2011. **108**(37): p. 15342-15347.
25. Zhao, M., et al., Journal of cell science, 2004. **117**(3): p. 397-405.
26. Crosby, C.O., et al., Tissue Engineering Part A, 2019. **25**(9-10): p. 746-758.
27. Cross, V.L., et al., Biomaterials, 2010. **31**(33): p. 8596-8607.
28. Gilchrist, A.E., et al., Advanced healthcare materials, 2019. **8**(20): p. 1900751.
29. Nichol, J.W., et al., Biomaterials, 2010. **31**(21): p. 5536-5544.
30. Yue, K., et al., Biomaterials, 2015. **73**: p. 254-271.
31. Chen, Y.C., et al., Advanced functional materials, 2012. **22**(10): p. 2027-2039.
32. Chen, X., et al., Tissue Engineering Part A, 2009. **15**(6): p. 1363-1371.
33. Li, S., et al., Nature materials, 2017. **16**(9): p. 953-961.
34. Burdick, J.A. and G.D. Prestwich, Advanced materials, 2011. **23**(12): p. H41-H56.
35. Hanjaya-Putra, D., et al., Blood, The Journal of the American Society of Hematology, 2011. **118**(3): p. 804-815.
36. Ruvinov, E., J. Leor, and S. Cohen, Biomaterials, 2010. **31**(16): p. 4573-4582.
37. Wang, W., et al., Journal of Biomedical Materials Research Part A, 2015. **103**(5): p. 1703-1712.
38. Trappmann, B., et al., Nature communications, 2017. **8**(1): p. 1-8.
39. Sun, G., et al., Biomaterials, 2011. **32**(1): p. 95-106.
40. Ponce, M.L., *Tube formation: an in vitro matrigel angiogenesis assay*, in *Angiogenesis Protocols*. 2009, Springer. p. 183-188.
41. Chwalek, K., et al., Scientific reports, 2014. **4**(1): p. 1-8.
42. Taubenberger, A.V., et al., Acta biomaterialia, 2016. **36**: p. 73-85.
43. Van Hove, A.H., et al., Journal of Controlled Release, 2015. **217**: p. 191-201.

44. Foster, G.A., et al., Biomaterials, 2017. **113**: p. 170-175.
45. Rauch, M.F., et al., Journal of Biomaterials Science, Polymer Edition, 2008. **19**(11): p. 1469-1485.
46. Brown, A., et al., Biomaterials, 2020. **243**: p. 119921.
47. Singh, R.K., D. Seliktar, and A.J. Putnam, Biomaterials, 2013. **34**(37): p. 9331-9340.
48. Moon, J.J., et al., Biomaterials, 2010. **31**(14): p. 3840-3847.
49. Kaushik, G., et al., Advanced healthcare materials, 2019. **8**(2): p. 1801186.
50. Juliar, B.A., et al., Biomaterials, 2020. **230**: p. 119634.
51. Ekaputra, A.K., et al., Biomaterials, 2011. **32**(32): p. 8108-8117.
52. Gniesmer, S., et al., Journal of tissue engineering and regenerative medicine, 2019. **13**(7): p. 1190-1202.
53. Zhang, K., et al., Acta biomaterialia, 2017. **51**: p. 246-257.
54. Da, L., et al., Acta Biomaterialia, 2017. **59**: p. 45-57.
55. Meyle, J., H. Wolburg, and A. Von Recum, Journal of biomaterials applications, 1993. **7**(4): p. 362-374.
56. Dobbenga, S., L.E. Fratila-Apachitei, and A.A. Zadpoor, Acta biomaterialia, 2016. **46**: p. 3-14.
57. Song, S., et al., Acta biomaterialia, 2015. **18**: p. 100-111.
58. Loh, Q.L. and C. Choong, 2013.
59. Bružauskaitė, I., et al., Cytotechnology, 2016. **68**(3): p. 355-369.
60. Chiu, Y.-C., et al., Biomaterials, 2011. **32**(26): p. 6045-6051.
61. Qazi, T.H., et al., ACS Biomaterials Science & Engineering, 2019. **5**(10): p. 5348-5358.
62. Mason, B.N., et al., Acta biomaterialia, 2013. **9**(1): p. 4635-4644.
63. Rao, R.R., et al., Angiogenesis, 2012. **15**(2): p. 253-264.
64. Ghajar, C.M., et al., Biophysical journal, 2008. **94**(5): p. 1930-1941.
65. Buchanan, C.F., et al., Cell adhesion & migration, 2014. **8**(5): p. 517-524.
66. Ogunrinade, O., G.T. Kameya, and G.A. Truskey, Annals of biomedical engineering, 2002. **30**(4): p. 430-446.
67. Ohura, N., et al., Journal of atherosclerosis and thrombosis, 2003. **10**(5): p. 304-313.
68. Tien, J., Comprehensive Physiology, 2019. **9**(3): p. 1155.
69. Gholobova, D., et al., Biomaterials, 2020. **235**: p. 119708.
70. Fleischer, S., D.N. Tavakol, and G. Vunjak-Novakovic, Advanced functional materials, 2020. **30**(37): p. 1910811.
71. Martino, M.M., et al., Proceedings of the National Academy of Sciences, 2013. **110**(12): p. 4563-4568.
72. Martino, M.M., et al., Frontiers in bioengineering and biotechnology, 2015. **3**: p. 45.
73. Saik, J.E., et al., Acta biomaterialia, 2011. **7**(1): p. 133-143.
74. Ehrbar, M., et al., Biomaterials, 2008. **29**(11): p. 1720-1729.
75. Liu, Q., et al., Journal of tissue engineering and regenerative medicine, 2017. **11**(5): p. 1562-1573.
76. Dvir, T., et al., Proceedings of the National Academy of Sciences, 2009. **106**(35): p. 14990-14995.
77. Freeman, I. and S. Cohen, Biomaterials, 2009. **30**(11): p. 2122-2131.
78. Kuzmic, N., et al., Biomechanics and modeling in mechanobiology, 2019. **18**(3): p. 717-731.
79. Kim, S., et al., Lab on a Chip, 2013. **13**(8): p. 1489-1500.
80. Belair, D.G., et al., Stem cell reviews and reports, 2015. **11**(3): p. 511-525.
81. Magnaudeix, A., et al., Acta biomaterialia, 2016. **38**: p. 179-189.
82. Kang, Y. and J. Chang, Regenerative medicine, 2018. **13**(06): p. 705-715.
83. Tang, F., et al., ACS Biomaterials Science & Engineering, 2020. **6**(3): p. 1476-1486.
84. Zieber, L., et al., Biofabrication, 2014. **6**(2): p. 024102.
85. Jain, R.K., et al., Nature medicine, 1997. **3**(11): p. 1203-1208.

86. Chung, S., et al., Annals of biomedical engineering, 2010. **38**(3): p. 1164-1177.
87. Groll, J., et al., Biofabrication, 2016. **8**(1): p. 013001.
88. Moroni, L., et al., Trends in biotechnology, 2018. **36**(4): p. 384-402.
89. Hochleitner, G., et al., Biofabrication, 2015. **7**(3): p. 035002.
90. Obata, K., et al., Light: Science & Applications, 2013. **2**(12): p. e116-e116.
91. Mota, C. and L. Moroni, *High throughput screening with biofabrication platforms*, in *Essentials of 3D biofabrication and translation*. 2015, Elsevier. p. 187-213.
92. Zhang, Y.S. and A. Khademhosseini, Tissue-Engineered Vascular Grafts, 2020: p. 321-338.
93. Kolesky, D.B., et al., Proceedings of the national academy of sciences, 2016. **113**(12): p. 3179-3184.
94. Kolesky, D.B., et al., Advanced materials, 2014. **26**(19): p. 3124-3130.
95. Zhang, Y.S., et al., Lab on a Chip, 2016. **16**(21): p. 4097-4105.
96. Lee, V.K., et al. *Generation of 3-D glioblastoma-vascular niche using 3-D bioprinting*. in *2015 41st Annual Northeast Biomedical Engineering Conference (Nebec)*. 2015. IEEE.
97. Lee, V.K., et al., Biomaterials, 2014. **35**(28): p. 8092-8102.
98. Hinton, T.J., et al., Science advances, 2015. **1**(9): p. e1500758.
99. Highley, C.B., C.B. Rodell, and J.A. Burdick, Advanced Materials, 2015. **27**(34): p. 5075-5079.
100. Bhattacharjee, T., et al., Science advances, 2015. **1**(8): p. e1500655.
101. Zhang, Y., Y. Yu, and I.T. Ozbolat, Journal of nanotechnology in engineering and medicine, 2013. **4**(2).
102. Zhang, Y., et al., Biofabrication, 2013. **5**(2): p. 025004.
103. Zhang, Y., et al., Biomaterials science, 2015. **3**(1): p. 134-143.
104. Xue, D., et al., ACS applied materials & interfaces, 2018. **10**(23): p. 19428-19435.
105. Zhu, W., et al., Biomaterials, 2017. **124**: p. 106-115.
106. Kelly, B.E., et al., Science, 2019. **363**(6431): p. 1075-1079.
107. Bernal, P.N., et al., Advanced materials, 2019. **31**(42): p. 1904209.
108. Castilho, M., et al., Trends in biotechnology, 2020. **38**(12): p. 1316-1328.
109. Dalton, P.D., et al., Advanced Science, 2020. **7**(11): p. 1902953.
110. Therriault, D., et al., Advanced Materials, 2005. **17**(4): p. 395-399.
111. Wu, W., et al., Soft Matter, 2010. **6**(4): p. 739-742.
112. Bellan, L.M., et al., Soft Matter, 2009. **5**(7): p. 1354-1357.
113. Wu, W., A. DeConinck, and J.A. Lewis, Advanced materials, 2011. **23**(24): p. H178-H183.
114. Skylar-Scott, M.A., et al., Science advances, 2019. **5**(9): p. eaaw2459.
115. Miller, J.S., et al., Nature materials, 2012. **11**(9): p. 768-774.
116. Pollet, A.M., et al., Micromachines, 2019. **11**(1): p. 43.
117. Kinstlinger, I.S., et al., Nature biomedical engineering, 2020. **4**(9): p. 916-932.
118. Kotz, F., et al., Nature communications, 2019. **10**(1): p. 1-7.
119. Brown, T.D., P.D. Dalton, and D.W. Hutmacher, Advanced Materials, 2011. **23**(47): p. 5651-5657.
120. Wei, C. and J. Dong, Journal of Micromechanics and Microengineering, 2013. **23**(2): p. 025017.
121. Taylor, G.I., Proceedings of the Royal Society of London. A. Mathematical and Physical Sciences, 1969. **313**(1515): p. 453-475.
122. Zhmayev, E., D. Cho, and Y. Lak Joo, Physics of fluids, 2011. **23**(7): p. 073102.
123. Hochleitner, G., et al., BioNanoMaterials, 2016. **17**(3-4): p. 159-171.
124. Nadernezhad, A., et al., Advanced Materials Technologies, 2021. **6**(8): p. 2100221.
125. Hrynevich, A., et al., Small, 2018. **14**(22): p. 1800232.
126. Florczak, S., et al., Polymer International, 2019. **68**(4): p. 735-745.

127. Robinson, T.M., D.W. Hutmacher, and P.D. Dalton, Advanced Functional Materials, 2019. **29**(44): p. 1904664.
128. Liashenko, I., A. Hrynevich, and P.D. Dalton, Advanced Materials, 2020. **32**(28): p. 2001874.
129. Saidy, N.T., et al., Small, 2019. **15**(24): p. 1900873.
130. McColl, E., et al., Materials & Design, 2018. **155**: p. 46-58.
131. Afghah, F., et al., Applied Sciences, 2019. **9**(17): p. 3540.
132. Zeng, J., et al., Microfluidics and Nanofluidics, 2018. **22**(2): p. 1-10.
133. Haigh, J.N., et al., Macromolecular Rapid Communications, 2016. **37**(1): p. 93-99.
134. Zhang, Y.S., et al., Nature Reviews Methods Primers, 2021. **1**(1): p. 1-20.
135. Naghieh, S. and X. Chen, Journal of Pharmaceutical Analysis, 2021. **11**(5): p. 564-579.
136. Cooke, M.E. and D.H. Rosenzweig, APL bioengineering, 2021. **5**(1): p. 011502.
137. Levato, R., et al., Advanced Materials, 2020. **32**(12): p. 1906423.
138. Malda, J., et al., Advanced materials, 2013. **25**(36): p. 5011-5028.
139. Decante, G., et al., Biofabrication, 2021. **13**(3): p. 032001.
140. Deo, K.A., et al., Tissue Engineering Part A, 2020. **26**(5-6): p. 318-338.
141. Ribeiro, A., et al., Biofabrication, 2017. **10**(1): p. 014102.
142. Hölzl, K., et al., Biofabrication, 2016. **8**(3): p. 032002.
143. Tarassoli, S.P., et al., Frontiers in bioengineering and biotechnology, 2021: p. 383.
144. He, Y., et al., Electroanalysis, 2016. **28**(8): p. 1658-1678.
145. Bégin-Drolet, A., et al., Additive Manufacturing, 2017. **15**: p. 29-39.
146. Gelber, M., et al., Additive Manufacturing, 2018. **22**: p. 38-50.
147. Gauvin-Rossignol, G., et al., Heliyon, 2018. **4**(7): p. e00680.
148. He, Y., et al., Microfluidics and Nanofluidics, 2015. **19**(2): p. 447-456.
149. Pollet, A.M., et al., Micromachines, 2020. **11**(1): p. 43.
150. Therriault, D., S.R. White, and J.A. Lewis, Nature materials, 2003. **2**(4): p. 265-271.
151. Nielsen, A.V., et al., Annual Review of Analytical Chemistry, 2019. **13**.
152. Au, A.K., et al., Angewandte Chemie International Edition, 2016. **55**(12): p. 3862-3881.
153. Castiaux, A.D., et al., Analytical chemistry, 2019. **91**(10): p. 6910-6917.
154. Bückmann, T., et al., Advanced Materials, 2012. **24**(20): p. 2710-2714.
155. Dalton, P.D., Current Opinion in Biomedical Engineering, 2017. **2**: p. 49-57.
156. Hochleitner, G., et al., Polymer, 2014. **55**(20): p. 5017-5023.
157. Kade, J.C. and P.D. Dalton, Advanced Healthcare Materials, 2020: p. 2001232.
158. Haigh, J.N., et al., Macromolecular rapid communications, 2016. **37**(1): p. 93-99.
159. Jiang, B., et al., Journal of agricultural and food chemistry, 2008. **56**(13): p. 5138-5147.
160. Borde, B. and A. Cesàro, Journal of thermal analysis and calorimetry, 2001. **66**(1): p. 179-195.
161. Cammenga, H. and B. Zielasko, Thermochimica acta, 1996. **271**: p. 149-153.
162. Shafiee, H., et al., Biomedical microdevices, 2009. **11**(5): p. 997-1006.
163. Brown, T.D., P.D. Dalton, and D.W. Hutmacher, Progress in Polymer Science, 2016. **56**: p. 116-166.
164. Hartel, R.W., R. Ergun, and S. Vogel, Comprehensive Reviews in Food Science and Food Safety, 2011. **10**(1): p. 17-32.
165. Dayan, C.B., et al., Materials & Design, 2018. **148**: p. 87-95.
166. Di Carlo, D., et al., Proceedings of the National Academy of Sciences, 2007. **104**(48): p. 18892-18897.
167. Ryma, M., et al., Advanced Materials, 2022: p. 2200653.
168. Baker, B.M. and C.S. Chen, Journal of Cell Science, 2012. **125**(13): p. 3015-3024.
169. Duval, K., et al., Physiology (Bethesda), 2017. **32**(4): p. 266-277.
170. Mandrycky, C., K. Phong, and Y. Zheng, MRS Commun, 2017. **7**(3): p. 332-347.
171. Grimes, D.R., et al., Journal of the Royal Society Interface, 2014. **11**(92).
172. Chang, W.G. and L.E. Niklason, NPJ Regen Med, 2017. **2**.

173. Wu, Q., et al., Biomed Eng Online, 2020. **19**(1): p. 9.
174. Hinton, T.J., et al., Sci Adv, 2015. **1**(9): p. e1500758.
175. Mota, C., et al., J Tissue Eng Regen Med, 2015. **9**(3): p. 174-90.
176. Moroni, L., et al., Nature reviews. Materials, 2018. **3**(5): p. 21-37.
177. Ma, J.Y., Y.C. Wang, and J. Liu, Rsc Advances, 2018. **8**(39): p. 21712-21727.
178. Gelber, M.K., et al., Additive Manufacturing, 2018. **22**: p. 38-50.
179. Miller, J.S., et al., Nat Mater, 2012. **11**(9): p. 768-74.
180. Gryka, M.C., et al., Addit Manuf, 2019. **26**: p. 193-201.
181. Schindelin, J., et al., Nature Methods, 2012. **9**(7): p. 676-682.
182. Zakaria, H., A.M. Robertson, and C.W. Kerber, Annals of biomedical Engineering, 2008. **36**(9): p. 1515.
183. Poon, C., bioRxiv, 2020.
184. Pries, A.R., D. Neuhaus, and P. Gaehtgens, American Journal of Physiology-Heart and Circulatory Physiology, 1992. **263**(6): p. H1770-H1778.
185. Robinson, T.M., D.W. Hutmacher, and P.D. Dalton, Advanced Functional Materials, 2019. **29**(44).
186. Nadernezhad, A., et al., Advanced Materials Technologies, 2021: p. 2100221.
187. Moreadith, R.W., et al., European Polymer Journal, 2017. **88**: p. 524-552.
188. Bloksma, M.M., et al., Macromolecules, 2011. **44**(11): p. 4057-4064.
189. Murray, C.D., Proceedings of the national academy of sciences of the united states of america, 1926. **12**(3): p. 207.
190. Moreau, B. and B. Mauroy, Journal of Rheology, 2015. **59**(6): p. 1419-1430.
191. Djonov, V.G., H. Kurz, and P.H. Burri, Developmental dynamics: an official publication of the American Association of Anatomists, 2002. **224**(4): p. 391-402.
192. Kurz, H. and K. Sandau, Comments Theor Biol, 1997. **4**(4): p. 261-291.
193. Klarhofer, M., et al., Magnetic Resonance in Medicine, 2001. **45**(4): p. 716-719.
194. Driver, I.D., et al., Frontiers in Neuroscience, 2020. **14**.
195. Papaioannou, T.G. and C. Stefanadis, Hellenic J Cardiol, 2005. **46**(1): p. 9-15.
196. Nadernezhad, A., et al., Polymer Journal, 2020. **52**(8): p. 1007-1012.
197. Du, X., et al., Chemical reviews, 2015. **115**(24): p. 13165-13307.
198. Fichman, G. and E. Gazit, Acta biomaterialia, 2014. **10**(4): p. 1671-1682.
199. Radvar, E. and H.S. Azevedo, Macromolecular bioscience, 2019. **19**(1): p. 1800221.
200. Groll, J., et al., Biofabrication, 2018. **11**(1): p. 013001.
201. Böck, T., et al., Macromolecular Bioscience, 2018. **18**(7): p. 1700390.
202. Baumann, B., et al., Angewandte Chemie International Edition, 2017. **56**(16): p. 4623-4628.
203. Stichler, S., et al., Biofabrication, 2017. **9**(4): p. 044108.
204. Tang, C., et al., Langmuir, 2009. **25**(16): p. 9447-9453.
205. Smith, A.M., et al., Advanced materials, 2008. **20**(1): p. 37-41.
206. Raeburn, J., et al., Soft Matter, 2012. **8**(4): p. 1168-1174.
207. Diaferia, C., G. Morelli, and A. Accardo, Journal of Materials Chemistry B, 2019. **7**(34): p. 5142-5155.
208. Aviv, M., et al., ACS applied materials & interfaces, 2018. **10**(49): p. 41883-41891.
209. Capito, R.M., et al., Science, 2008. **319**(5871): p. 1812-1816.
210. Huang, R., et al., Soft Matter, 2011. **7**(13): p. 6222-6230.
211. Graessley, W.W., Polymer, 1980. **21**(3): p. 258-262.
212. Orbach, R., et al., Langmuir, 2012. **28**(4): p. 2015-2022.
213. Gong, X., et al., Materials Science and Engineering: C, 2016. **58**: p. 478-486.
214. Chakraborty, P., et al., Macromolecular Rapid Communications, 2019. **40**(18): p. 1900175.
215. Nadernezhad, A. and J. Groll, Advanced Science, 2022: p. 2202638.
216. Sun, W., et al., Biofabrication, 2020. **12**(2): p. 022002.

217. Moroni, L., et al., Nature Reviews Materials, 2018. **3**(5): p. 21-37.
218. Naghieh, S. and D. Chen, Journal of Pharmaceutical Analysis, 2021.
219. Malekpour, A. and X. Chen, Journal of Functional Biomaterials, 2022. **13**(2): p. 40.
220. Goh, G.D., S.L. Sing, and W.Y. Yeong, Artificial Intelligence Review, 2021. **54**(1): p. 63-94.
221. Kim, J., et al., Frontiers in bioengineering and biotechnology, 2020. **7**: p. 443.
222. Yu, C. and J. Jiang, International Journal of Bioprinting, 2020. **6**(1).
223. An, J., C.K. Chua, and V. Mironov, International Journal of Bioprinting, 2021. **7**(1).
224. Conev, A., et al., Tissue Engineering Part A, 2020. **26**(23-24): p. 1359-1368.
225. Bone, J.M., et al., ACS Biomaterials Science & Engineering, 2020. **6**(12): p. 7021-7031.
226. Ruberu, K., et al., Applied Materials Today, 2021. **22**: p. 100914.
227. Lee, J., et al., Biofabrication, 2020. **12**(3): p. 035018.
228. Shi, J., et al., Annals of biomedical engineering, 2018. **46**(9): p. 1267-1279.
229. Shi, J., et al., Engineering, 2019. **5**(3): p. 586-593.
230. Jin, Z., et al., ACS Biomaterials Science & Engineering, 2021.
231. Menon, A., et al., 3D Printing and Additive Manufacturing, 2019. **6**(4): p. 181-189.
232. Shrikumar, A., P. Greenside, and A. Kundaje. *Learning important features through propagating activation differences*. in *International Conference on Machine Learning*. 2017. PMLR.
233. Ribeiro, M.T., S. Singh, and C. Guestrin. *" Why should i trust you?" Explaining the predictions of any classifier*. in *Proceedings of the 22nd ACM SIGKDD international conference on knowledge discovery and data mining*. 2016.
234. Lundberg, S.M. and S.-I. Lee. *A unified approach to interpreting model predictions*. in *Proceedings of the 31st international conference on neural information processing systems*. 2017.
235. Pedregosa, F., et al., the Journal of machine Learning research, 2011. **12**: p. 2825-2830.
236. Kursa, M.B. and W.R. Rudnicki, J Stat Softw, 2010. **36**(11): p. 1-13.
237. Lundberg, S.M., et al., Nature machine intelligence, 2020. **2**(1): p. 56-67.
238. Fisch, P., M. Holub, and M. Zenobi-Wong, Biofabrication, 2020. **13**(1): p. 015012.
239. Gillispie, G., et al., Biofabrication, 2020. **12**(2): p. 022003.
240. Fu, Z., et al., Biofabrication, 2021. **13**(3): p. 033001.
241. Corker, A., et al., Soft Matter, 2019. **15**(6): p. 1444-1456.
242. Visser, J., et al., Nature communications, 2015. **6**(1): p. 1-10.
243. de Ruijter, M., et al., Advanced healthcare materials, 2019. **8**(7): p. 1800418.
244. Afghah, F., et al., Advanced Healthcare Materials, 2022: p. 2102068.

Affidavit

I hereby confirm that my thesis entitled *Engineering approaches in biofabrication of vascularized structures* is the result of my own work. I did not receive any help or support from commercial consultants. All sources and/or materials applied are listed and specified in the thesis.

Furthermore, I confirm that this thesis has not yet been submitted as part of another examination process, neither in identical nor in similar form.

Dresden, 23.10.2022

Place, Date Signature

Eidesstattliche Erklärung

Hiermit erkläre ich an Eides statt, die Dissertation *Ingenieurtechnische Ansätze in der Biofabrikation vaskularisierter Strukturen* eigenständig, d.h. insbesondere selbständig und ohne Hilfe eines kommerziellen Promotionsberaters, angefertigt und keine anderen als die von mir angegebenen Quellen und Hilfsmittel verwendet zu haben.

Ich erkläre außerdem, dass die Dissertation weder in gleicher noch in ähnlicher Form bereits in einem anderen Prüfungsverfahren vorgelegen hat.

Dresden, 23.10.2022

Ort, Datum Unterschrift